\CORROSION AND CORROSION SUPPRESSION ON N-TYPE GALLIUM ARSENIDE SEMICONDUCTOR LIQUID-JUNCTION SOLAR CELLS/

by

James Edward \Cwynar/

Dissertation submitted to the Faculty of the
Virginia Polytechnic Institute and State University
in partial fulfillment of the requirements for the degree of
MASTER OF SCIENCE
in
Chemistry

APPROVED:

/ H. O. Finklea

P. E. Field

B. E. Hanson

August, 1984
Blacksburg, Virginia

ABSTRACT

CORROSION AND CORROSION SUPPRESSION ON N-TYPE GaAs SEMICONDUCTOR LIQUID-JUNCTION SOLAR CELLS

by

James Edward Cwynar

N-type GaAs is a potentially useful semiconductor in liquid junction type solar cells. Corrosion and corrosion suppression on an n-type GaAs semiconductor in both light and dark has been studied. The application of non-electroactive layers for corrosion suppression on semiconductor electrodes is a relatively new field. GaAs corrodes to form Ga(III) and As(III) solution species during photocurrent generation. The corrosion rate is determined electroanalytically in acidic media by measuring As(III) using differential pulse polarography (DPP). In neutral electrolytes a rotating ring-disc experiment measured the efficiency of hole-transfer to a redox couple. Two protecting processes have been utilized. Silanization and electrochemical polymerization of divinylbenzene and phenol were used to deposit non-electroactive layers on the electrode surface. The polyphenylene oxide coating partially suppressed corrosion in acid electrolytes. However, the coatings did not improve hole transfer efficiency in neutral electrolytes.

DEDICATION

This dissertation is dedicated to my parents,

, and My brothers,

ACKNOWLEDGEMENTS

I would like to express my appreciation of support to the following people:

To and for their moral support, without which this thesis would not have been completed.

To Dr. Harry O. Finklea for his encouragement and guidance during my time here and for his help.

To my friends,

for the help they gave me.

To for financial support during my stay.

To for typing my drafts.

And to my family for their love and patience, understanding and moral support during these past years.

TABLE OF CONTENTS

LIST OF TABLES

LIST OF FIGURES

I. Introduction

A. Introductory Remarks

With the advent of the Arab oil embargo in 1973 the interest in other energy forms, such as solar, nuclear, geothermal, and wind, has gained much attention. Of these, solar has gained much more attention, second to nuclear. Solar energy has been reportedly used by the public as early as 1934.(1) Presently, most people are familiar with passive solar energy. This includes solar housing design, earth walls, and collectors. Not as many people are knowledgeable about active solar energy, the conversion of light to electricity. This form is used to a smaller extent by remote communities in North Dakota where the cost of electricity from the nearest public utility plant would be enormous. Solar cells have found their way into satellite power generation, such as Lockheed's Milstar project bound for space in 1987, and NASA's Skylab. These projects use photovoltaic devices.

The term photovoltaics refers to solid-state semiconductor devices which convert sunlight directly into electricity. These systems are pollution-free with an unlimited energy source and can augment power grid supplies for industrial or domestic applications.

There are two main disadvantages: (1) storage of electricity and (2) cost of operation. Liquid-junction solar cells, on the other hand, utilize the light energy absorbed to form chemical redox reaction products. These products can be used to store energy. The liquid-junction cells have not been given much attention outside of the scientific community. These devices have one major drawback associated with them, namely, corrosion.

By inhibiting the corrosion of liquid-junction devices, longer lifetimes and possibly higher efficiencies may be obtained. Corrosion may be prevented or reduced by modifying the surface exposed to the liquid. This can result in greater stability, depending on the type of coating used.

My thesis is about corrosion and its suppression on n-type GaAs semiconductor liquid-junction solar cells. The use of modifying layers has also been studied and reported here.

B. Semiconductor physics

In order to better understand the workings of semiconductors in relation to their applicability in semiconductor liquid-junction solar cells, energy bands and atomic bonds must be described.

The concept upon which the molecular orbital theory is based declares that all orbitals of a molecule encompass the entire molecule and that delocalization of its electrons occurs over the molecule inclusively.(2) These molecular orbitals exist as bonding, anti-bonding, or nonbonding orbitals which may contain only two electrons per individual molecular orbital with their spins being of opposite sign.(2) As larger and larger molecules are formed with numerous electrons per atom, they may eventually condense into a crystal lattice. If such a structure contains atoms of a single element, then, on the average, the electron energy levels can be represented as closely spaced levels. (Figure 1)(3) In this diagram the left side represents the average energy of the atoms whereas the right half represents each individual energy level for each atom.

The question now arises as to why so many energy sublevels exist at each energy level. This is required by molecular orbital theory. If there exists a number

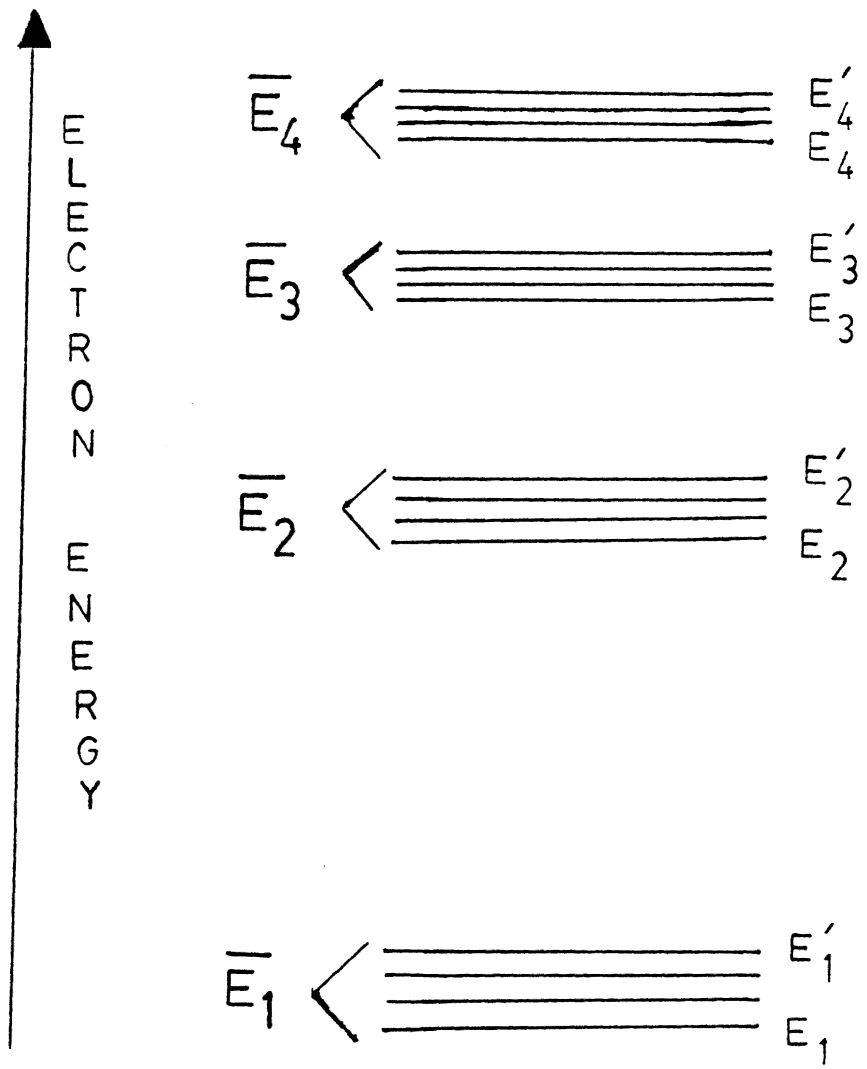

Energy level diagram of a crystal

Figure 1

of atoms, Q, with T atomic orbitals each, then there are Q•T molecular orbitals. These are frequently spaced so closely as to form energy bands, a continuous band of allowed energy levels. This picture is known as band theory. The spaces between these allowed energy bands are known as forbidden gaps. It is also of interest that these molecular orbitals can be localized or delocalized. In the crystal structure we are only concerned with the delocalized orbitals at present. An example of this is represented by Figure 2. (4)

At zero degrees Kelvin the highest fully occupied orbital is called the valence band. The energy of the top of the valence band is E_v. The next empty level above this is named the conduction band. Its lower energy limit is marked by E_c. The energy difference between these two energy levels is referred to as E_g, the difference between the bonding and anti-bonding levels. It is affected by structural properties of the crystal. This is not to be confused with the difference of energies between the top of the valence band and the bottom of the conduction band. This latter difference, ΔE_{cv}, determines the electrical properties (See Figure 3) and is referred to as the forbidden gap (or sometimes called the bandgap) energy.

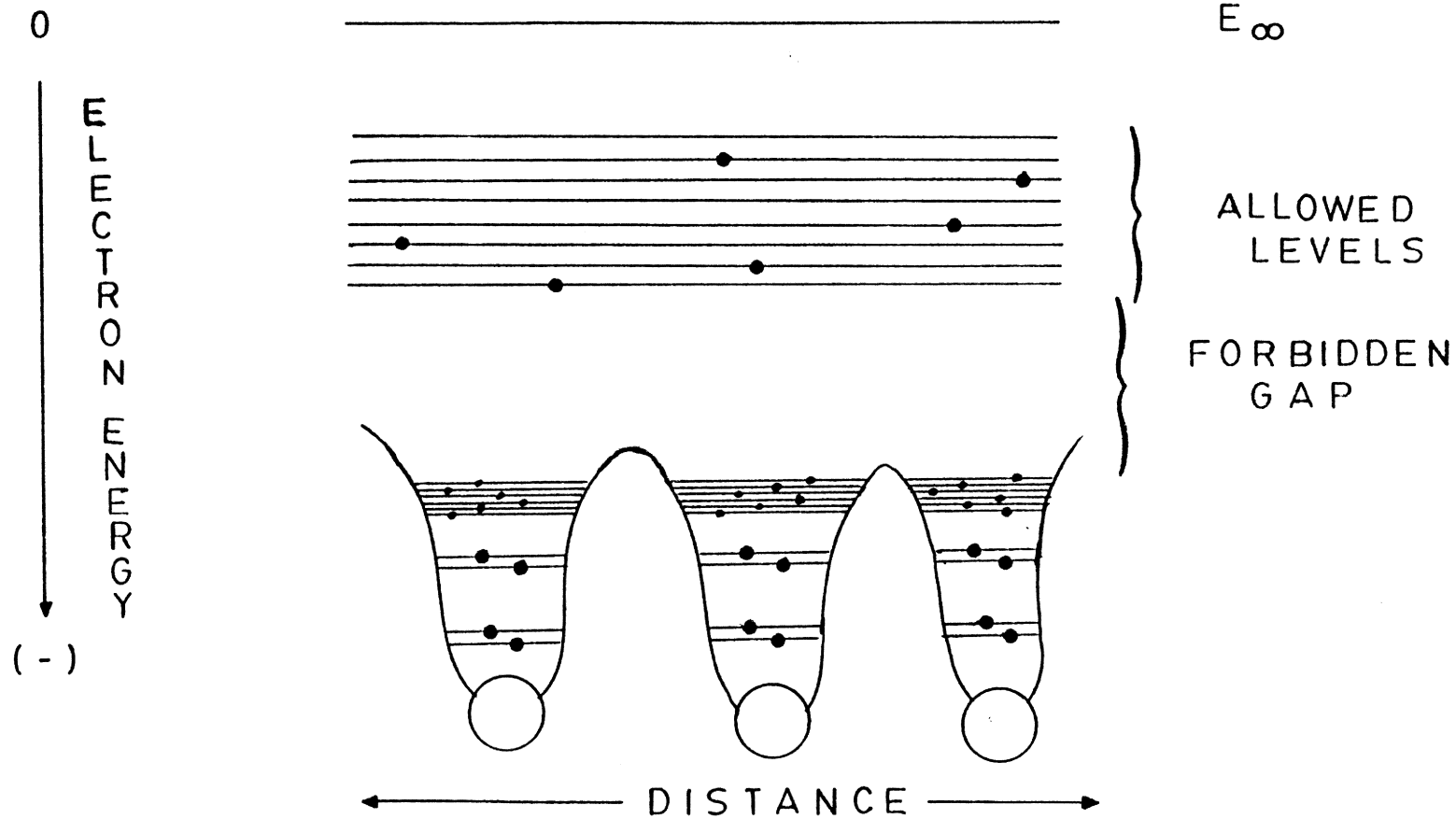

Energy diagram of delocalized orbitals in a crystal

Figure 2

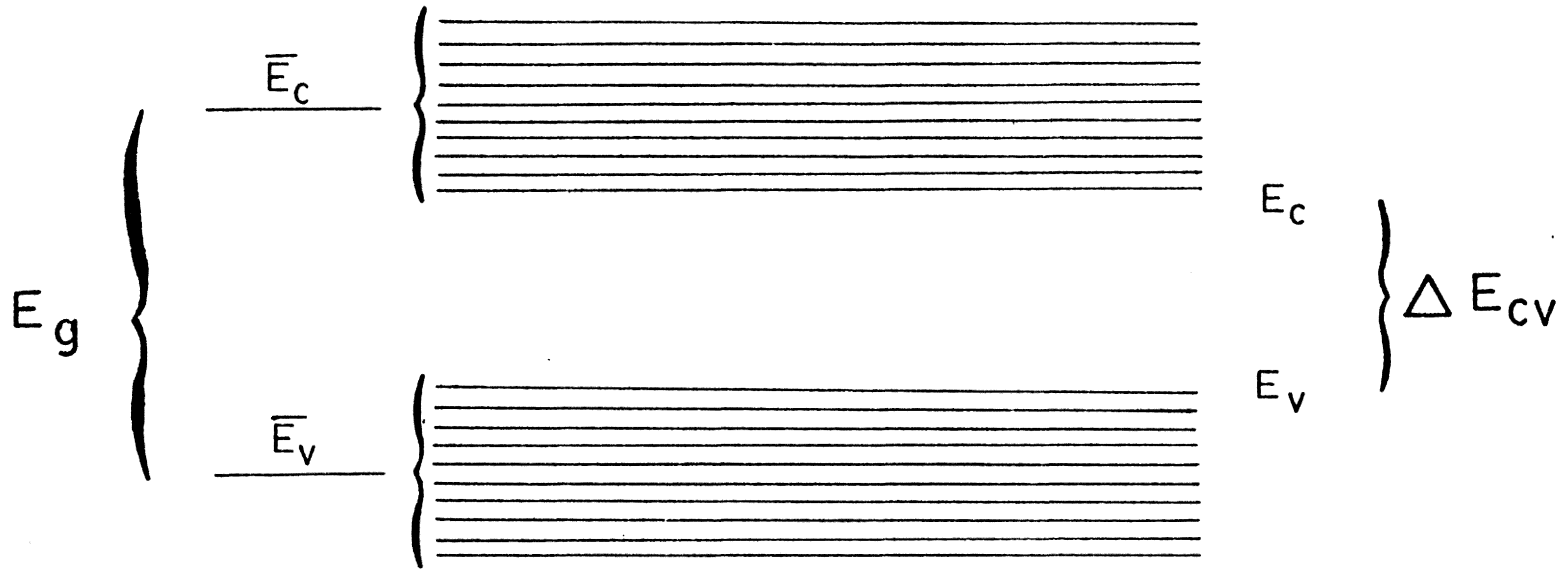

Energy Levels Illustration

Figure 3

(5) (6) It is this energy gap which gives the semiconductor its own distinctive characteristics.

The final energy topic relating to the subject at hand is the Fermi level, E_f, which represents the average energy of the free electrons in the crystal at any temperature.(4) It is "the energy at which the probability of an energy level being occupied by an electron is exactly one-half."(6) At absolute zero all the energy states below it are filled and all the states above it are empty. From this argument it can be stated that the energy of the electrons within the crystal corresponds to the Fermi level, which lies between the conduction band and the valence band. (See Figure 4) (7) (8)

The classification of metal, semiconductor, and insulator can now be discussed.

At absolute zero all electrons are in their lowest allowed energy levels. For a metal some of its electrons lie in a partially filled conduction band. This is quite the opposite for insulators and semiconductors. These two do not have any electrons within their conduction bands. When an electrical field is applied, current flow is observed in a metal, due to electron motion. In semiconductors and insulators such motion is not observed. All of their

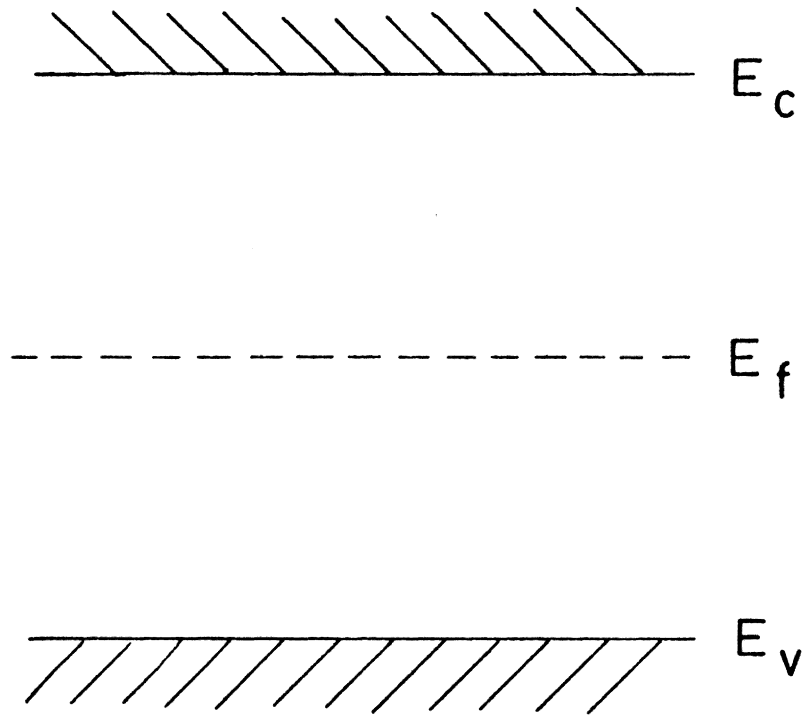

Fermi level diagram

Figure 4

electrons remain situated in the valence band and, thus, do not achieve enough energy to be promoted to the conduction band. Therefore, at absolute zero, both semiconductors and insulators are insulators.

When the temperature is raised above zero Kelvin, electrons in the valence band can move into the conduction band by thermal excitation, and electrical conduction will occur. Whether the electrical conductivity will be great enough depends on whether the bandgap energy is large (>3 eV), for insulators, or small (<3 eV), for semiconductors. These energy differences may be viewed in Figure 5. (3) (4) Table 1 exhibits relative bandgap energies of various semiconductors at room temperature. As it can be seen, some semiconductors have small bandgap energies, such as PbTe and InAs, while others have larger bandgap energies, such as CdS and TiO_2. (9)

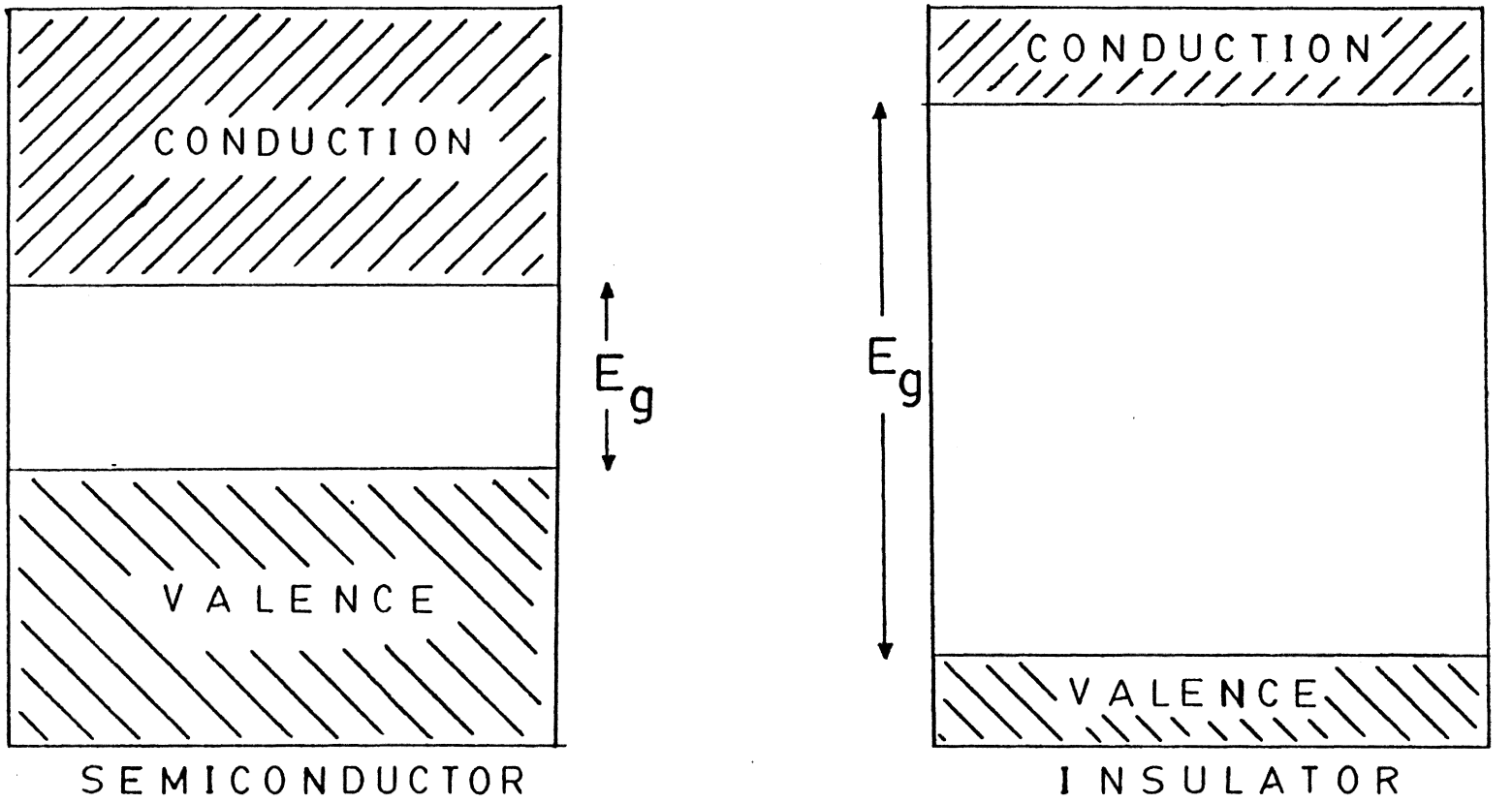

Band Energy Diagram for an Insulator and Semiconductor

Figure 5

Table 1

Bandgap Energies and Wavelengths of Various Semiconductors at Room Temperature

Semiconductor	Bandgap Energies (eV)	Onset Wavelength (nm)
PbTe	0.29	4280
InAs	0.33	3760
Ge	0.63	1970
Si	1.1	1130
InP	1.3	950
GaAs	1.4	890
Fe_2O_3	2.1	590
CdS	2.4	520
TiO_2	3.0	410
ZnO	3.2	390
SnO_2	3.5	350

The rest of this discussion will be concerned mainly with the semiconductor.

There exist two main categories of semiconductors, intrinsic and extrinsic. When an electron is promoted from the valence band into the conduction band, it leaves behind a positive vacant site or "hole". This hole is mobile like an electron and moves in the opposite direction in an electric field. This is true of both extrinsic and intrinsic semiconductors, with the main difference being that the intrinsic type is pure and the extrinsic type contains impurities called dopants. The dopant will be situated in the crystal lattice (See Figure 6) and will incorporate either filled or vacant energy levels in the bandgap region.

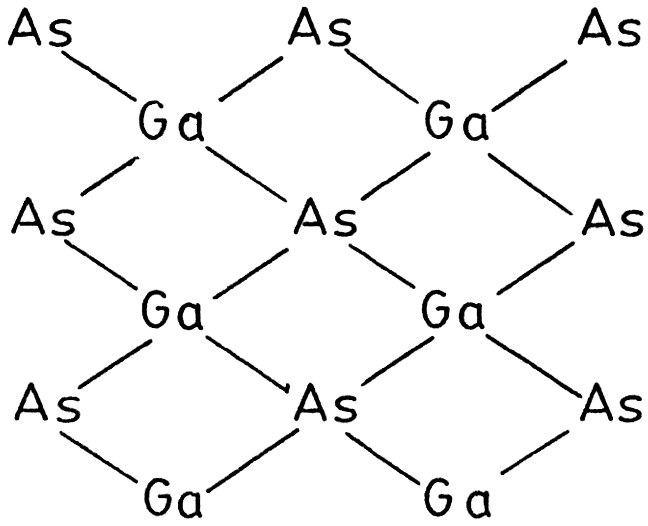

Intrinsic

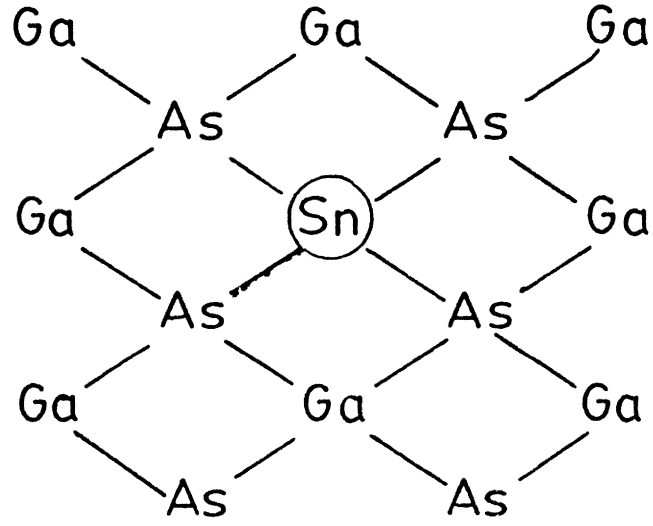

Extrinsic

Types of Semiconductors

Example: GaAs

Figure 6

This is observed when the electrons move into the conduction band by thermal excitation. Those which generate an excess of mobile electrons in the conduction band by thermal excitation are called n-type. On the other hand, semiconductors that have an excess of mobile holes are called p-type. An example of each is given as follows.

In a silicon lattice, in which each atom contains four valence electrons, a phosphorus atom, which contains five valence electrons, is substituted. The resultant lattice structure fixes the position of the phosphorus atom by silicon-phosphorus bonding. Thus, four of the electrons of phosphorus are located in the valence band. The fifth electron, being weakly bound to the phosphorus, can enter the conduction band, whereupon it moves freely throughout the lattice. Accordingly, the phosphorus is called a donor species (D) upon release of its extra electron, and the semiconductor is n-type.

Alternatively, if the silicon array is impregnated with gallium, which contributes only three valence electrons, an electron deficiency exists. Such kind of impurity accepts an electron from the valence band, and is called an acceptor (A). The electrons, in this case, are accepted from the valence band of the

silicon, creating holes. The resulting doping is p-type.

The type and amount of doping determines both the majority carrier, whether it be holes or electrons, and the concentration of the dopant carrier. Typical values for dopant concentration are between 10^{16} to 10^{20} carriers/cm^3. (10)

Doping influences the Fermi level according to the type of dopant (See Figure 7). N-type doping raises the Fermi level closer to the conduction band. This is primarily due to the donor levels located near the conduction band. (11) Conversely, those semiconductors which contain holes as the majority carriers, p-type, cause the Fermi level to shift closer to the valence band. Thus, these two shifts reflect the increase in electron population in the conduction band and the decrease in electron population in the valence band, respectively. If the dopant concentration is very great, the Fermi level can be driven into the valence band or conduction band. When this occurs, the semiconductor then becomes a quasi-metal. (6)

Consequently, these changes also influence the conductivity of the semiconductor. The normal conductivity range varies from 10^{2} to 10^{-4} mho per meter for semiconductors, 10^{-6} to 10^{-14} mho per meter

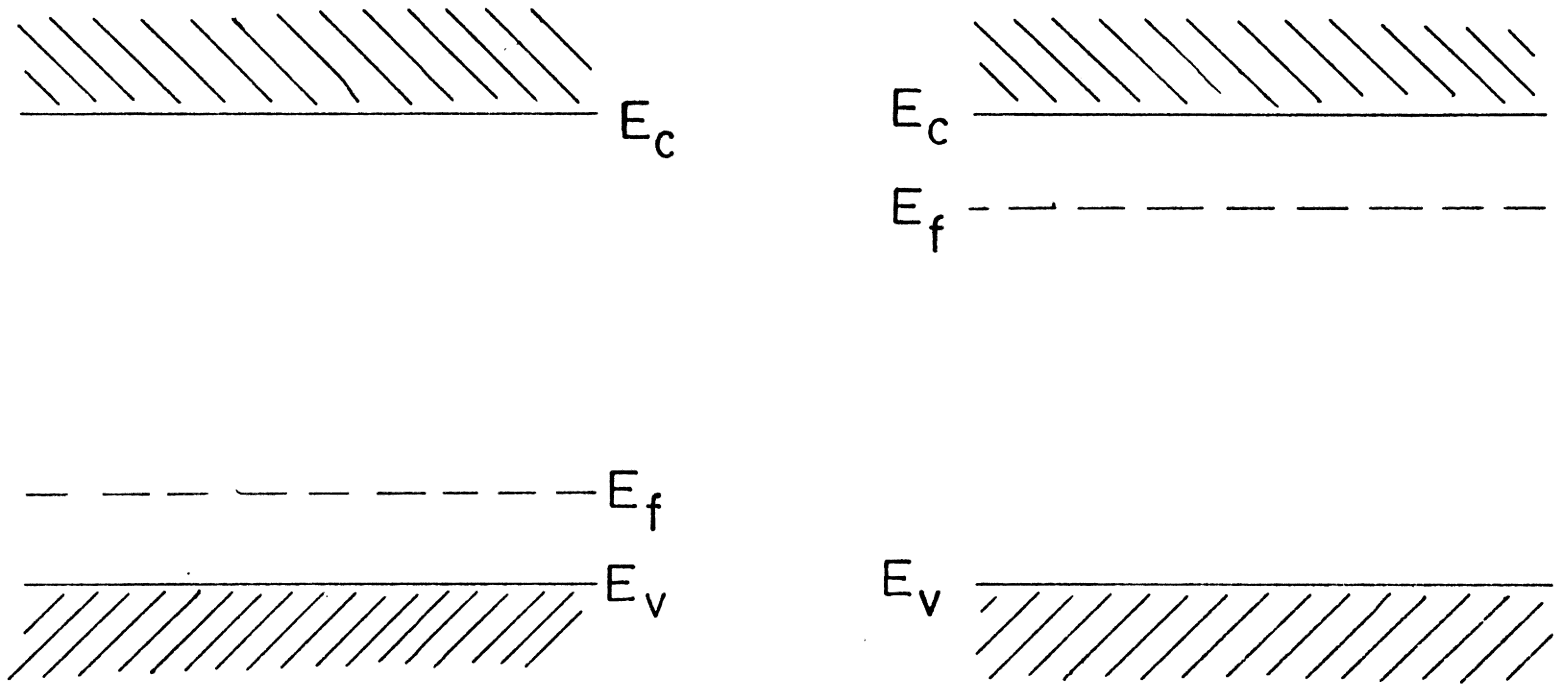

Fermi levels in
p- and n-doped semiconductors

Figure 7

for insulators, and 10^{3} to 10^{4} mho per meter for metals. Thus, the consequence of heavily doping a semiconductor is reflected in the conductivity. (9)

The next area of semiconductor physics takes us from isolated crystals into that of junction formation or, in other words, semiconductor/electrolyte interfaces.

When interfacing, in this case, a semiconductor and a solution, a couple of important facts concerning the Fermi level still apply. (i) The probability of finding an electron state being filled is one-half at the Fermi level (as previously stated); (ii) since the thermodynamic free energy of the system per electron is a concern, the Fermi level must remain continuous across the point of contact. (12)

Prior to contact with a solution (See Figure 8(a)), the n-type semiconductor's Fermi level lies close to the conduction band. As for the solution, its Fermi level is different, usually, and is the energy located between the oxidized species (higher energy) and the reduced species (lower energy). After contact has been accomplished (See Figure 8(b)), the Fermi level of the semiconductor remains flat from the bulk to the surface while the two Fermi levels move together by charge transfer across the interface. Meanwhile,

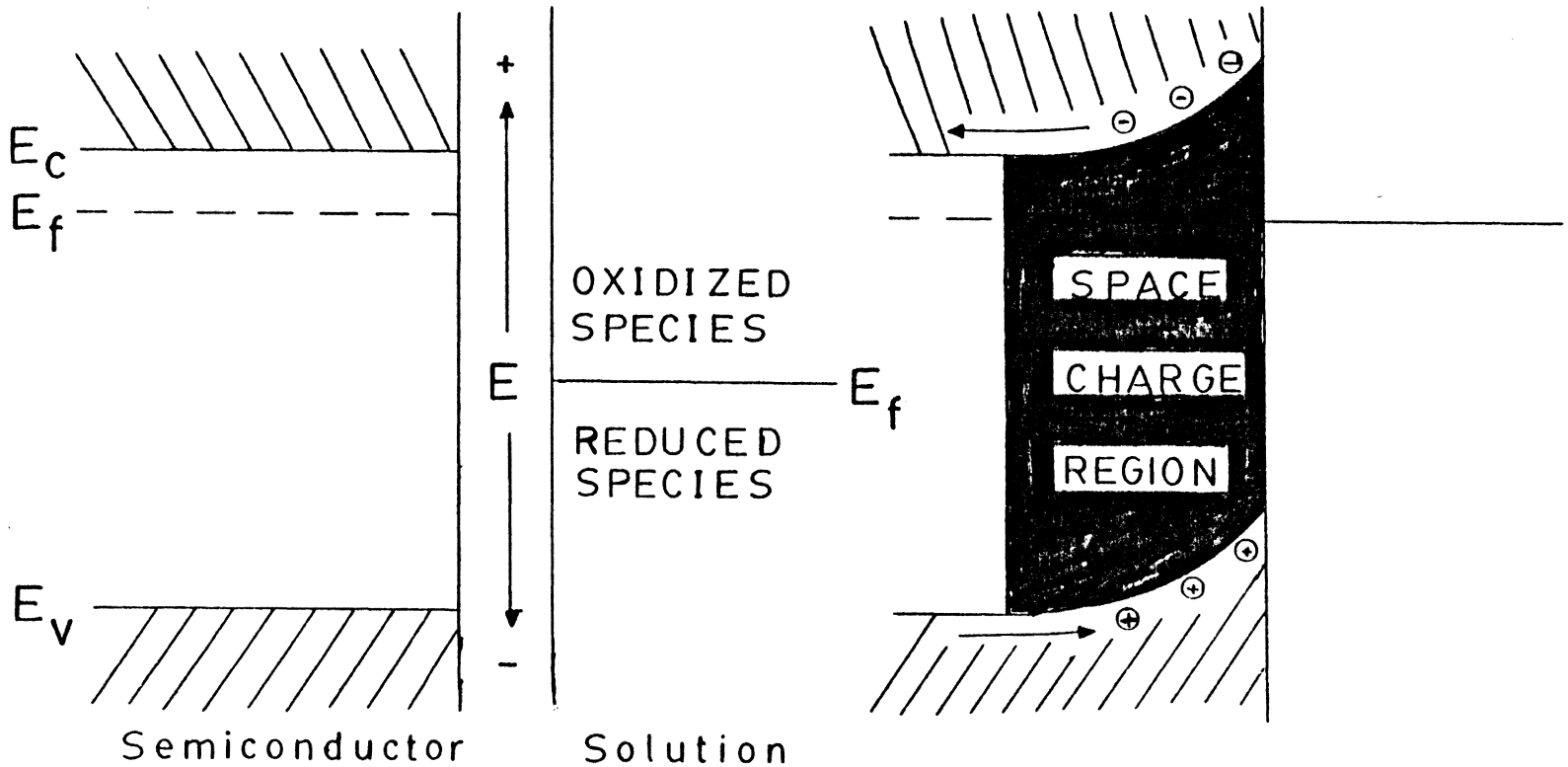

Figure 8
n-type semiconductor liquid-junction solar cell
(a) prior to contact
(b) after contact
semiconductor positive with respect to E_{fb}

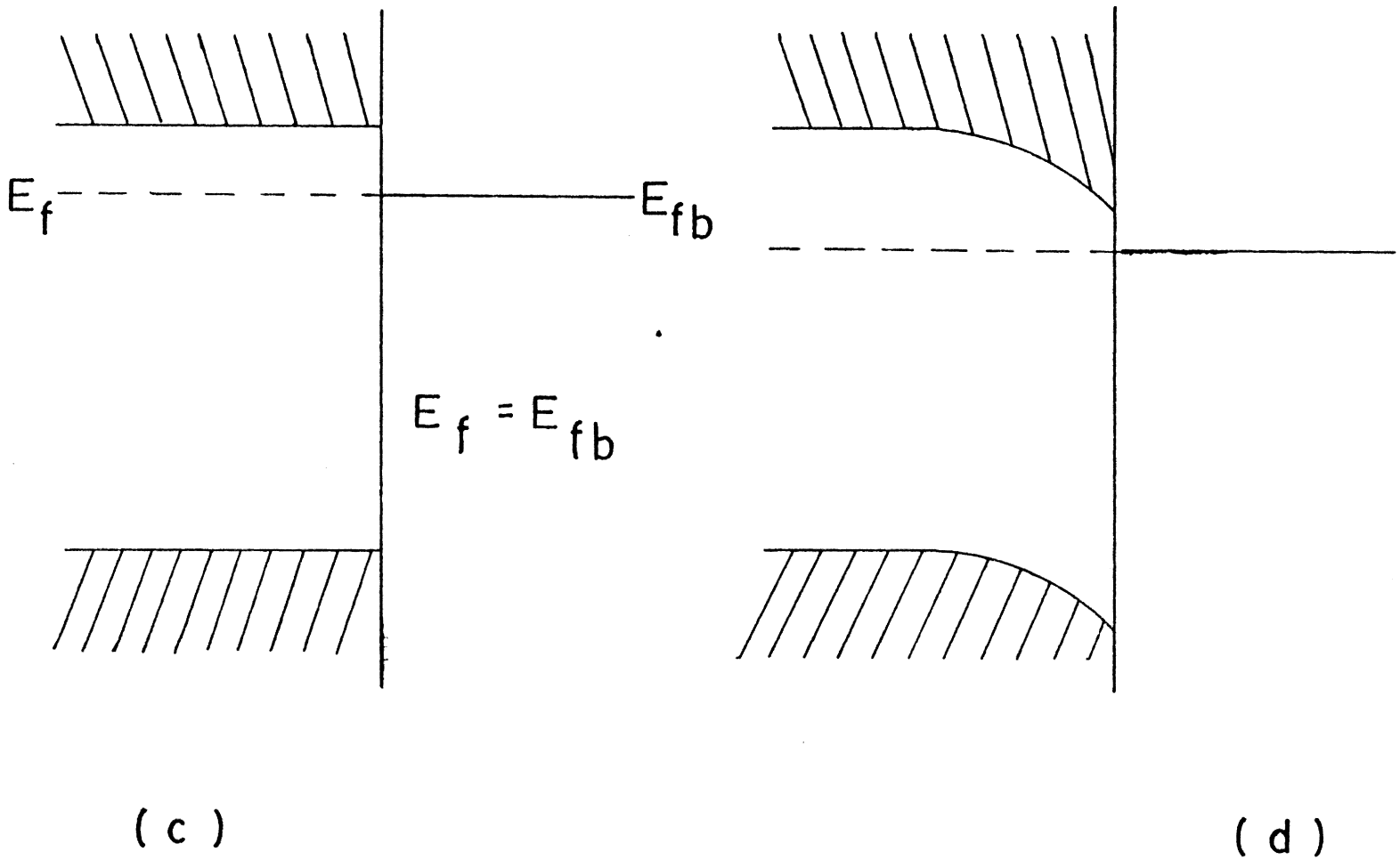

Figure 8 (continued)
(c) after contact with zero potential charge
(d) after contact
semiconductor negative with respect to E_{fb}

where the conduction and valence bands approach the surface, upward bandbending occurs. (The opposite is usually true for p-type semiconductors.) This effect is due to the semiconductor becoming more positive in potential with respect to the solution. Electrons flow away from the surface and holes move towards it. When this occurs, a space charge region develops in which the electrons and holes are inhomogeneously distributed (unlike a metal which has all charge placed on its surface). The third diagram (Figure 8(c)) defines the flatband potential, E_{fb}, when the solution and semiconductor come in contact. In this example, the observation of no bandbending is due to zero excess charge existing in the semiconductor.

In the last example (Figure 8(d)), the semiconductor has developed a potential which is negative with respect to E_{fb}. Contact has been made with a redox couple of high energy. In this case the energy bands are bent downward when they approach the surface of the semiconductor. (13)

If an external voltage is applied to the semiconductor/electrolyte system (with respect to a reference electrode), then the bandbending within the space charge region is controllable. The Fermi level of the electrode can be changed with respect to the

Fermi level of the solution. This effect may be demonstrated in three cases. (See Figure 9.)

In 9(a) a potential positive of V_{fb} (the flatband potential) is applied. A depletion layer of majority carriers is observed at the surface within the space charge region. This is due to a flow of majority carriers in the conduction band towards the bulk. The minority carriers in the valence band increase near the surface. A net positive charge has now formed within the space charge region. Meanwhile, the holes in the bulk of the semiconductor have been neutralized by electrons. Thus, as a result, the space charge region acts as an insulator. If the depletion layer becomes deep enough when a high enough external voltage is applied (+10 volts vs. V_{fb} for example), the valence band may be bent to the point where the Fermi level enters the valence band near the surface (Figure 9(b)). An inversion layer has formed, in which the surface of an n-type semiconductor has become p-type. It is essentially a severe case of depletion with the added result of the accumulation of minority carriers within the valence band near the surface. Finally, in Figure 9(c), an accumulation layer can be observed. This may be accomplished by applying a negative enough voltage with respect to V_{fb} or by having the electron donor

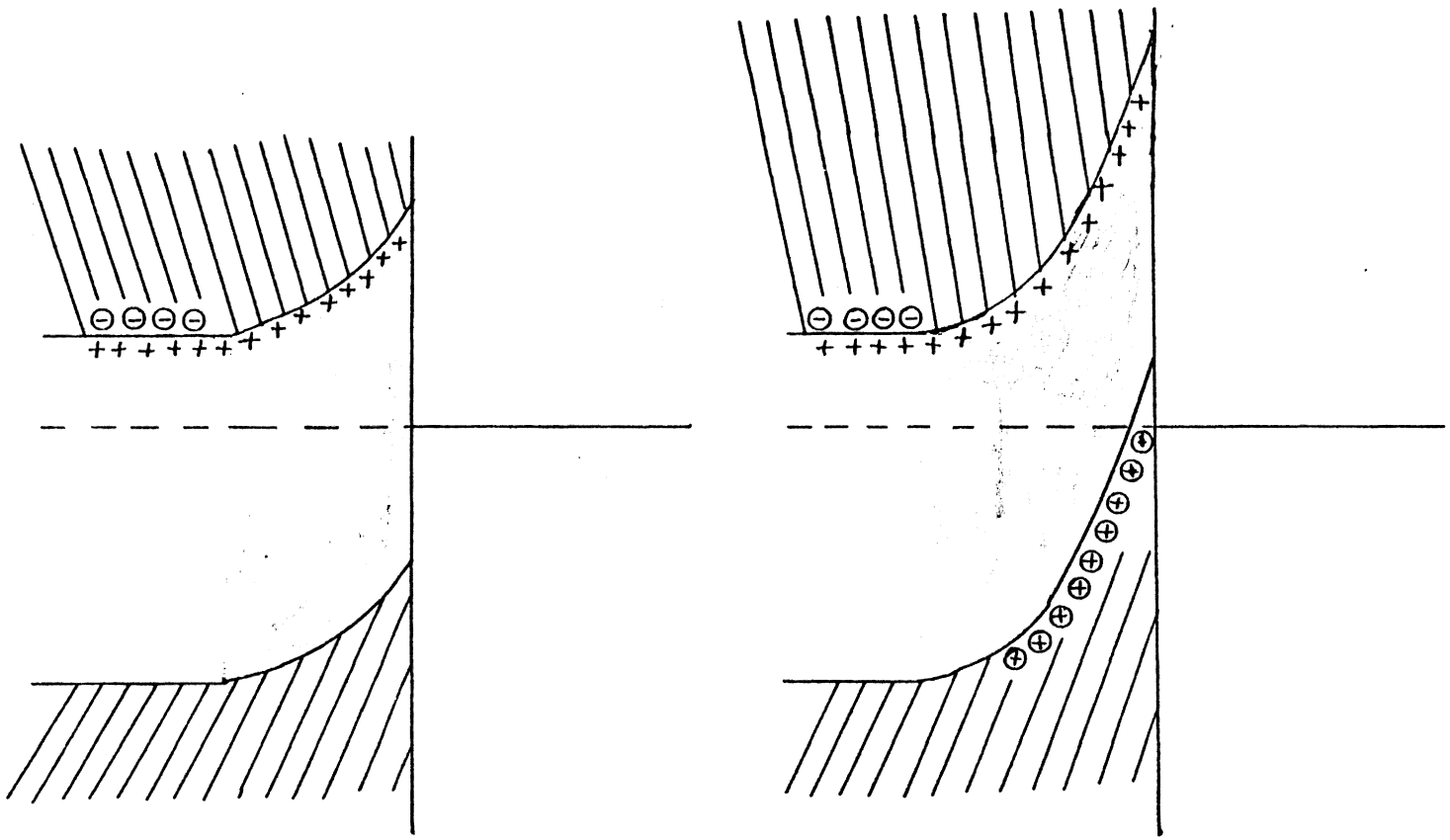

Figure 9
Space charge layers
(a) Depletion
(b) Inversion

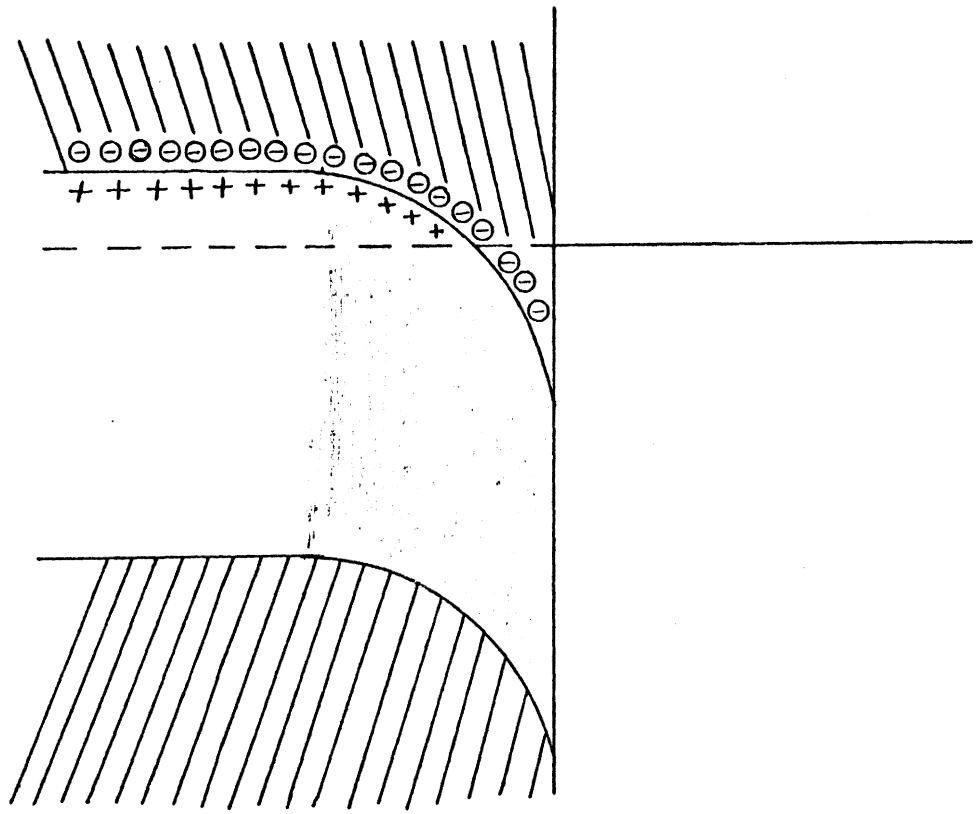

(c)

Figure 9 (continued)
(c) Accumulation

species in the solution at a high enough concentration so as to force electrons into the semiconductor. If the accumulation of electrons is so great that the Fermi level is driven into the conduction band, a degenerate surface results and the resultant surface behaves both like a metal and a semiconductor, i.e., a quasi-metal.

The discussion will now consider the electrolyte part of the interface. In laying this groundwork, the electrochemical triple layer (See Figure 10) is described.

A triple layer in solution consists of an inner Helmholtz plane, an outer Helmholtz plane, and the diffusion layer. At the interface the metal, in this example, only has a negative surface charge of 3 Å thickness while the solution provides a large collection of positively charged ions within the triple layer. (If a semiconductor is used, the space charge layer would be approximately 100 to 10,000 Å deep.) (12) (14) As one proceeds from the solid surface towards the bulk electrolyte, the first layer of molecules encountered consists of adsorbed ions and water. This region is called the "inner Helmholtz plane." Continuing outward, solvated cations and anions are encountered and this layer is entitled the "outer

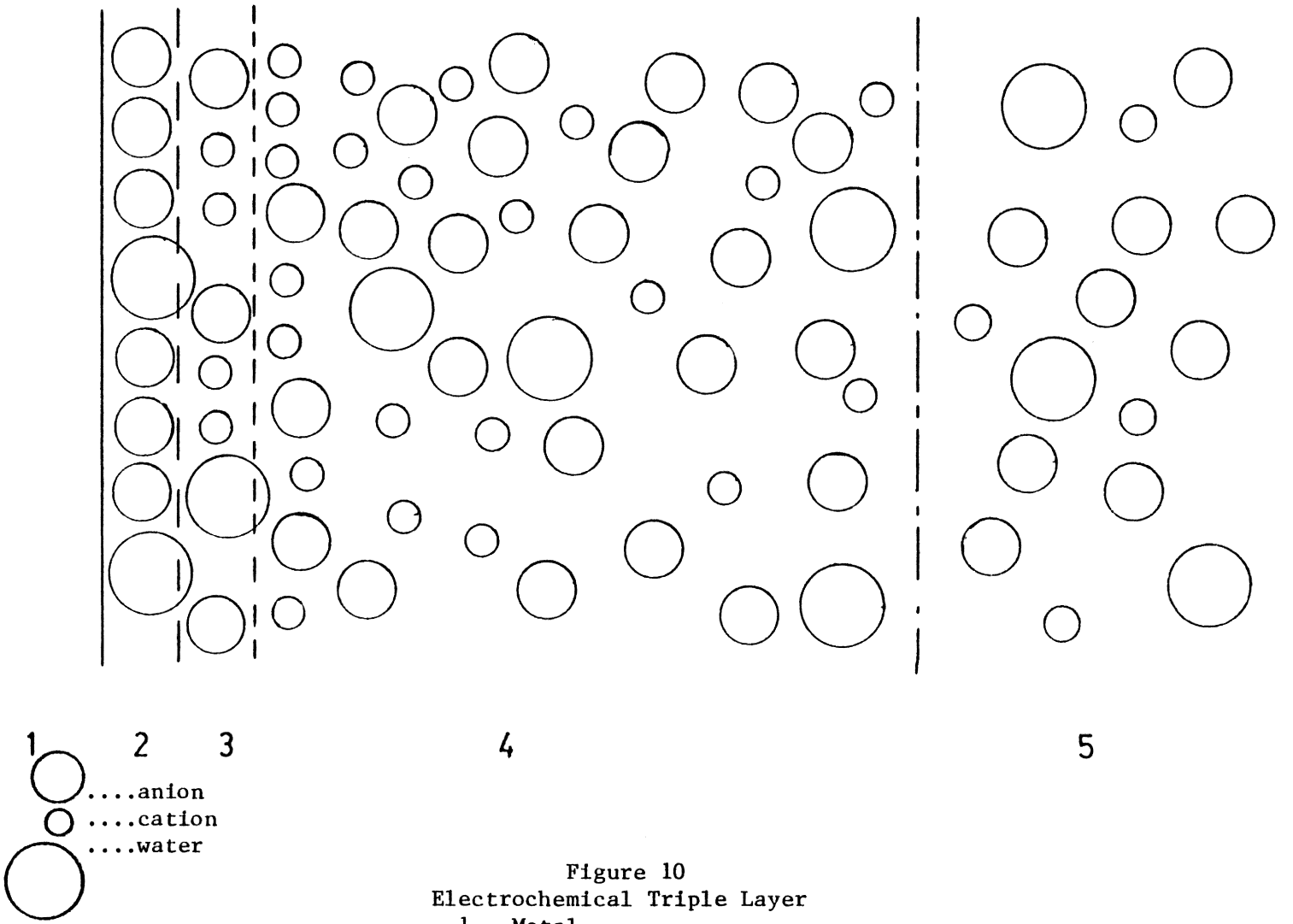

Figure 10
Electrochemical Triple Layer
1. Metal
2. Inner Helmholtz Plane
3. Outer Helmholtz Plane
4. Diffusion Layer
5. Bulk

Helmholtz plane." The thickness of each layer is in reality only the average diameter thickness of a water molecule. These two layers together act as a dielectric between the conducting electrolyte layer and the solid. (14) (15) (16) The diffuse layer has a concentration of excess charge with respect to the bulk, starting with higher excesses near the surface and progressing to lesser concentrations at further distances. Thus, the solid, the inner and outer Helmholtz planes, and the diffusion layer can be viewed as a capacitor which can be broken down into the capacitances in series, $C_{spacecharge}$, $C_{Helmholtz}$, and $C_{diffuse}$.

When a voltage within the normal operating range is applied to the n-type semiconductor electrode, one of the following conditions prevail. (See Figure 11) If the applied potential is more positive than the flatband potential of the semiconductor (Figure 11(a)), upward bandbending occurs within the space charge layer of the semiconductor and the Fermi level of the semiconductor is lowered with respect to the reference electrode Fermi level. A depletion of electrons in the conduction band of the space charge region develops as they flow to the bulk of semiconductor. At the same time holes in the valence band move toward the surface.

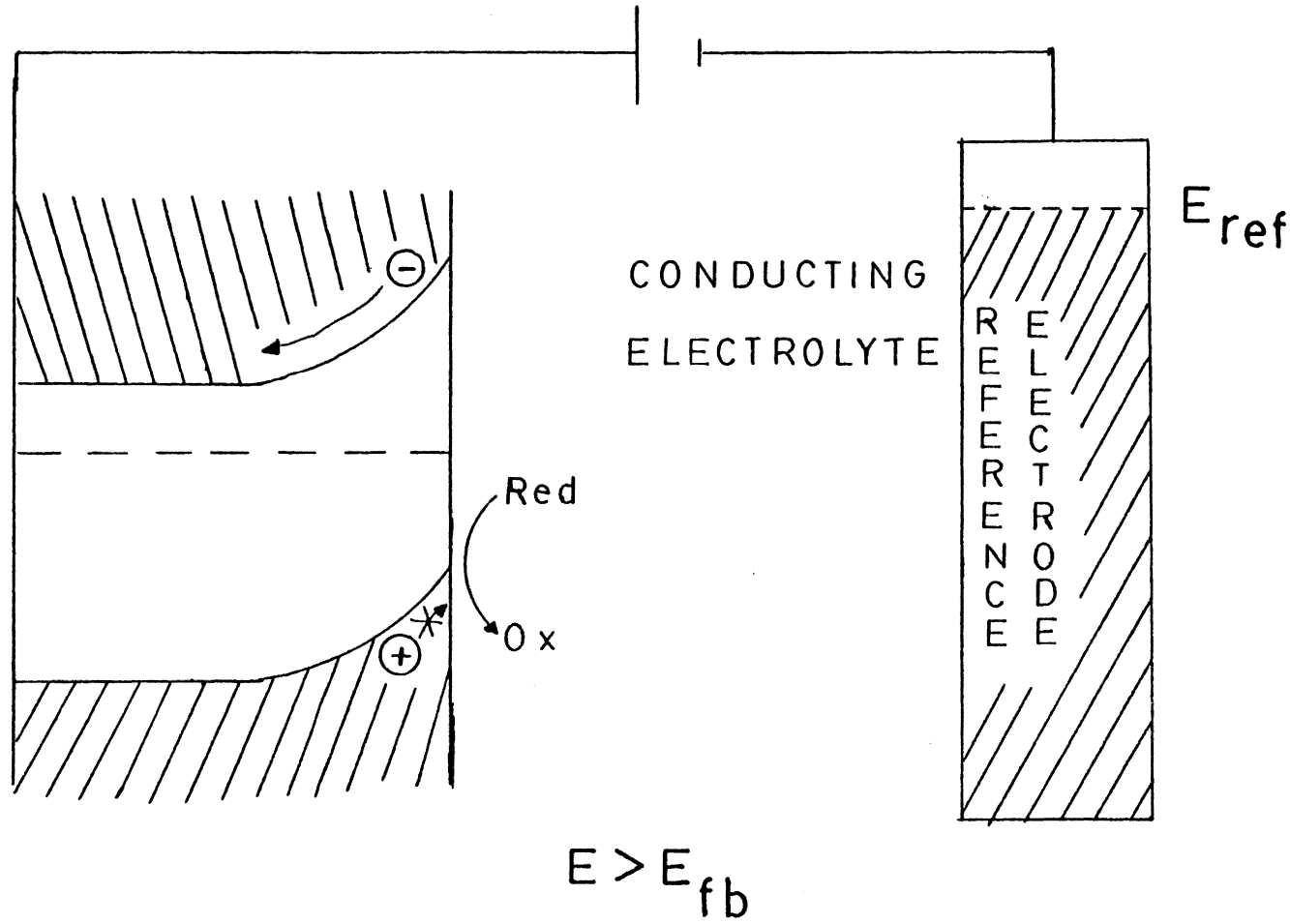

Figure 11
Voltage applied to n-type semiconductor

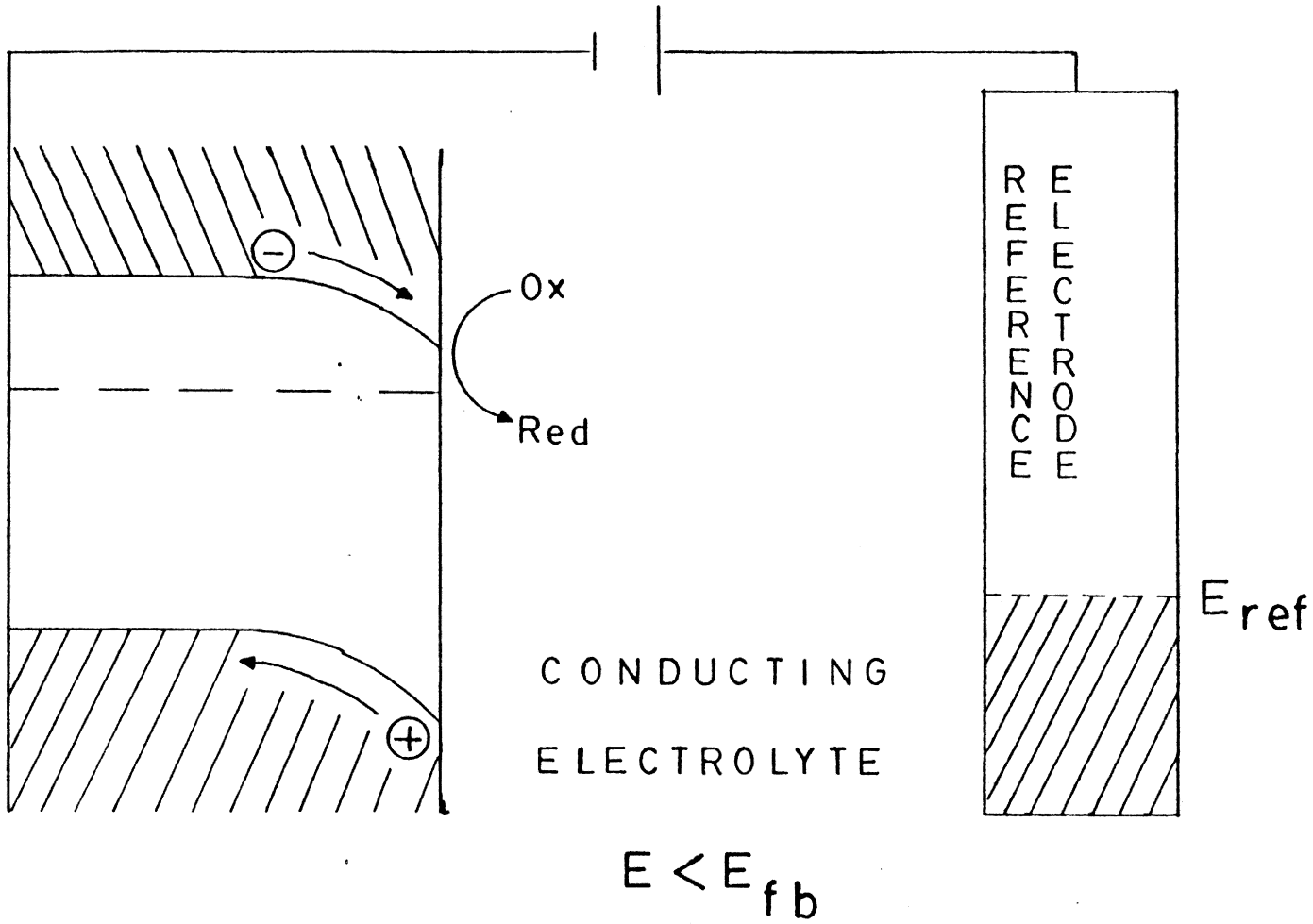

Figure 11 (continued)

However, their concentration is so low in an n-type semiconductor that the electrode is effectively blocking. If the applied potential is more negative than the flatband potential of the semiconductor (Figure 11(b)), downward bandbending occurs within the space charge layer of the semiconductor. The electrons accumulating within the space charge layer can combine with oxidized species in the solution to generate the reduced form. Holes tend to move from the space charge layer into the bulk. Finally, if the voltage applied is equal to the flatband potential, then no bandbending occurs. Consequently, a redox reaction might or might not happen, depending on its redox potential and the doping.

Light absorption will now be discussed.

As mentioned earlier, all semiconductors have a certain bandgap energy. These bandgap energies in turn can be related to their individual wavelengths at which light absorption begins (See Table 1) by the formula

$$\lambda_{BG} = \frac{1240}{E_{BG}}, \text{ where } \lambda_{BG}$$

is the onset bandgap wavelength in nanometers, and E_{BG} is the bandgap photon energy in electron-volts. 1240 is the conversion factor to change electron-volts to nanometers, as derived from $E = h\nu$ and $\lambda\nu = c$. (4) (6)

For light of wavelengths longer than the onset bandgap wavelength of the semiconductor, photons are not absorbed. But for those wavelengths that are equal to or shorter than the bandgap wavelengths, the photons are absorbed and produce excited electron-hole pairs. Photoexcitation of electrons is possible even at absolute zero.

Recombination of electron-hole pairs can occur, but within the space charge region, the two can become separated. For positive bandbending, the electron travels toward the bulk of the semiconductor and the hole moves toward the surface. At this point--the hole can react with reduced species to produce the oxidized species. In the meantime, the electron flows to the counter electrode, where it reacts with an oxidized species to generate the reduced form. (The counter electrode is a second electrode that serves to complete the current loop through the cell. The counter electrode is usually placed in a separate compartment that is connected to the working electrode compartment by a glass frit.) Thus, Figure 12 summarizes the basic steps involved in photogeneration of electron-hole pairs while Figure 13 displays the physical reality of these processes. (10) (17) This is the basis of solar energy conversion in a semiconductor liquid-junction

Process	Reaction
light absorption	$e^-_{vb} \longrightarrow h^+_{vb} + e^-_{cb}$
recombination	$h^+_{vb} + e^-_{cb} \longrightarrow$ heat
charge separation	$e^-_{cb} \longrightarrow e^-_{bulk}$
	$h^+_{vb} \longrightarrow h^+_{surface}$
interface reactions	$e^-_{bulk} + Ox \longrightarrow$ Red (at counter electrode)
	$h^+_{surface} + Red \longrightarrow Ox$

vb = valence band

cb = conduction band

Electron-hole pair photogeneration and reaction processes

Figure 12

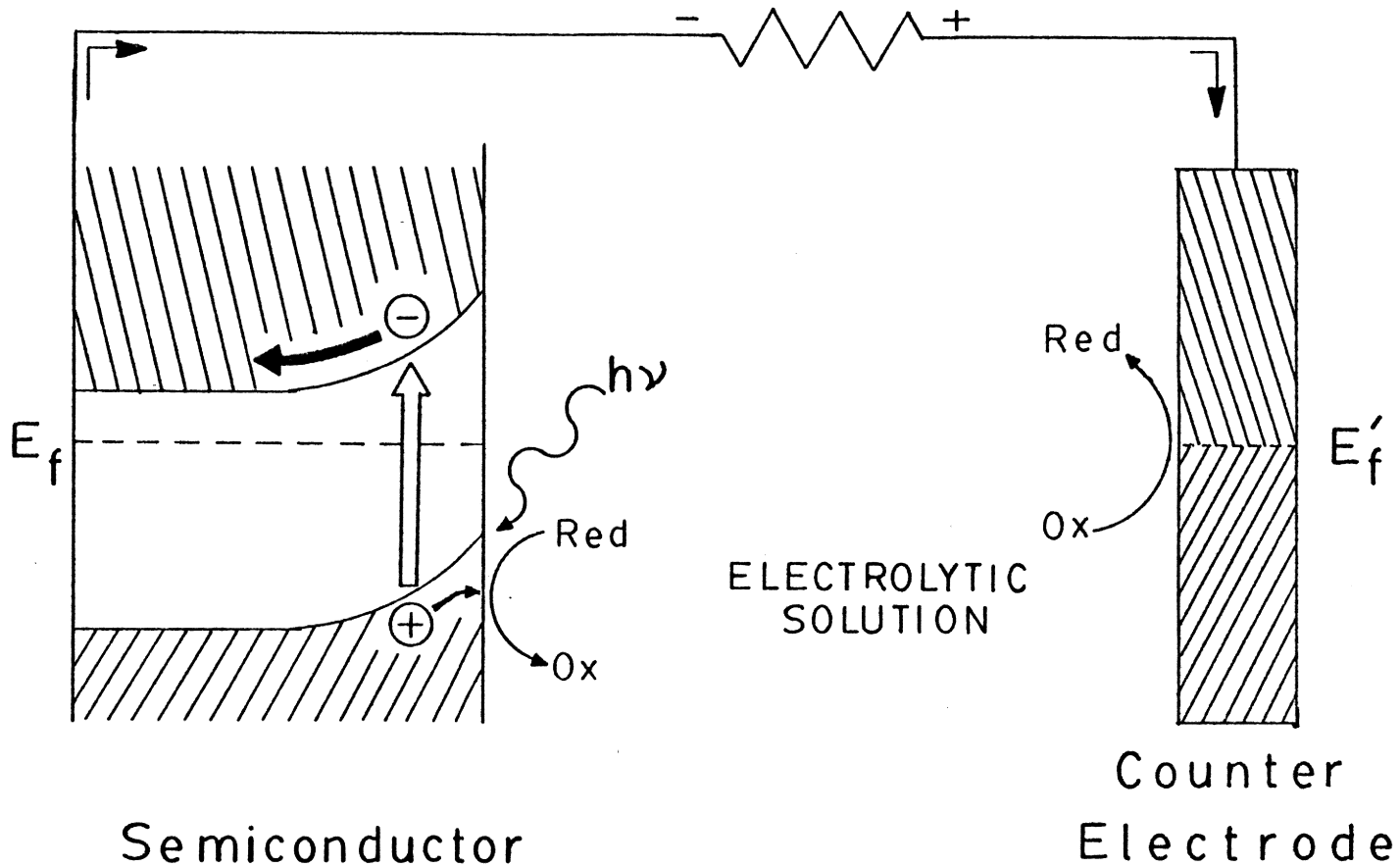

Operation of an SLJSC

Figure 13

solar cell.

C. Corrosion and Corrosion Suppresssion

Corrosion is the process of crystalline lattice destruction governed by chemical or other means, such as weathering, acid or alkali attack, atmospheric or water corrosion, or galvanic corrosion, just to name a few. (18) Because corrosion is so costly, much interest has been generated in studying it. The lack of funding hampers the development of semiconductor liquid-junction solar cells (SLJSC), which have a severe corrosion problem.

Recent work (19-22) has established a foundation for observing these corrosion processes in an electrochemical environment which mimics the working SLJSC. By observing electrochemical reactions occurring at the electrode/electrolyte interface, the involvement of electron transfer and/or ion transport under the influence of an electric field can help determine rates of corrosion.

These rates may be suppressed by non-electroactive coatings, in order to obtain better stability and longer lifetime of the SLJSC. These coatings should also permit electrochemical redox reactions to occur at the interface with minimal or non-existent destruction of the electrode surface. Corrosion suppression is the goal of the thesis.

Factors most influential on the rate of corrosion include potential, temperature, lattice structure of the electrode (particularly the exposed face), solution composition, and current. Of these, current, potential, and solution composition are considered to be most important. Hence, the discussion of electrochemical corrosion involving redox reactions under current flow conditions will be emphasized for the most part.

In my research, the rates of corrosion of n-type GaAs, and likewise the observance of corrosion suppression, have been measured by electrochemical methods, namely differential pulse polarography and rotating ring-disc voltammetry. The actual experimental techniques will be described in chapter two.

Corrosion in the electrochemical environment may result in the following two cases: dissolution and passivation.

Electrochemical dissolution of n-type GaAs involves the breaking of bonds at the surface by movement of electrons and holes. (23) On clean n-GaAs surfaces, this exchange of electrons and holes occurs at the interface via the triple layer. Figure 14 exhibits the physical destruction of the n-GaAs

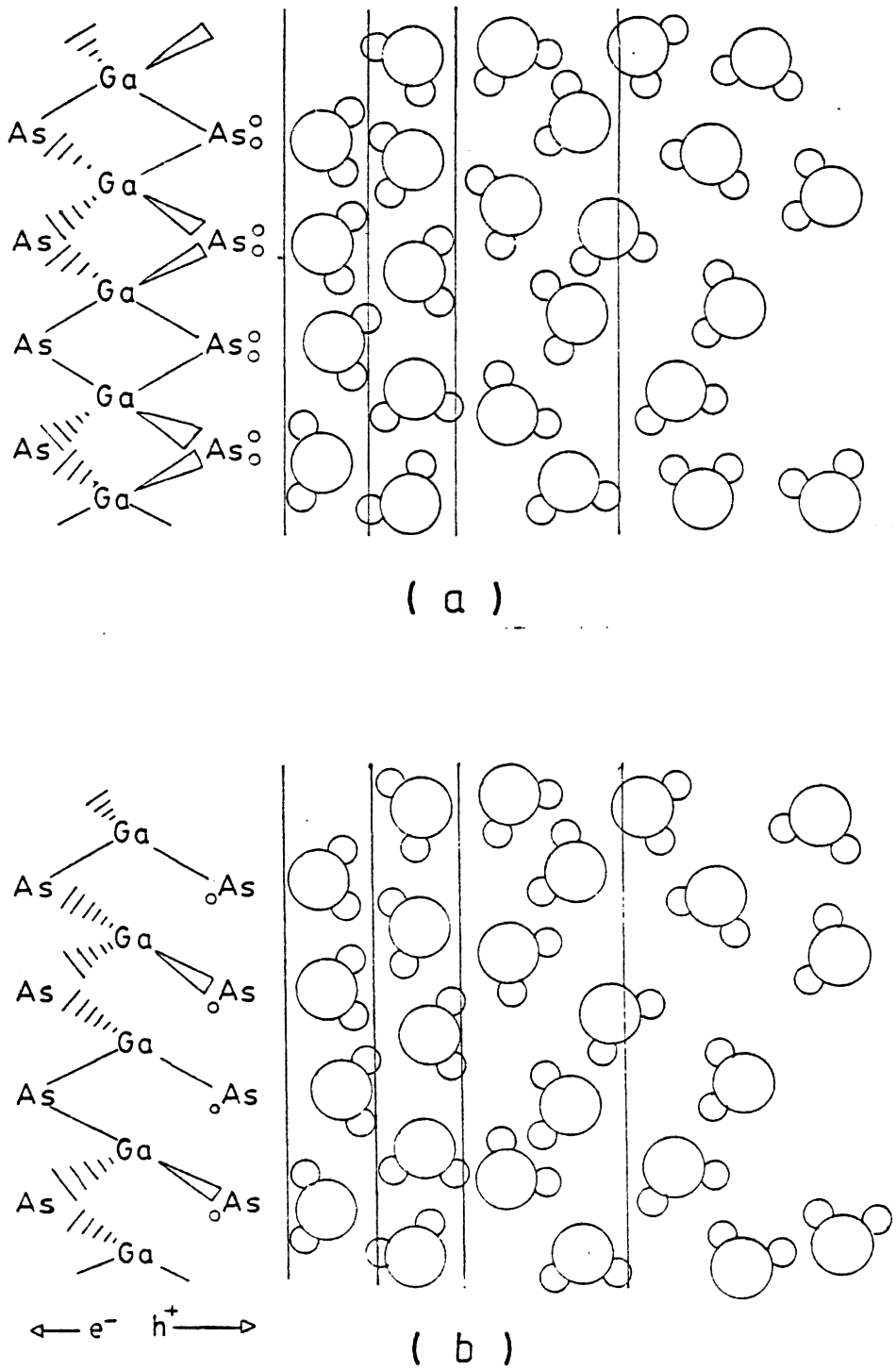

Figure 14

Electrochemical dissolution of n-GaAs by H_2O oxidative decomposition

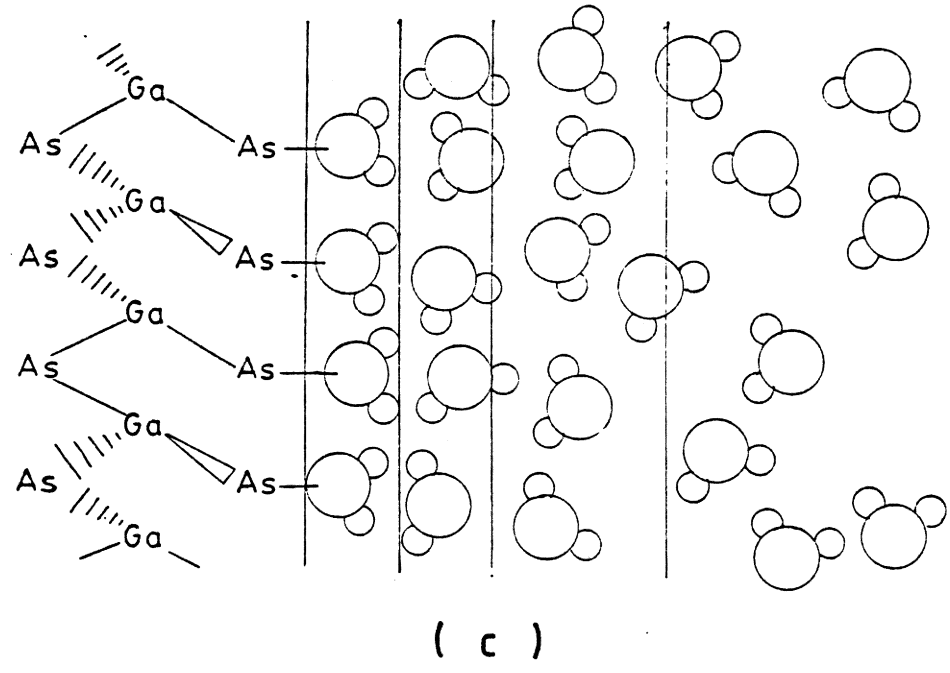

(c)

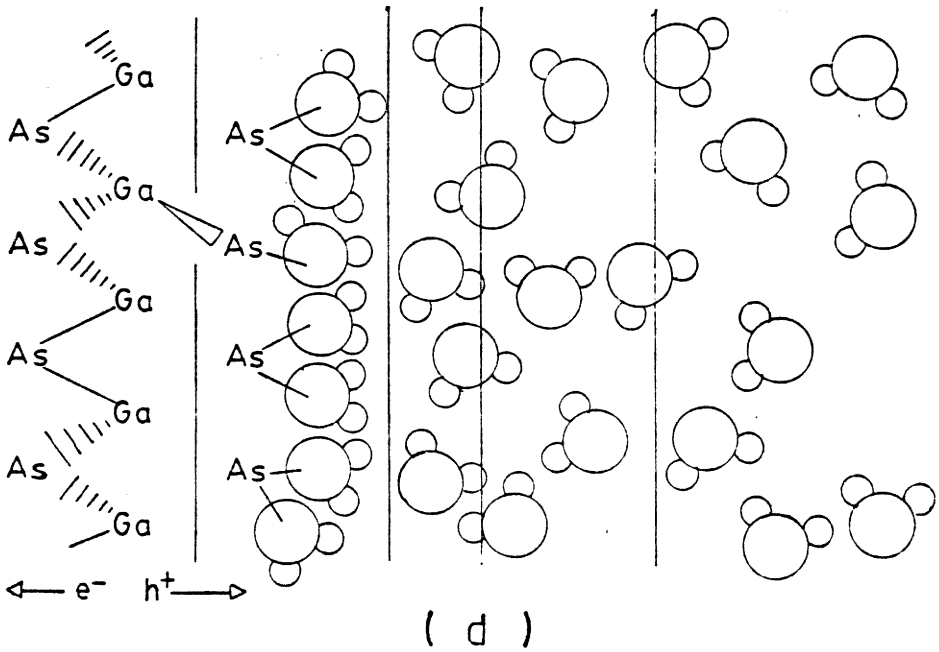

(d)

Figure 14 (continued)

semiconductor electrode surface via oxidative decomposition. At the surface (See Figure 14(a)) is a layer of surface atoms in contact with water molecules. The surface atoms average two free electrons per atom. These surface electrons can react with water molecules and form an oxide layer or they can be drawn back into the bulk by hole movement to the surface. (22) (24) As the holes approach the surface atoms, the bonds toward the bulk of the crystal are weakened. (See Figure 14(b).) The surface atom becomes a surface radical which is electron-deficient. It reacts with a water molecule, which attaches to the surface. (See Figure 14(c).) As more holes travel to the surface, another water molecule can be attached to the surface atom. (See Figure 14(d).) Eventually the surface atoms break away from the bulk and then move into solution as a solvated species. In order to have a continuous supply of surface charge carriers from the bulk of the crystal, a current must flow through the electrode and electrolyte via a circuit.

Passivation, a form of corrosion suppression, is the process which causes the rate of dissolution to decrease sharply. A blocking layer forms on the surface of the electrode. This condition can be achieved by altering the electrolyte composition in

order to form oxides which promote passivity. (25) Neutral pH results in formation of gallium and arsenic oxide on the surface. Evidence presented by Harvey et al. (26) (27) indicates the primary oxides are Ga_2O_3 and As_2O_3 in approximately equal proportion, whereas in acidic and basic media, anodic dissolution of the GaAs forms Ga(III) and As(III) species. (26) (28-30)

Next, attention is drawn to photoelectrochemical corrosion of n-GaAs, the basics of which are chemical corrosion processes. In photoelectrochemical corrosion of n-GaAs electronic excitation is induced via light absorption. (See Figure 15.) As discussed earlier, when a packet of light energy is absorbed by the n-GaAs semiconductor, electron-hole pairs are generated and the reduced species in solution is oxidized at the n-GaAs surface by holes. (22-24) (31) Secondary to this photocurrent generation is photo-induced chemical corrosion. At acidic or basic pH's, the photocurrent will remain constant (dissolution) (See Figure 15 (a)). A competition for holes between the redox reaction and the dissolution of the n-GaAs will occur and depends upon the energy levels of the products formed. (32) If the photocorrosion products form an oxide layer on the n-GaAs semiconductor surface, then condition (b) (passivation) will prevail and the photocurrent will

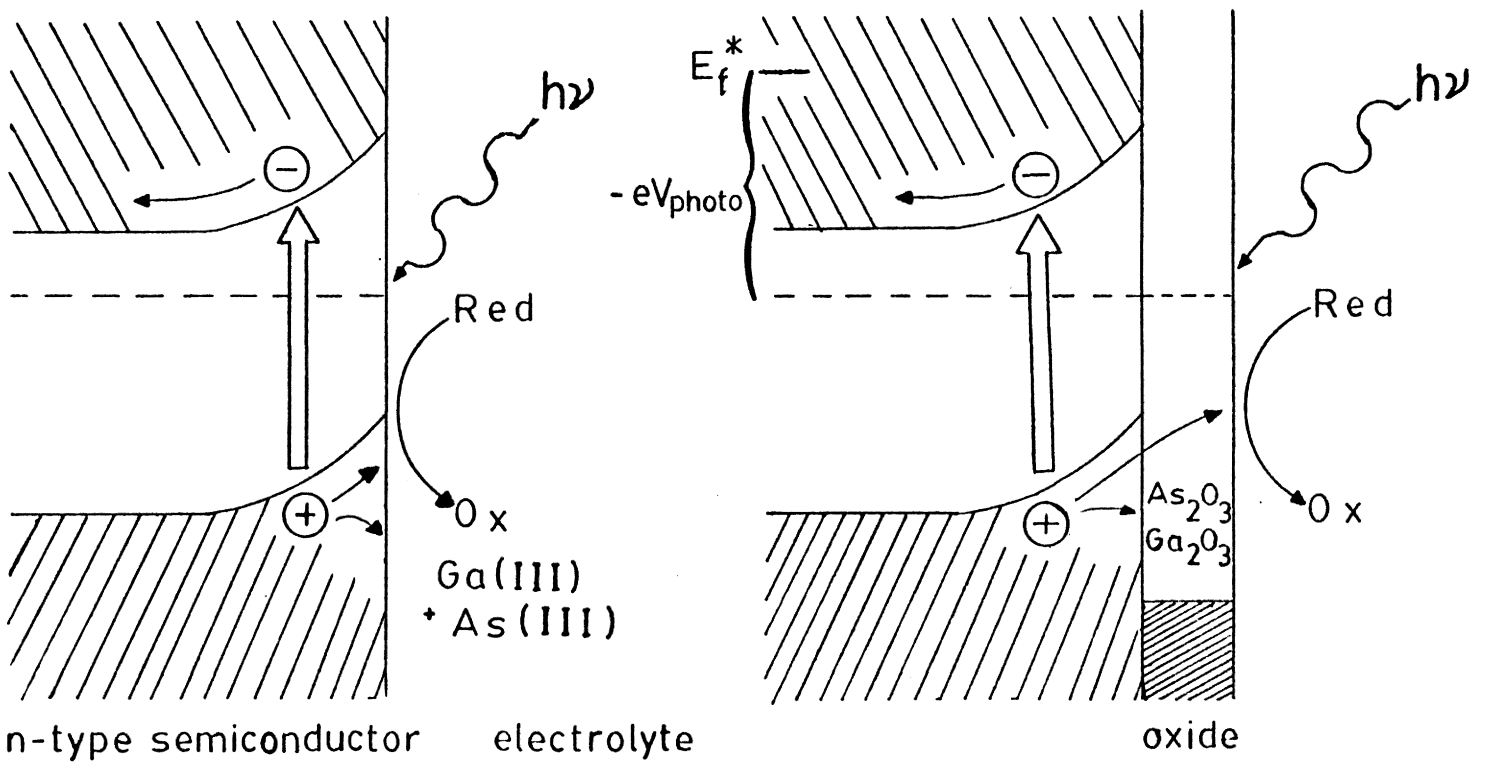

Photoelectrochemical Corrosion
with positive band-bending

Figure 15

decay with time. When this happens, more energy will be required for holes to reach to surface as they travel through the growing oxide layer. Thus, it can be seen that the oxide layer from the corrosion products functions as a protective layer against photocorrosion.

As explained earlier in this section, various items affect corrosion such as current, pH, electrode structure, potential, temperature, and solution composition. It has also been mentioned that the corrosion rate is controlled by the thermodynamics of the electrode and its corrosion products and by the corrosion layer formed on the electrode surface. Semiconductor corrosion may be prevented by using protective inorganic or organic coatings. (21) These protective coatings may be placed on the electrode surface either by vapor deposition techniques (such as silanization) or by evaporation of solutions (organic or aqueous). These techniques will be described more fully in the next section.

Several approaches are possible for measuring the rate at which a GaAs electrode corrodes during photocurrent generation. One method for measuring the corrosion rate is by weight loss experiments. In these the amount of n-GaAs electrode lost during an etching

process is related to the charge passed through the electrode. As an example, a loss of 5.0 mg of n-GaAs should result in an equivalent current generation of 20.02 Coulombs, based on $6e^-$ per GaAs oxidized. This should become obvious from the equation

$$GaAs \rightarrow Ga^{+3} + As^{+3} + 6e^-.$$

Using Faraday's constant,

$$\frac{(96484.6\ C/eq)\ (.0050g)\ (6\ eq/mole)}{144.64\ g/mole} = 20.02\ Coulombs$$

This is an effective yet simple technique.

In differential pulse polarography (which will be discussed in detail in Chapter 2), the concentration of As(III) in solution is observed as a function of charge passed. The corrected peak current for As(III) reduction is obtained before and after passing photocurrent through the electrode, and then converted to the amount of As(III) released via a calibration plot.

In summary, chemical corrosion of n-GaAs is caused by very basic and very acidic solutions. Electrochemical corrosion requires holes arriving at the surface for n-GaAs and photoexcitation to produce the holes. Also, for the corrosion to occur, the potential applied needs to be more positive than the flatband potential; corrosion is not observed at

potentials negative of V_{fb}.

In comparing the dissolution method with that of passivation, dissolution generates soluble products (Ga(III) and As(III)) in acidic and basic media. Passivation produces insoluble products which are mainly situated on the surface of the photoelectrode. These products form at intermediate pH's and there is no potential dependence of the oxide layer. Finally, the dissolution process allows a steady photocurrent in comparison to the passivation process, in which the current peaks and continues at low levels.

D. Work by Others

With the advent of the electronics industry, in particular transistors, much interest has been generated in semiconductor research. (22) (23) (29) (33-35) This surge of interest is not just limited to products such as high-speed electronic devices but it also extends to other areas such as photoelectrochemical cells, photovoltaic devices, and optical communications. (31) (36) (37) Semiconductor use offers advantages over conventional methods for power generation in certain fields, such as space and isolated communities, where power plants would be too costly to build or where batteries, in the long run, would need numerous replacements.

Although semiconductors have advantages, they also have problems, especially those used in photoelectrochemical cells. As pointed out in the previous section, corrosion is the major problem, but there are other troubles. Interface properties, composition, and uniformity depend on oxide preparation methodologies, such as thermally-, plasma-, or electrochemically-grown crystals. (34) These will affect the optical properties. In conjunction with these difficulties, crystal surface defects introduce new surface states making irregular surface points

where electron exchange is hampered or enhanced, depending on the type of doping. This eventually will result in altered etched lattice faces. (38)

Kelly and Notten, in their recent publication (26), studied the effects of surface charging in relation to n-GaAs photoanodic dissolution. They argued that the dissolution of semiconductor electrodes may be due to surface or interfacial charge localization states, in which the charge distribution between the electrode and the electrolyte influences the dissolution rate. Futhermore, they claim that interface states can act as intermediates in the dissolution reaction. Finally, they conclude that the n-GaAs/electrolyte interface localizes a high charge density during the photoanodic dissolution process. These results concur with those of Elliott and Regnault. (39) Along with the charge density localization case, they add that pH is an important factor to consider. Elliott and Regnault assert that with EDTA in a pH 4.5 electrolyte there exists negligible oxide solubility, at pH 10 and above, uneven electrode dissolution results, and at pH 2.5 the EDTA complexes with gallium at the surface. But one advantage they have uncovered is that the oxide film formed can act as a protective barrier to reduce

further film growth. Also, this film can be readily removed by dilute NH_4OH.

In a recent publication by Frese et al. (22) they show that only a small amount of the exposed electrode surface is defective. These are the sites at which corrosion is most likely to occur. At the defect-free regions of the GaAs semiconductor stabilization against corrosion is supported by redox couples in solution. They further stress that these defects alter the surface state hole energy levels, which can lead to weakening of the bonds towards the bulk of the crystal. This, in effect, results in a surface which is more susceptible to corrosion.

Finally, Wrighton et al. (30) state that although the production of photocurrent from GaAs may be stable, it does not mean that the semiconductor is. By utilizing a redox couple such as Te^{-2}/Te_2^{-2} (which has its redox energy above E_v), the rate of Te^{-2} oxidation is then competitive with the rate of photoanodic dissolution. This effect was confirmed by Heller and Miller (40), who used the Se^{-2}/Se_2^{-2} redox couple on n-GaAs. Their results indicate that although the anodic reaction of $2Se^{-2} + 2h^{+} \rightarrow Se_2^{-2}$ dominates, photocorrosion still occurs.

Polymer coatings may be deposited by

electrochemical polymerization. We will consider only work done with non-electroactive coatings; work using electroactive polymers has been reported. (41-49)

Work in this area has been accomplished by Parkinson and Canfield (50) in which they blocked recombination centers by layering the electrode with bulky molecular species. Also, Bard and others (35) attempted similar electrochemical polymerization with OPD (o-phenylenediamine) on n-WSe_2 electrodes. The success of two polymerization cases was pH dependent with passivation increasing when pH was decreased. Thus, the OPD coating proved to be stable after further testing by redox reactions.

II. EXPERIMENTAL

A. Preparation of solutions

1. As(III) standard solutions were prepared by dissolving reagent grade $NaAsO_2$ in deionized, distilled water.

2. The acid solutions (HCl, HNO_3, and H_2SO_4) were prepared using distilled, deionized water and reagent grade acids, respectively, and then calibrated via a Fisher Accumet model 610A pH meter. Some HNO_3 solutions contained 0.1 M KNO_3 to increase conductivity.

3. The tetraethylammmonium perchlorate (TEAP) solutions were prepared by drying spectroscopic grade acetonitrile with activated molecular sieves and then by passing them through a chilled (-20°C) activated alumina column. The TEAP was heated to 150°C overnight to dry and immediately dissolved in the dried CH_3CN.

4. The Fe(II)/Fe(III) solutions were prepared by dissolving ferrous sulfate or ferric sulfate, respectively, in HNO_3/0.1 M KNO_3.

5. The Fe(II)/EDTA solutions were prepared by dissolving ferrous sulfate in 0.100 M EDTA. The pH was adjusted to 7.00 by additions of electrolytic grade NaOH pellets and reagent grade H_2SO_4 and NH_4OH.

B. GaAs Crystal Preparation

A 1:1 95% H_2SO_4/30% H_2O_2 mixture was used to etch the surface of the GaAs crystal to remove any oxidation products from the surface. Etching time was thirty seconds. It was discovered that 70% H_2SO_4 deposited a carbon film on the crystal. Next, HF was used to remove any oxide layer present. The GaAs crystal was then rinsed with deionized, distilled water and methanol after each etch.

C. Mounting of GaAs Crystal

The back of the GaAs crystal was polished with alumina slurries to obtain an area for electrical contact. Sometimes scratching the surface with glass aided the electrical contact. Gallium-indium eutectic formed the ohmic contact to the crystal. The crystal (obtained from IT&T) was then mounted on either a glass tube of slightly larger diameter or onto a brass ESCA mount, depending on usage. Shell Epon 828 and PACM-20 were combined to produce the epoxy (which is resistant to HF) to be spread on the electrode end of the mount. In the glass mount a copper wire was used to maintain contact for experimental measurements, whereas the brass ESCA mount itself provided contact. (See Figure 16.)

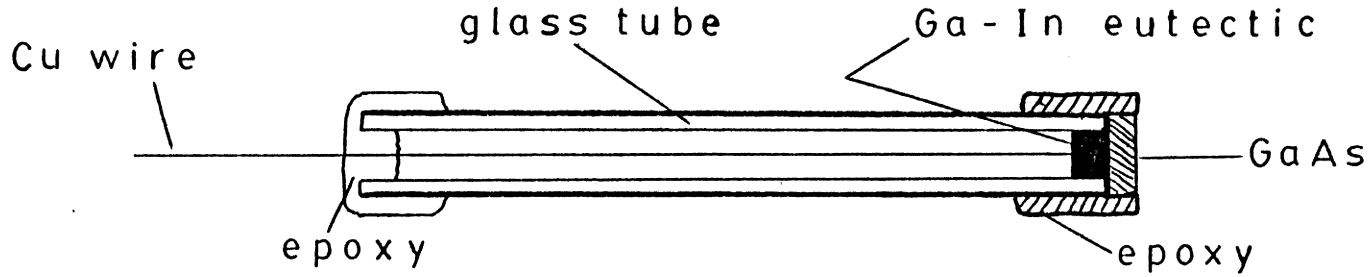

(a)

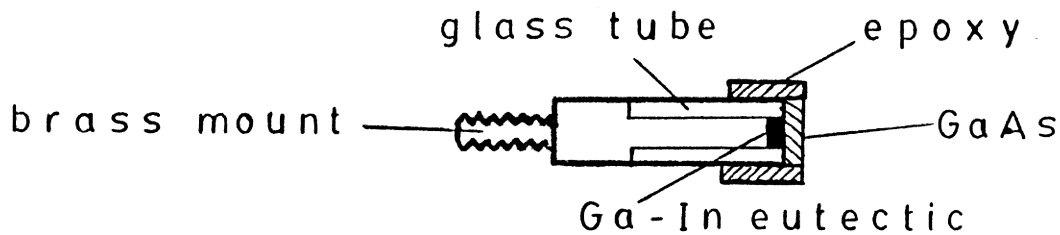

(b)

GaAs Electrodes

Figure 16

D. Cleaning and Preparation of Equipment

1. All glassware was cleaned first by soap and water, then by soaking in hot concentrated H_2SO_4 and hot concentrated HNO_3, and finally by rinsing with distilled, deionized water. The glassware was dried by placing it in an oven at 150°C.

2. Plastic surgical tubing, used in the dropping mercury electrode set-up (Figure 17), was boiled in 2 N NaOH for 75 to 120 minutes to remove any plasticizers in the tubing. It was then rinsed with distilled, deionized water to remove any NaOH and residual plasticizers and then air-dried.

3. The capillary tube was cleaned by soaking in hot concentrated HNO_3 to dissolve any Hg, waste, or films. Next, a methanol-water rinse was aspirated through the capillary.

4. Figure 17 is representative of the basic experimental set-up used.

E. Silanization

The silanization with $SiCl_4$ was carried out according to procedures established by Rathnapala S. Vithanage. (11) (51)

F. Voltammetric Techniques

1. Photocurrent Etching

The equipment was set up as shown in Figure 17.

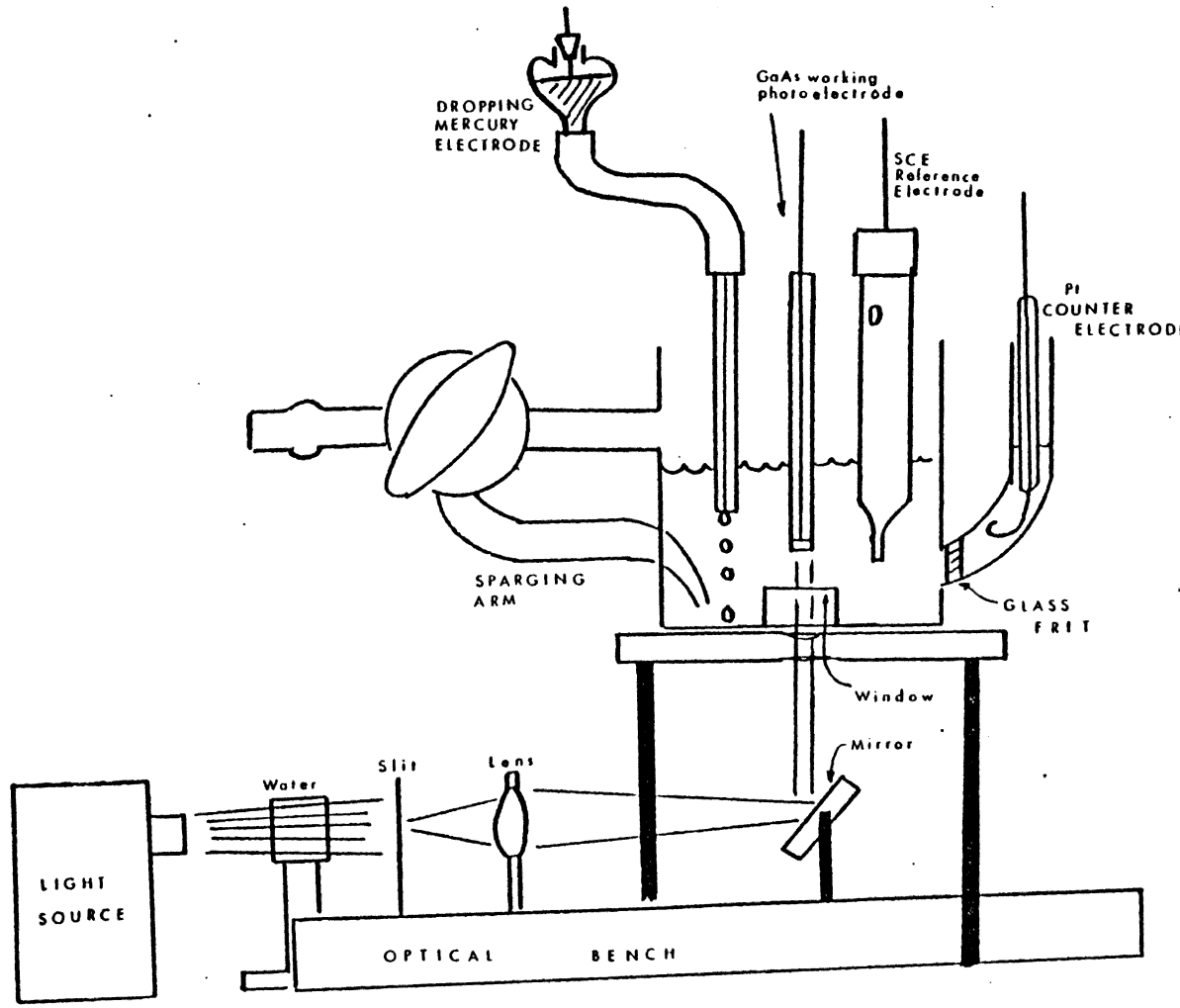

EXPERIMENTAL SET-UP

Figure 17

Thirty milliliters of pH 1.00 HNO_3/0.1 M KNO_3, H_2SO_4, HCl, or NaOH was added as the electrolyte to the electrolytic cell. A volume of the same electrolyte was added to the counter electrode cell compartment so that the levels were equivalent in height. Argon was bubbled through the solution for 10 to 20 minutes to remove any O_2, which ordinarily interfered with the oxidation/reduction etching.

The electrode used was checked as to whether it was coated or cleaned before etching. The inlet arm on the cell was positioned to form an argon blanket over the solution. A PAR Polarographic Analyzer and an x-y recorder were used to acquire the data.

The xenon lamp was utilized as the light source. A black box was placed over the electrolytic cell in order to exclude room lights.

2. Sampled DC Polarography

Sampled DC polarography has been established as an electroanalytical tool for some time now. (52) (53) The basic principle of sampled DC employs the current flow at a dropping mercury electrode (DME) as a function of potential. The current is measured only once at a point where the faradaic current exists as the major component. Figure 18 illustrates the current-time curves for sampled DC polarography. The

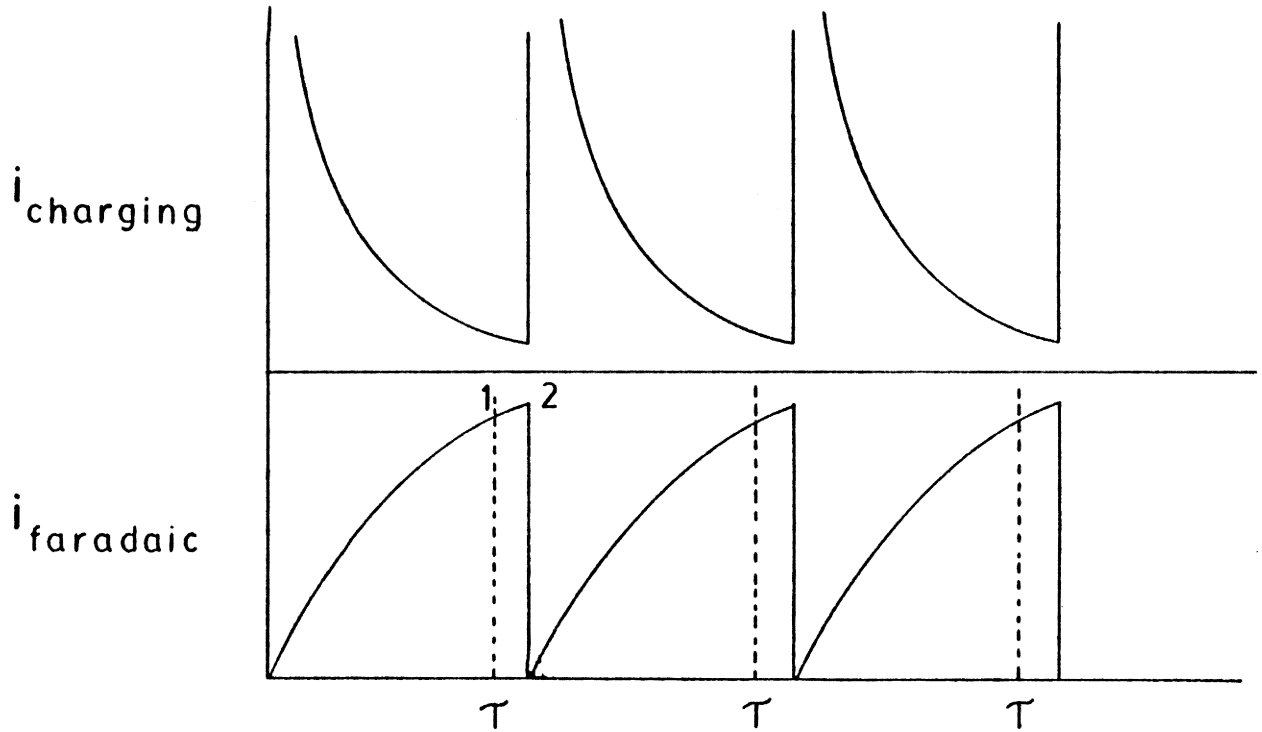

Current-Time Curves
for Sampled DC Polarography

Figure 18
1. Current sampled
2. Drop dislodged

dashed line indicates that the current is sampled near the end of the droplife; i.e., the last 16.7 ms. Figure 19 depicts a simple sampled DC polarogram. As it can be seen, the plateau region for the reduced species B consists of the residual current at B, $i_r(B)$, plus the diffusion limited current of B, $i_d(B)$. Simple extrapolation of the residual current allows measurement of $i_d(B)$ and hence an estimation of B's concentration.

3. Differential Pulse Polarography

In differential pulse polarography, a pulse of a few millivolts is applied at regular intervals on a slowly changing polarized voltage. (54) A differential output is the result of measuring the difference between two currents before and after the pulse. (53) In this technique a peak-shaped curve of Δi versus E is generated in the voltammogram. This result can be observed in Figure 20. Theoretically, the maximum in Δi, the difference of measured current sampled during the lifetime of a drop, occurs at $E_{1/2}$, the half-wave potential. The pre- and post-portions of the diffusion-controlled wave are symmetrical. (55)

The current is a function of the redox concentrations, the electrode area, and the redox diffusion coefficients. (56)

1. $E_{\frac{1}{2}}$ (B)
2. $E_{\frac{1}{2}}$ (C)
3. i_d (B)
4. i_d (C)
5. i_r (B)
6. i_r (C)

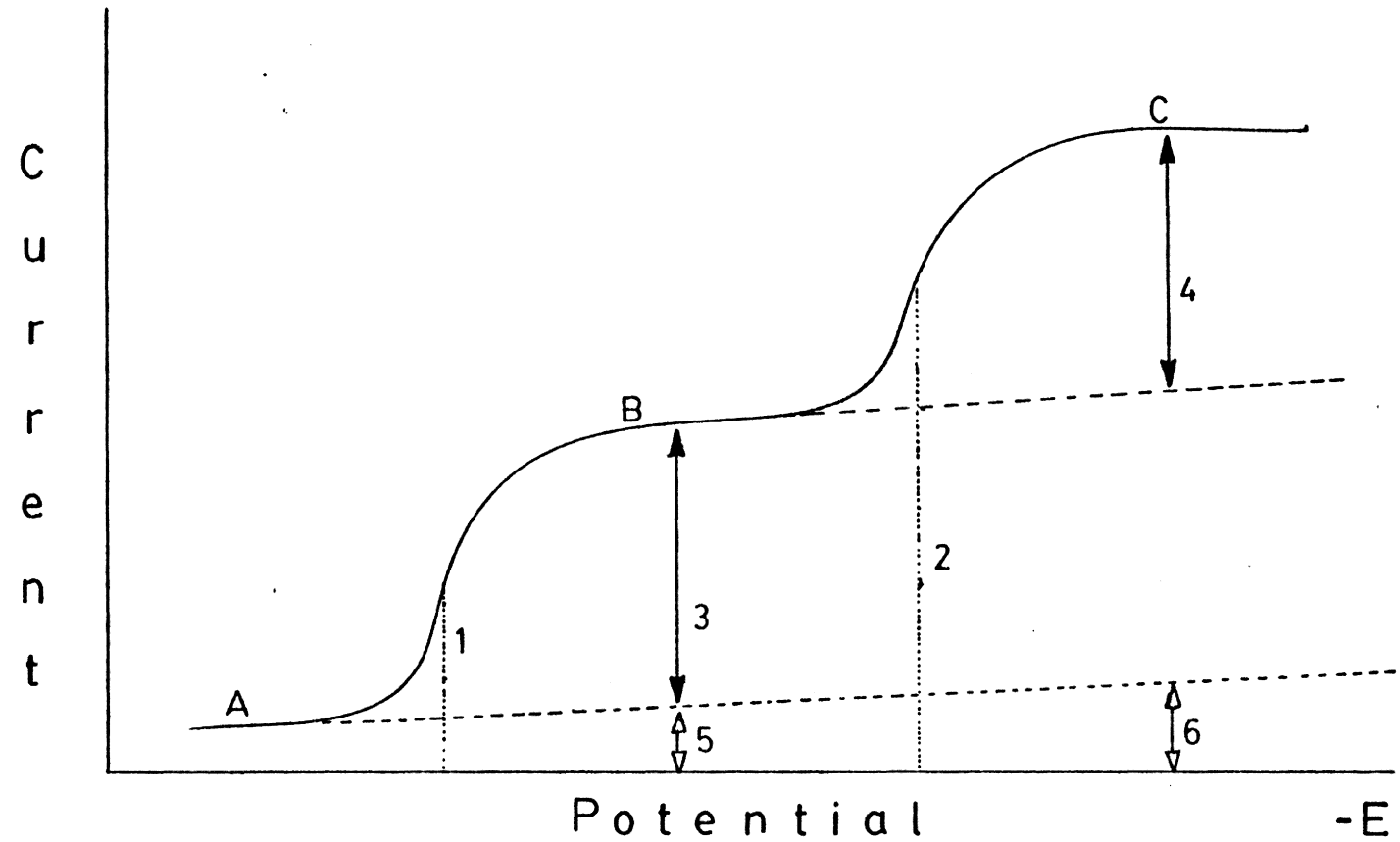

Sampled DC Polarogram

Figure 19

A Theoretical Differential Pulse Polarographic Wave

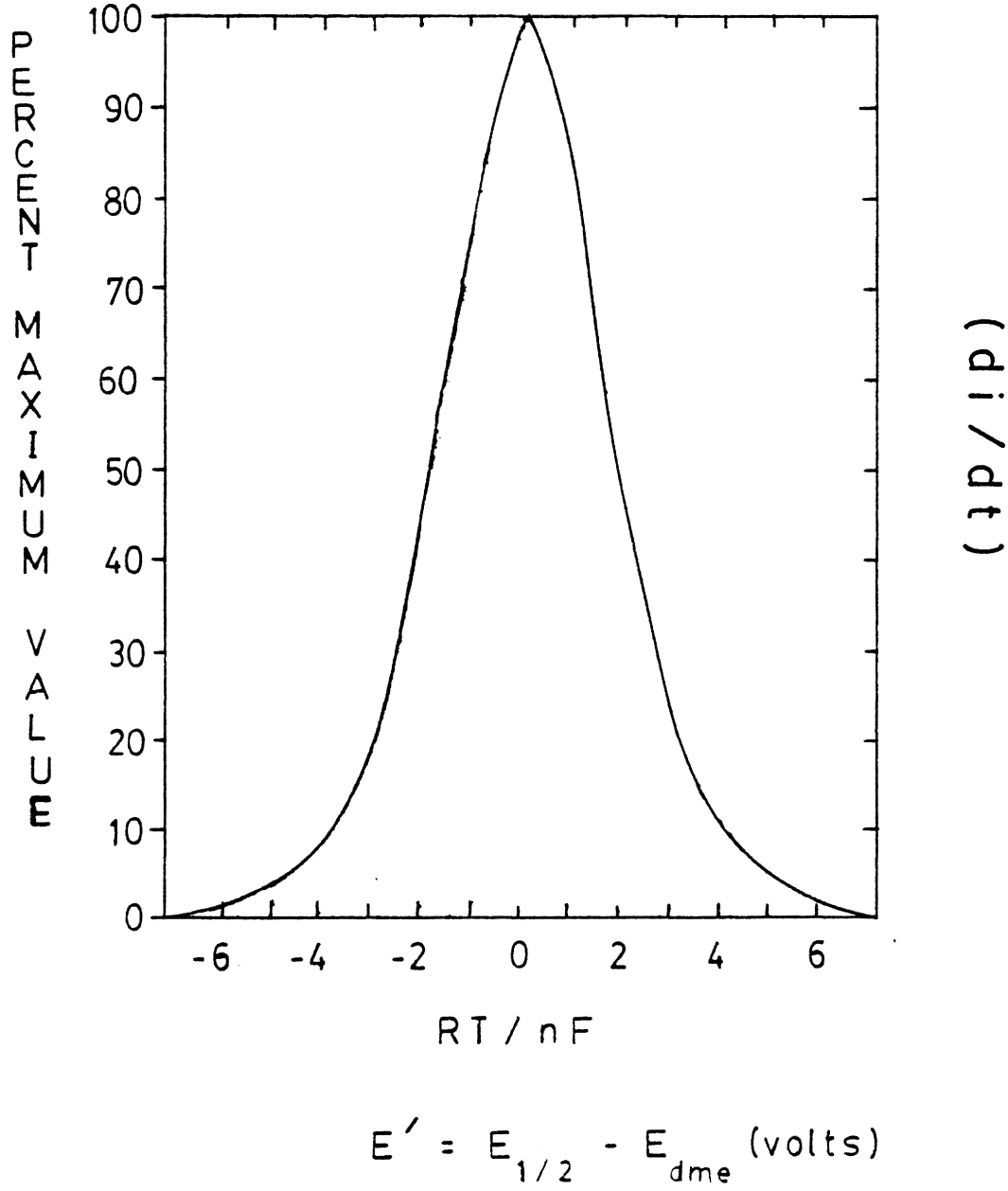

Figure 20

Figure 21 (57) shows the potential-time plot used in DPP: a potential ramp with the repeated pulse added. While the potential is steadily increased in a linear fashion with time, several events occur. At point A the previous mercury drop has been knocked off and a new one begins to grow until point F, the point of maximum drop growth. The entire lifetime of the mercury drop, A to F, is dependent on the programming of the dropknocker, which can vary the lifetime from 0.5 sec to 5 seconds. The PAR 174A circuitry for DPP samples the current 16.7 ms prior to pulse application, B to C. (57) The current obtained is converted into a voltage analog and is stored in a sample-and-hold circuit. When the current is finished being sampled, a pulse of predetermined magnitude (5, 10, 25, or 50 mV) is applied at point C and thus is observed in the transition to D. The second current measurement of 16.7 ms duration is taken at E, 40 ms into the pulse, and is also converted into its voltage analog. The first measurement is then subtracted from the second and is plotted via a recorder to yield $\Delta i/\Delta E$. The curve approximates the first derivative of a sampled DC voltammogram.

When a sampled DC pulse polarogram is overlaid with a differential pulse polarogram, as in Figure 22,

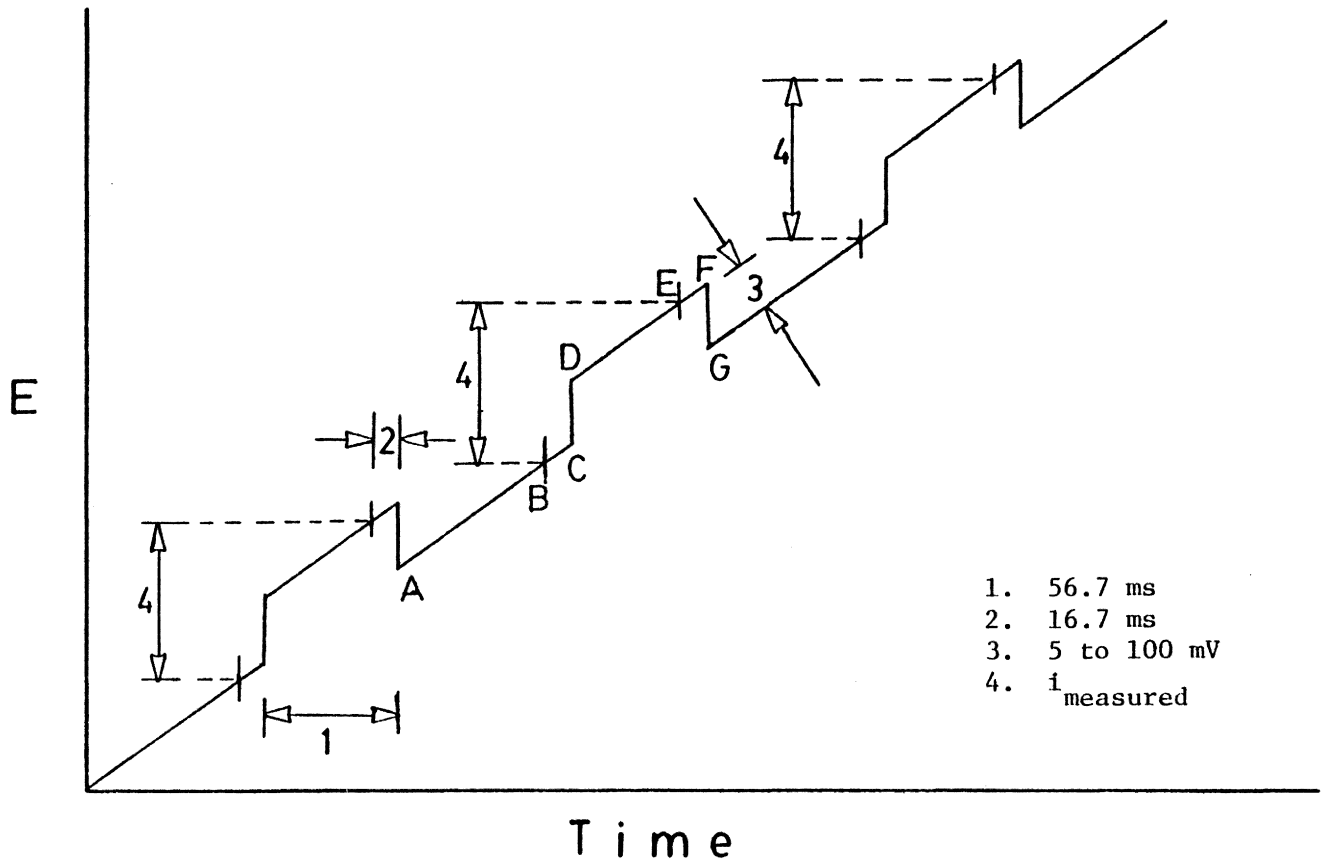

Potential excitation waveform used in differential pulse polarography

Figure 21

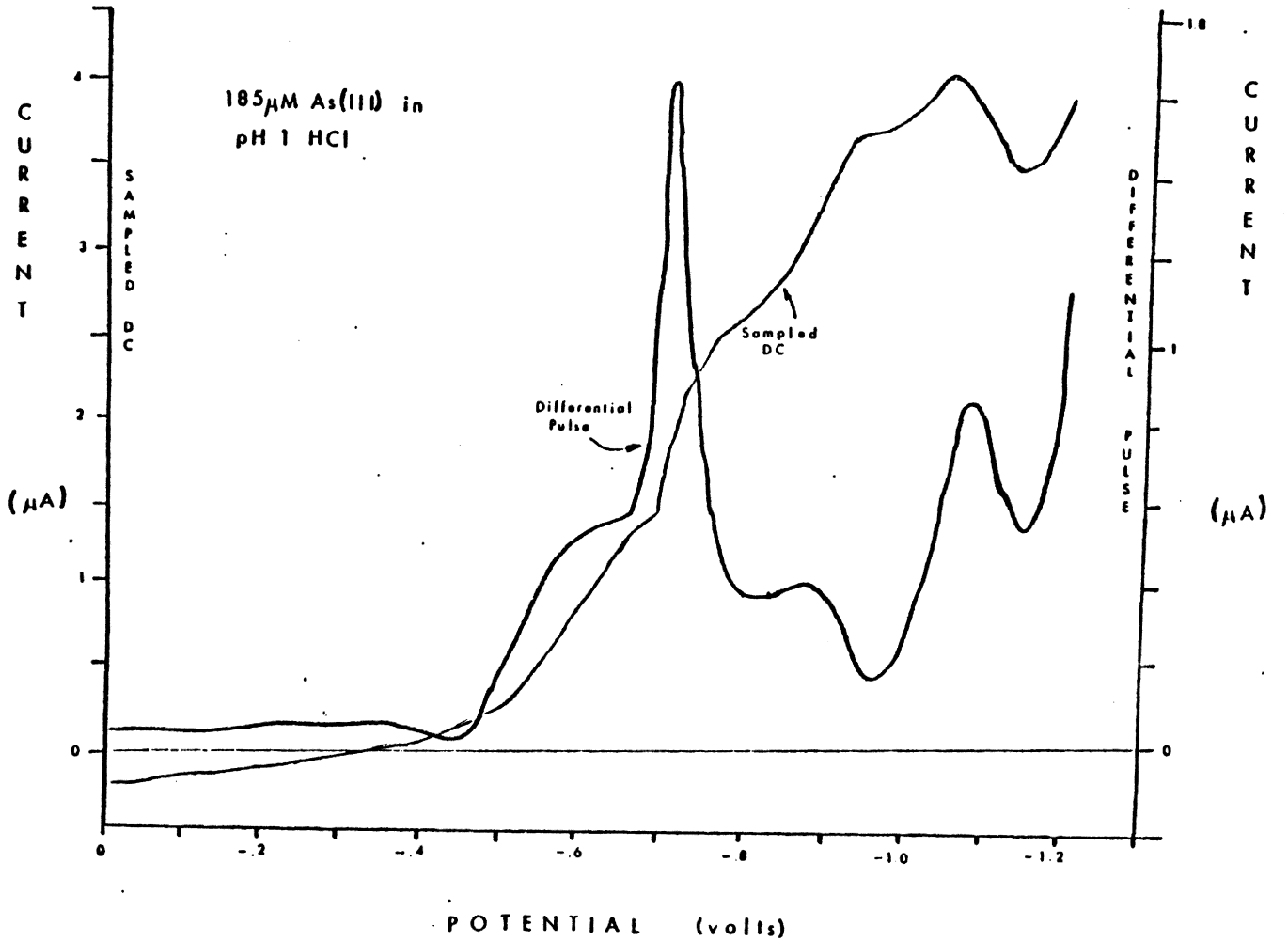
185μM As(III) in
pH 1 HCl
CURRENT
SAMPLED DC
(μA)
DIFFERENTIAL PULSE
CURRENT
(μA)
Sampled DC
Differential Pulse
POTENTIAL (volts)

Figure 22

a comparison of sensitivities between the two can be made. The figure shows a sampled DC and differential pulse polarogram for As(III) in HCl. The sampled DC pulse polarogram is not as sensitive as the differential pulse polarogram with all conditions (except current sensitivity) being equal. In the differential pulse polarogram the first peak corresponds to a $3e^-$ reduction of As(III) to As^0, and the third peak is yet a further reduction to AsH_3. (58) The second peak is a polarographic maxima and disappears at arsenic concentrations less than 8 μM. (58)

4. AC Voltammetry

In alternating current (AC) methodologies a small AC signal is superimposed upon a simple DC potential ramp and applied to an electrochemical cell. (13) (59) (60) The AC peak-to-peak voltage applied usually lies between 1 and 30 mV. (61) Although most AC techniques are used in the sweep mode, various stationary DC potentials were applied in order to determine the flatband potential of the GaAs semiconductor in an acidic media.

Figure 23 presents the basic electronic circuitry utilized in this analytical method. The PAR 176 and the PAR 173 acted in conjunction as the

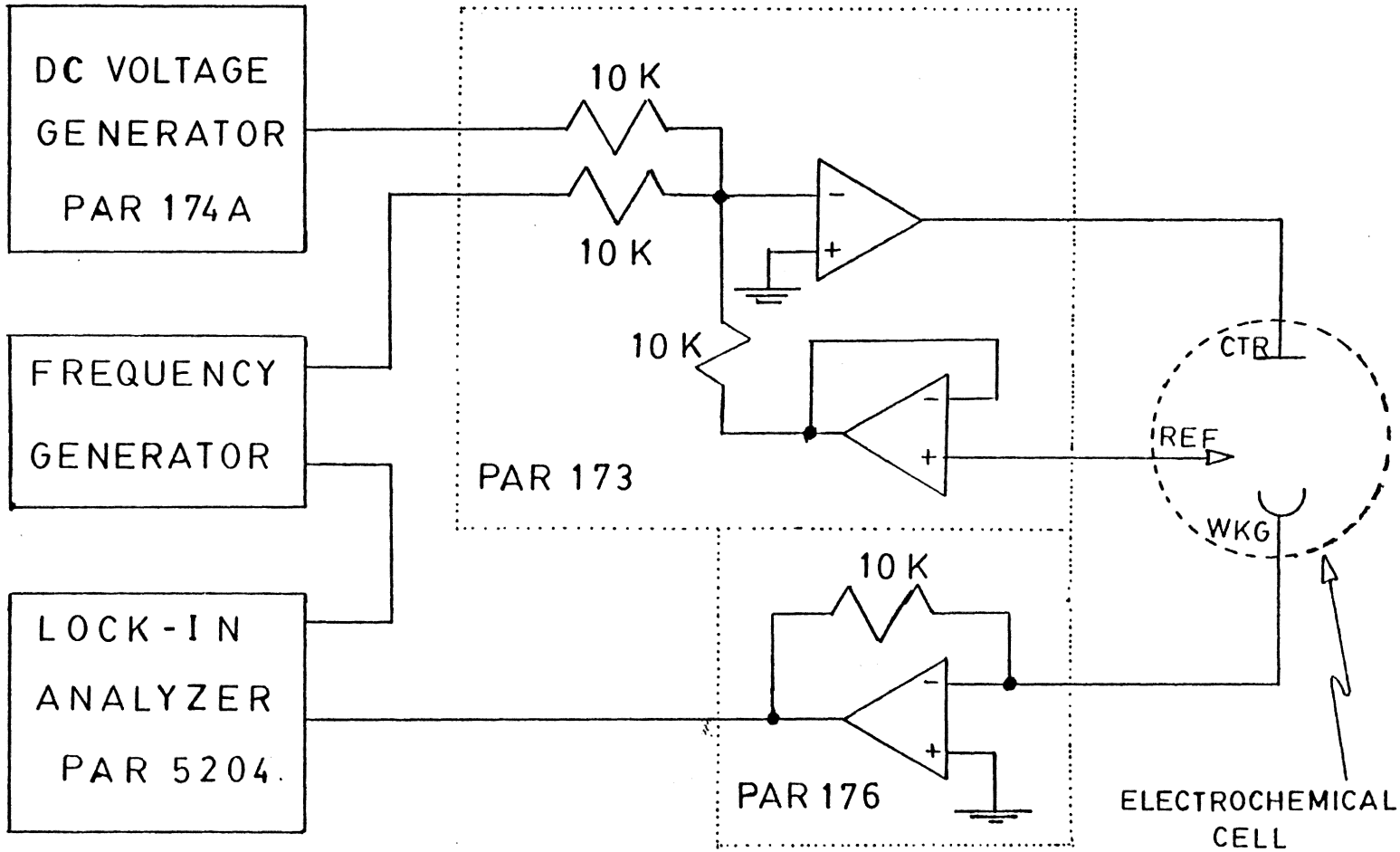

Electronic Schematic for AC Voltammetry

Figure 23

potentiostatic circuit, and the PAR 5204 displayed the in-phase, i_0, and out-of-phase, i_{90}, components with respect to the applied potential from the PAR 174A. These values are then utilized in determining the resistance and the double layer capacitance in the electrochemical cell. From this information a plot of $1/C^2$ versus $E_{applied}$ (a Mott-Schottky plot) will yield the flatband potential.

5. Rotating Ring-Disc Voltammetry

a. Mounting of GaAs crystal

The GaAs crystal was cleaned and polished as described in Section C of this chapter. Again, gallium-indium eutectic formed the ohmic contact to the crystal. The crystal was then mounted on an interchangeable stainless steel disc electrode mount. Bathtub silicone was then placed around the circumference of the upper portion of the mount, which was then placed in the ring-disc assembly and adjusted until flush with the surface. The silicone was allowed to cure overnight. The assembly's radial face was then soaked in distilled, deionized water to remove any excess acetic acid, which was released during curing. Figure 24 (62) represents an illustration of the rotating ring-disc electrode assembly as obtained from the Pine Instrument Company.

Model AFDTI36 Interchangeable Disk Electrode For AFASR

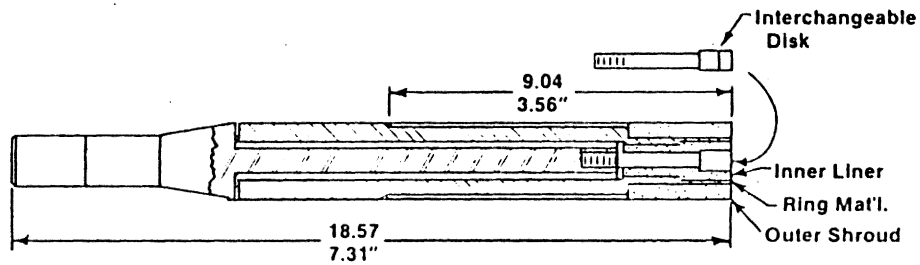

NOTE: Inner Liner Can Be EPOXY; KEL-F; or U-CUP INSERT. Outer Shroud Can Be EPOXY or TEFLON

Figure 24

b. General Theory

The rotating ring-disc electrode is a powerful method for analyzing the kinetics of homogeneous electrochemical reactions in solution. (63) It can be used to determine some kinetic parameters associated with the electrochemistry involved. The electrode is rotated, thereby setting up convective flow by rotational forces. As this occurs, solution flows towards the disc and then across the ring, which is downstream from the disc. During rotation the surface concentration of the reactant being analyzed is assumed to be uniform.

The potentiostat used to analyze data was modified to accommodate two working electrodes. How this was accomplished and calculation of the collection efficiency are covered in the next chapter.

6. Voltammetric Photooxidation of Phenol and DVB

The basic experimental set-up is given in Figure 17. The reference electrode can be either in the same compartment as the working electrode or in a separate one connected by a fine glass frit.

Cyclic voltammetry, in conjunction with a light source, is utilized to covalently attach or adsorb phenol (35) (64-68) (or DVB) to the gallium arsenide semiconductor surface. Thus, a non-electroactive polymer coating can be

synthesized by this technique. (69) The light source is utilized to aid in the generation of holes needed to oxidize DVB or phenol; the GaAs is blocking otherwise. The deposition solution must consist of a basic organic electrolyte, preferably CH_3CN or CH_3CH. (The high dielectric constant of these two solvents will favor a separation of charges, thereby generating phenolate or DVB radicals.) The cyclic voltammogram of phenol oxidation is represented by Figure 25.

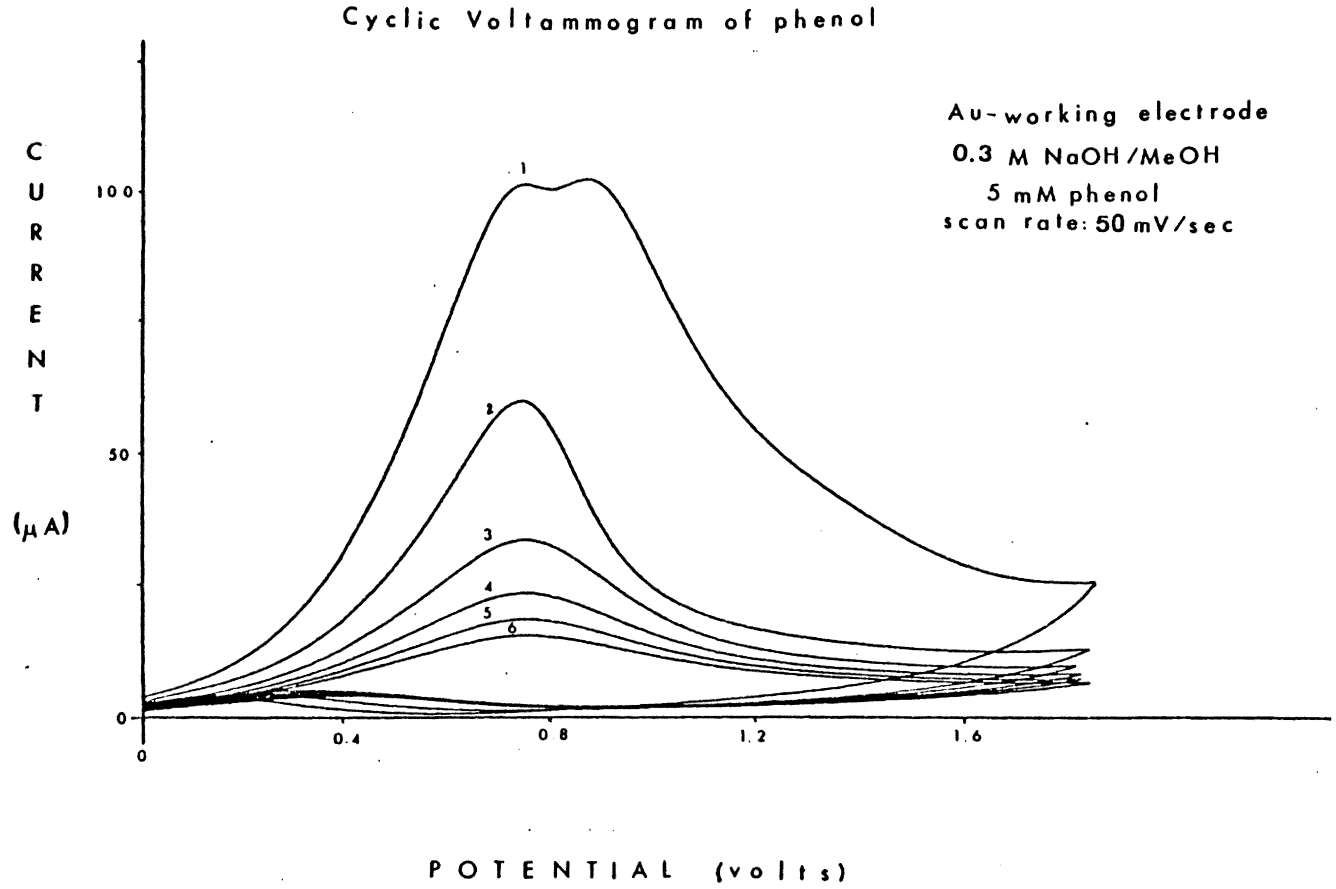
Cyclic Voltammogram of phenol
Au-working electrode
0.3 M NaOH/MeOH
5 mM phenol
scan rate: 50 mV/sec
CURRENT
(μA)
100
50
0
0
0.4
0.8
1.2
1.6
1
2
3
4
5
6
POTENTIAL (volts)

Figure 25

III. Results and Discussion

A. General Properties of n-GaAs

The main goal of my research was to suppress corrosion on the semiconductor electrode surface. This goal was attempted by placing a non-electroactive coating on the n-GaAs semiconductor electrode surface. Haller and others (36) (51) (70-74) have found that the corrosion rate on semiconductor electrodes may be suppressed by covalent attachment of non-electroactive layers on the surface. The objective was (a) preventing or reducing rates of surface corrosion of the n-GaAs semiconductor electrode surface, (b) promoting redox reactions of iron, iodide, or ferroin redox couples through the adsorbed polymer layer, and (c) allowing current levels of coated electrodes to be near those of uncoated electrodes.

An IR spectrum was attempted on (Aldrich Chemical brand) GaAs powder which was pressed into a pellet. Due to inhomogeneous surface conditions and excessive light scattering, an IR spectrum of reasonable quality could not be obtained.

X-ray photoelectron spectroscopy was employed to analyze the gallium arsenide crystal surface. After etching the surface for one minute in a warm (~35°C) $H_2SO_4:3H_2O_2:H_2O$ mixture and then rinsing with

deionized, distilled water, the surface was examined by XPS. (See Figures 26 and 28.) It was then re-examined after a one minute etch in concentrated HF at room temperature and thorough rinsing. The data (Figures 27 and 29) revealed the loss of an oxide layer after the HF etch. This loss was indicated by the attenuation of the peaks at binding energies 44.9 eV and 167.5 eV. The change at 44.9 eV was a result of the loss of the As(3d) state from As_2O_3 on the surface. The As(3d) peak at 42.1 eV corresponds to the binding energy of the As(3d) state in the GaAs crystal. As for Figures 26 and 27, the peak observed at 161.5 eV corresponds to a Ga(Auger) peak, whereas the peak at 167.5 eV corresponds to a Ga(Auger) peak in Ga_2O_3. These results concur with those observed by Mizokawa et al. (75) Other scans, not shown here, disclosed a four-fold decrease in the O(1s) peak height at 532 eV after the HF etch. Finally, the oxide peak height at 46.5 eV was reduced to a negligible value while the peak height for the As(3d) state at 42.5 eV remained basically at the same level of intensity.

The next property investigated was the flatband potential, V_{fb}. Two methods were utilized to determine the flatband potential: AC voltammetry,

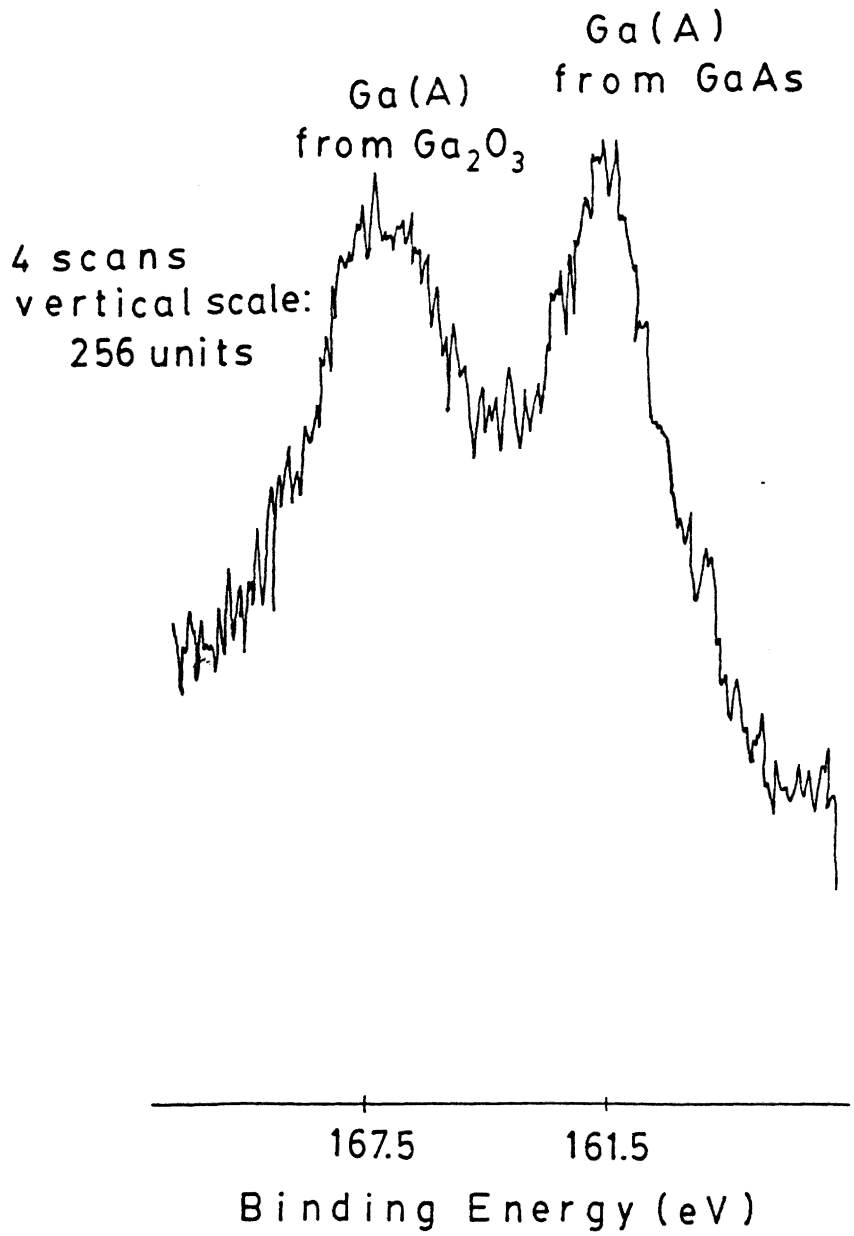

Figure 26
ESCA of oxidized GaAs crystal - Ga(A)

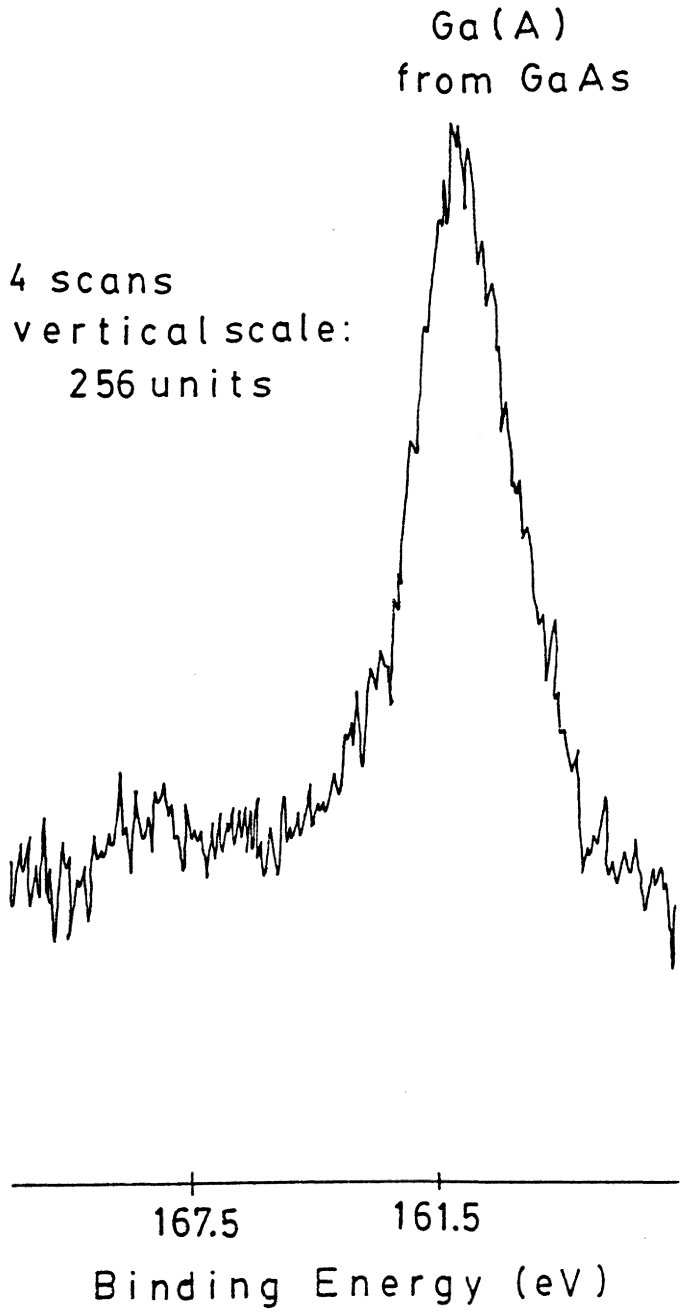

Figure 27
ESCA of cleaned GaAs crystal - Ga(A)

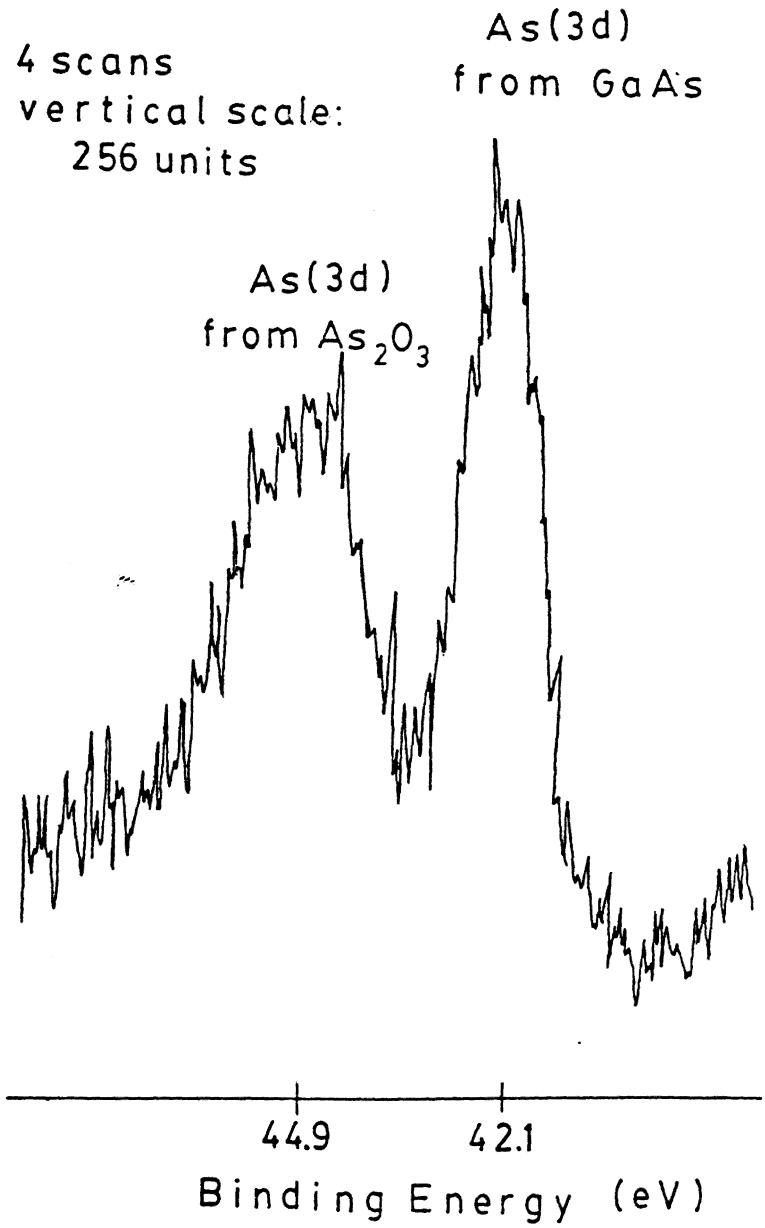

Figure 28
ESCA of oxidized GaAs crystal - As(3d)

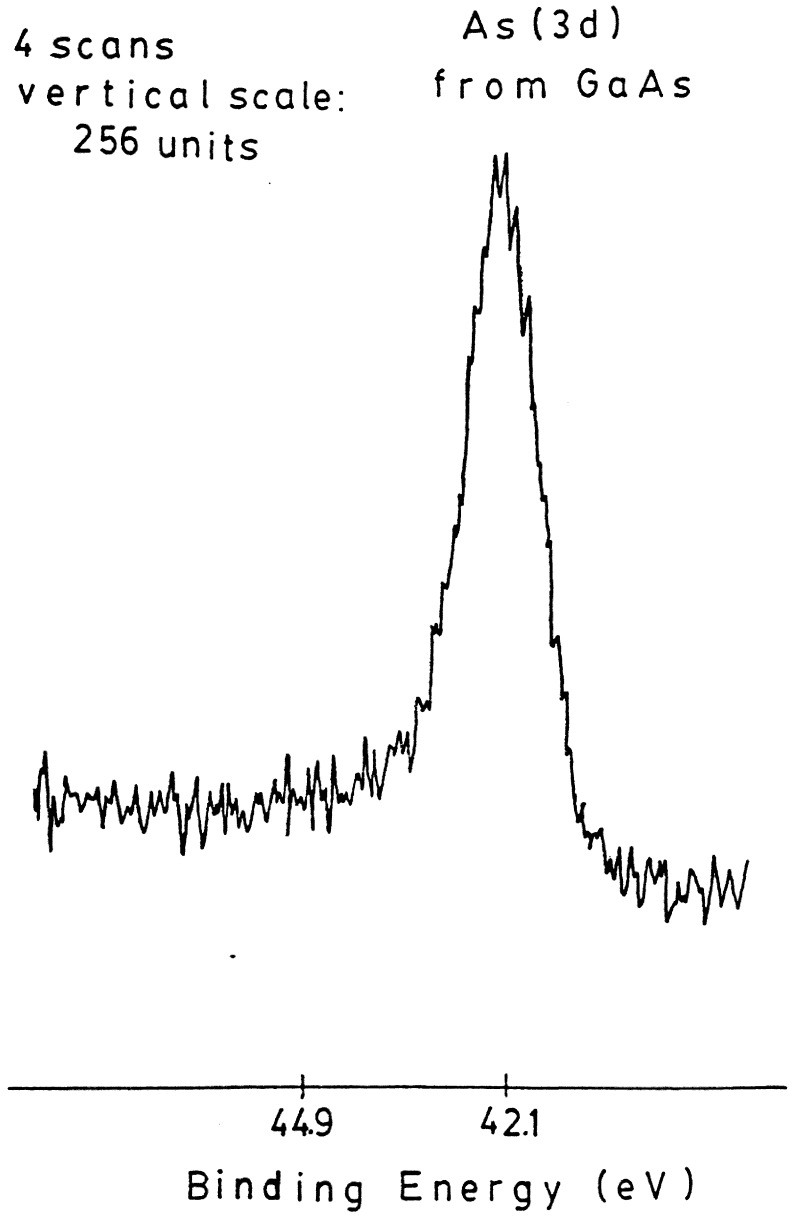

Figure 29
ESCA of cleaned GaAs crystal - As(3d)

which yielded Mott-Schottky plots, and the photocurrent onset potential method. The basic AC voltammetric set-up to obtain Mott-Schottky plots is represented by Figure 23. When a small AC voltage was applied to the cell, the resulting AC current was analyzed. Utilizing its amplitude and phase angle, the impedance of the n-GaAs semiconductor/electrolyte interface was determined. (74) Table 2 contains some typical data obtained as a result of AC voltammetry. The data were analyzed by assuming a linear RC circuit, where R is the cell resistance and C is the space charge capacitance. By plotting the inverse of the capacitance squared versus applied potential, a Mott-Schottky plot was obtained. (See Figure 30.) Mott-Schottky plots should yield a straight line whose potential axis intercept is V_{fb} + .0257 volts. In this fashion, the flatband potential may be determined. Unfortunately, the Mott-Schottky plots obtained resulted in a curve, thus making the V_{fb} determination impossible. This may be due to the frequency dispersion which is often observed for semiconductor/electrolyte interfaces. (74)

Laflere, van Meirhaeghe, and Cardon (76) observed a "knee" region (See Figure 31) at potentials more negative than -0.35 volts. They reported that

Table 2. AC voltammetry data for a clean n-GaAS electrode in 0.01 M HNO_3/0.1 M KNO_3

Applied potential (volts)	i_0 (μA)	i_{90} (μA)	$\frac{i_{90}}{i_0^2+i_{90}^2 E_{ac}}$	$\frac{i_0}{i_0^2+i_{90}^2 E_{ac}}$	R (kΩ)	C (μf)
1.0	.36	.33	4.80	5.24	5.24	.033
0.8	.38	.34	4.54	5.07	5.07	.034
0.6	.40	.33	4.26	5.16	5.16	.037
0.4	.41	.32	4.11	5.26	5.26	.039
0.2	.41	.28	3.94	5.77	5.77	.040
0.0	.32	.17	4.49	8.46	8.46	.035

f = 1.0 kHz
E_{ac} = 3.47 mV

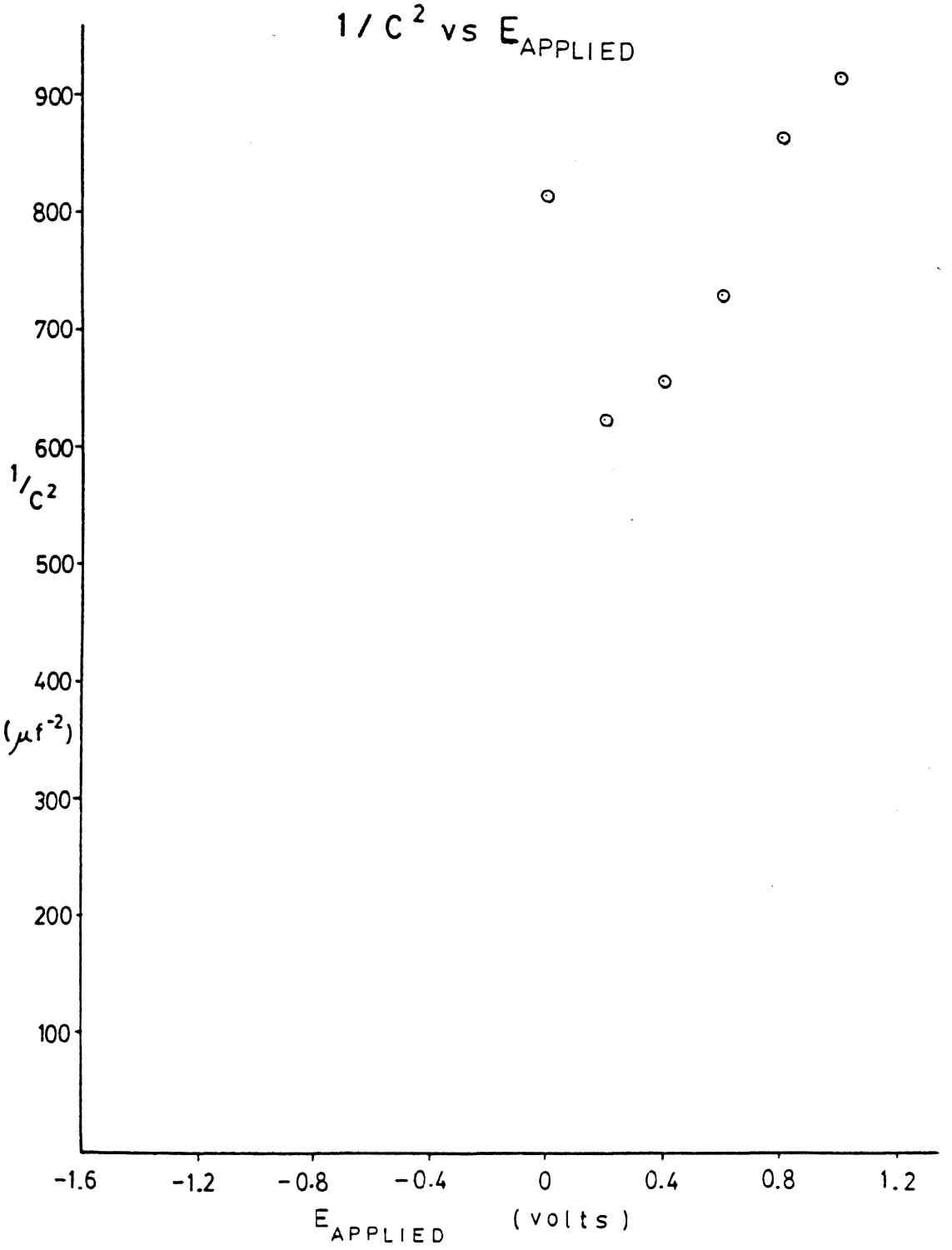

Figure 30
Mott-Schottky plot for a clean n-GaAs electrode

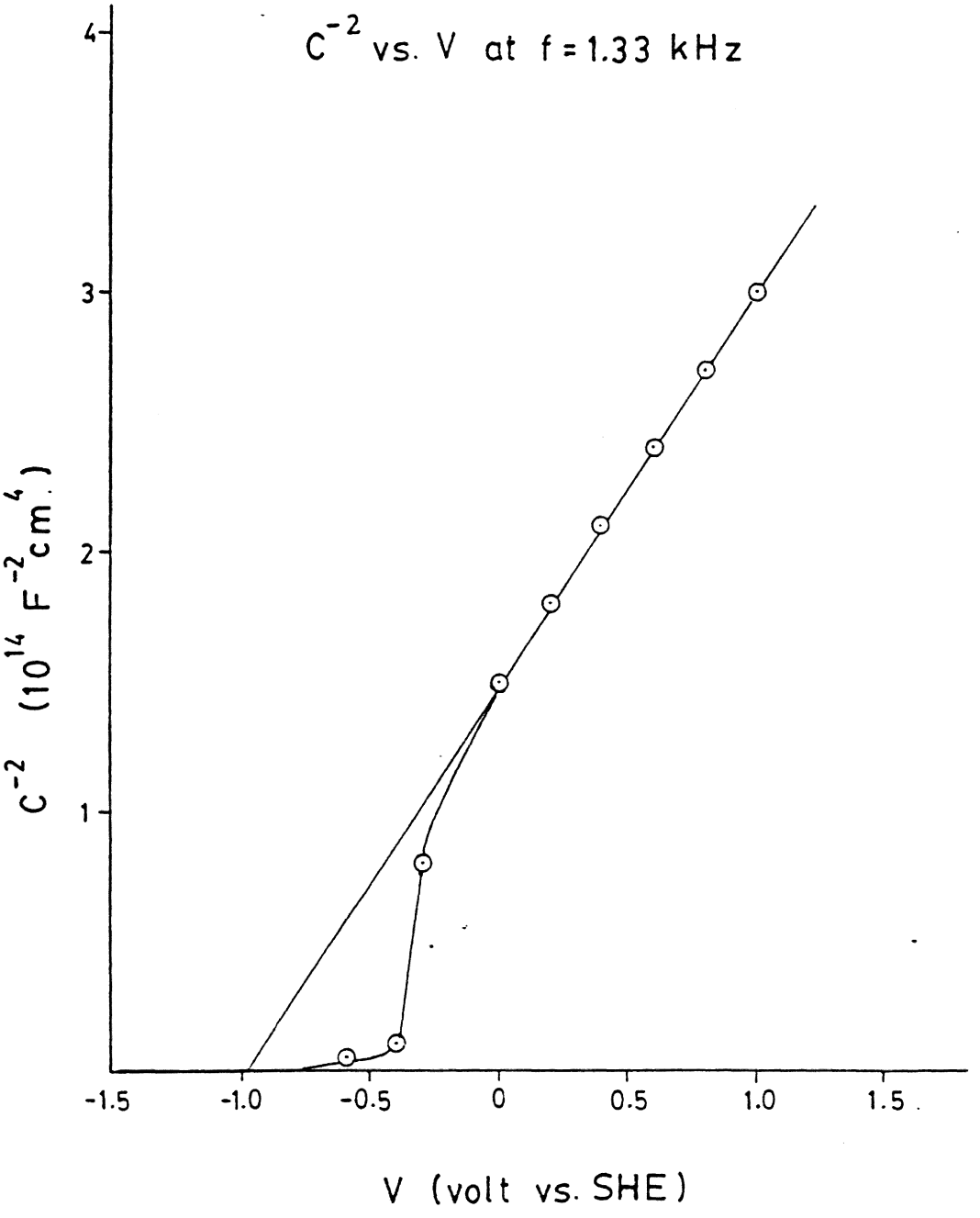

Figure 31

Mott-Schottky plot by Laflere

stabilization times of greater than 15 minutes were required before each impedance measurement. Without this knee region, their V_{fb} determination was reported as -1.0 volts vs. SHE or -1.24 volts vs. SCE. The knee region, as they reported it does not appear when the n-GaAs is in contact with a metal Schottky barrier. They stated that this phenomenon may be due to the presence of the electrolyte in liquid-junction interfaces.

The second method of flatband determination was photocurrent onset potential. Two approaches were employed. The first technique used a chopped light beam to generate anodic and cathodic currents. Figure 32 presents the recorded data. In this method the anodic current decayed with time when the electrode was illuminated at potentials near V_{fb}. Once the light beam was blocked, a momentary cathodic current was observed. This current is believed to be due to reduction of hole oxidation products. V_{fb} was located at the point where the net anodic and cathodic currents (after the pulse decay) were zero. In 0.5 M H_2SO_4, V_{fb}= -0.7 volts ± 50 mV. In the second photocurrent onset potential technique the plateau photocurrent was first measured. Next, the dark current was subtracted from the photocurrent. The

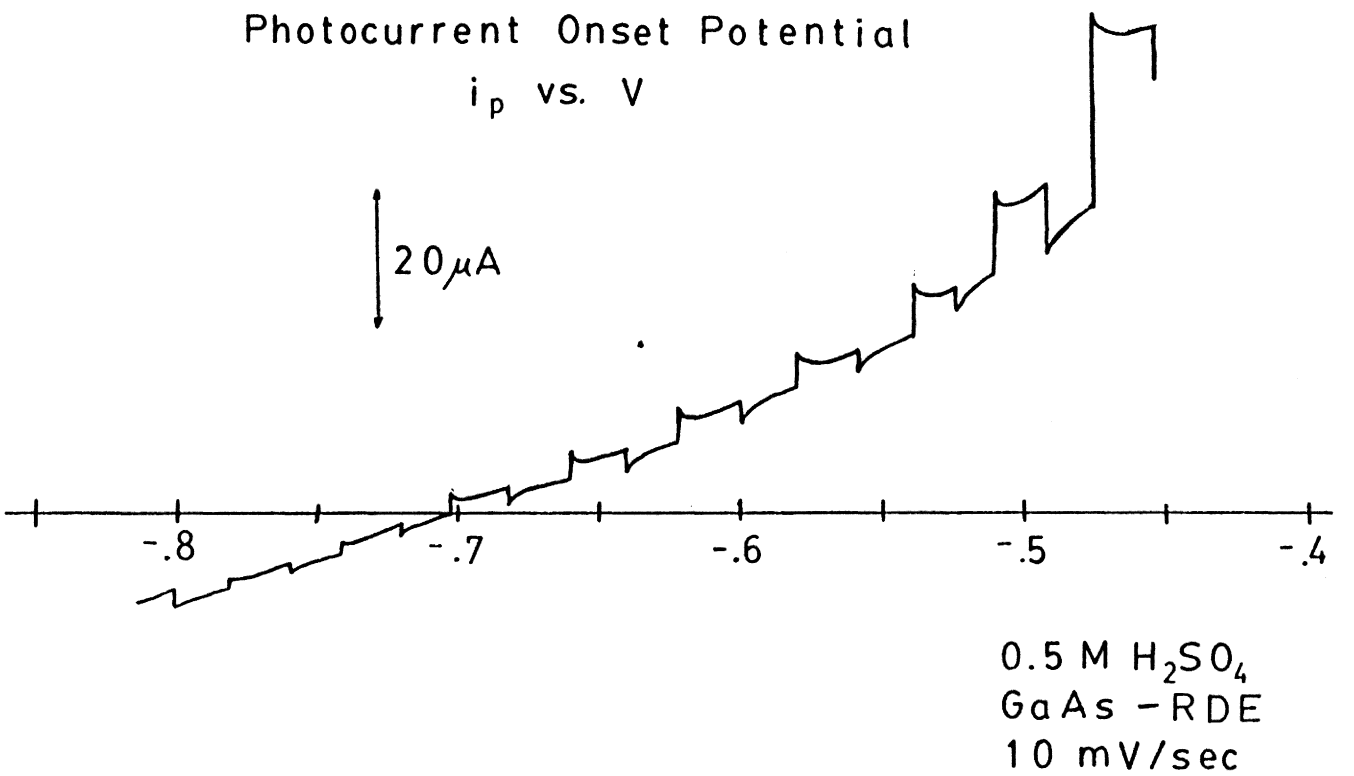
Photocurrent Onset Potential
i_p vs. V
20μA
-.8
-.7
-.6
-.5
-.4
0.5 M H_2SO_4
GaAs - RDE
10 mV/sec

Figure 32

photocurrent squared (Table 3) was plotted versus the potential and the flatband potential determined by the potential axis intercept (-0.70 volts vs. SCE in 1.0 M H_2SO_4) (See Figure 33.)

Table 3

Flatband potential as Determined By Photocurrent Onset Potential in pH 1.0 H_2SO_4

V (volts)	i_p (μA)	i_p^2 (μA^2)
-.70	2	4
-.65	8	64
-.60	10	100
-.55	13	169
-.50	16	256

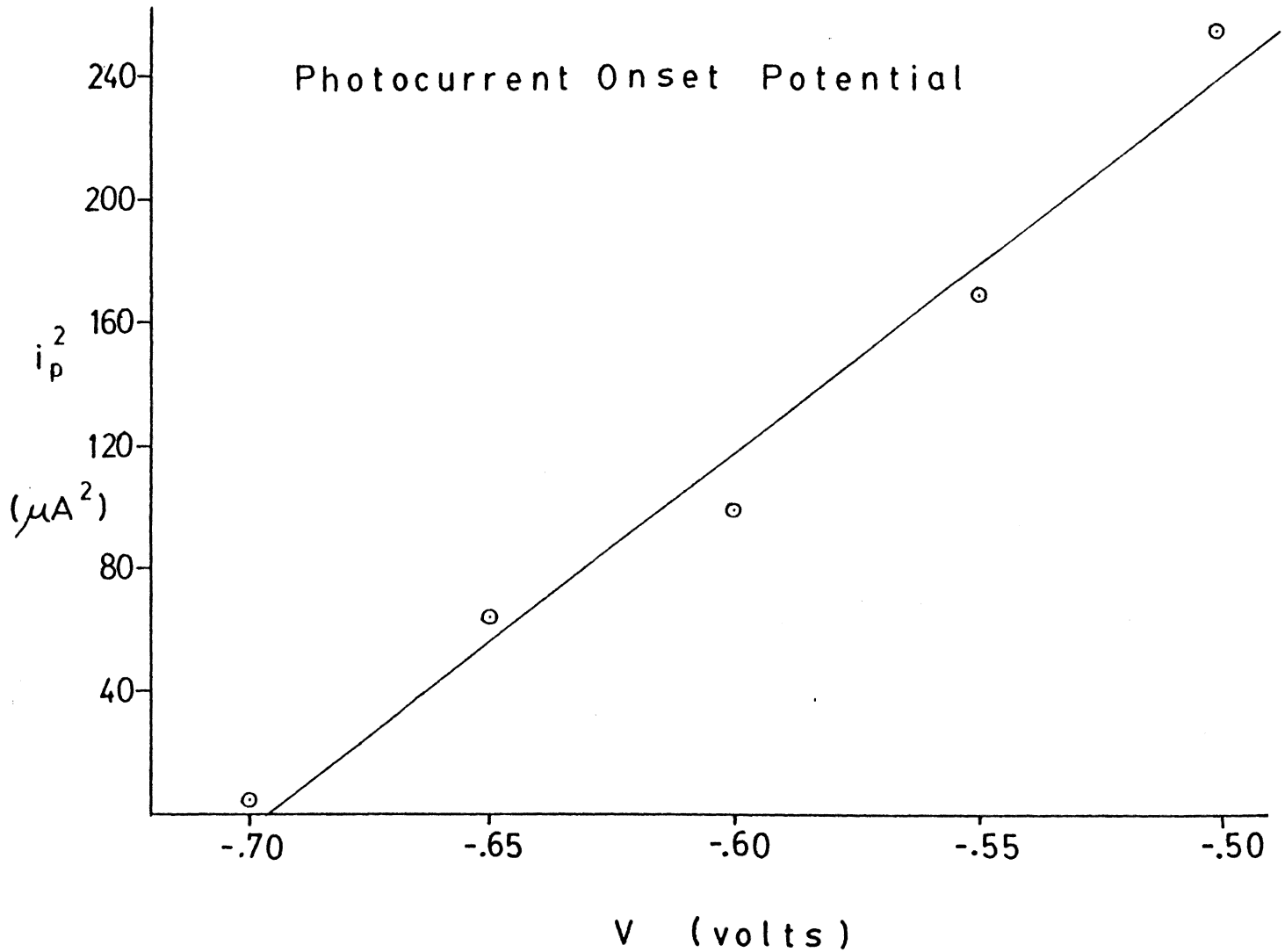
Photocurrent Onset Potential
240
200
160
120
80
40
i_p^2
(μA^2)
-.70
-.65
-.60
-.55
-.50
V (volts)

Figure 33

B. Analysis of uncoated n-GaAs photoelectrode

Before the corrosion rate of the n-GaAs photoelectrode could be measured, differential pulse polarography (DPP) was used to analyze the possible soluble corrosion products, As(III) and Ga(III). These corrosion products are soluble in acid, insoluble at neutral pH, and soluble at high pH. Initial experiments included sampled DC polarography in both acidic and basic media. First analyzed was Ga(III). Although predicted to be observable (20), Ga(III) could not be seen even after increasing its concentration to approximately 12 μM with current sensitivity at 0.5 μA full scale. These experiments were carried out in pH 12.0 NaOH, pH 1.0 HNO_3, and pH 3.0 HCl.

The electrochemistry of As(III) was observed in acidic media. Referring to Figure 22, the first peak at -0.6 volts corresponds to a $3e^-$ reduction of As(III) to As(0). (58) (77) Calibration curves of current versus concentration were obtained at -0.6 volts. As can be seen in Figure 34, a nice linear calibration curve was obtained in acidic media over a wide concentration range. (See Table 4.) Figure 35 illustrates that at the same pH for strong acids the As(III) peak potential does not change, thus allowing

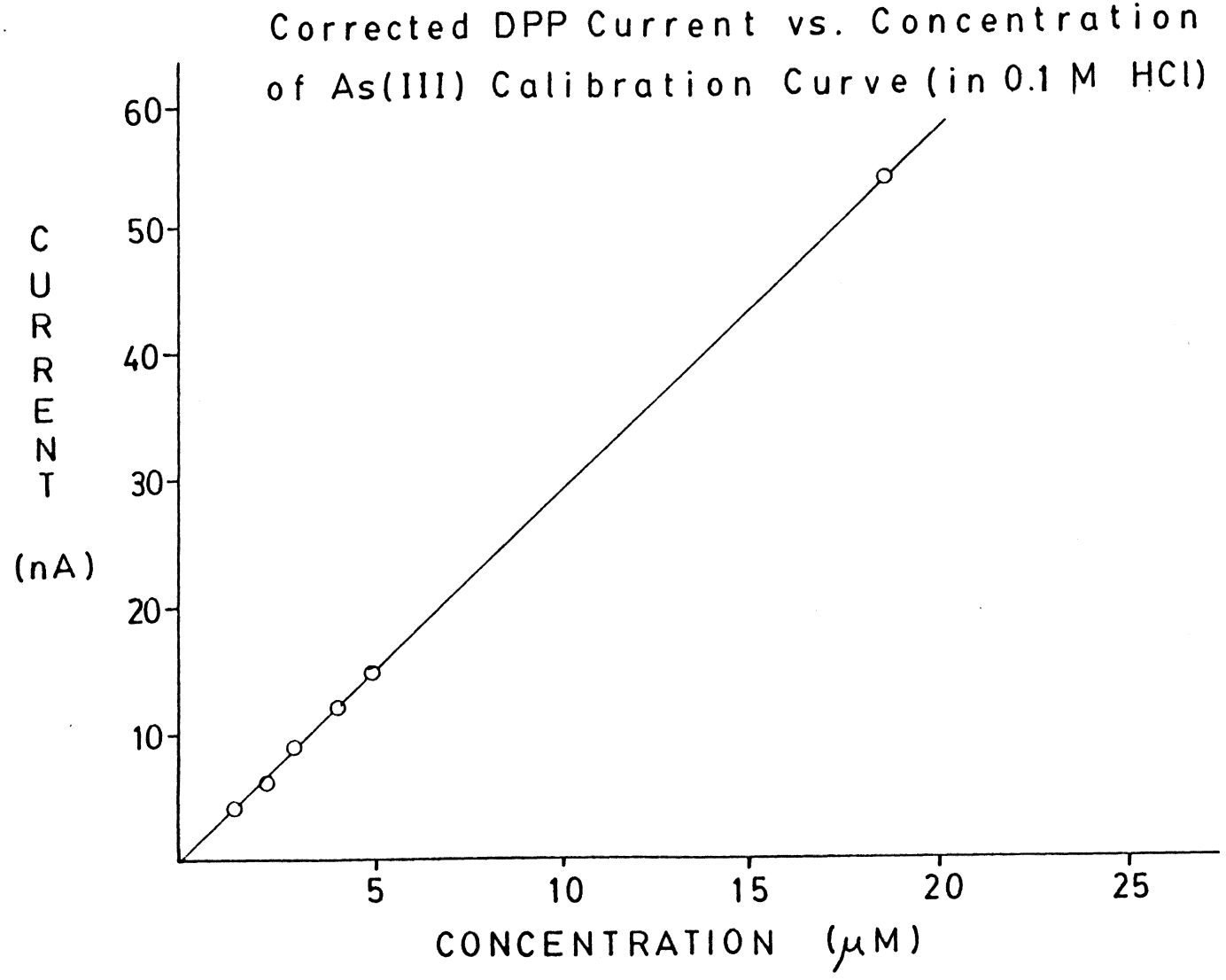
Corrected DPP Current vs. Concentration
of As(III) Calibration Curve (in 0.1 M HCl)
CURRENT (nA)
60
50
40
30
20
10
5
10
15
20
25
CONCENTRATION (μM)

Figure 34

Table 4. Solutions used to check linearity of current vs. As(III) concentrations

Electrolyte	(volts) Potential	(μM) Concentration Range
HCl - 0.1 M	-.60	1.3 - 201
pH 3.0	-.75	3.3 - 76
pH 3.0/0.1 M NaCl	-.75	3.3 - 76
pH 5.0	-.975	3.3 - 50.7
HNO_3 - 0.1 M	-.60	1.3 - 185
pH 3.0	-.72	3.3 - 60
pH 3.0/0.1 M KNO_3	-.72	3.3 - 71
pH 5.0	-.84	3.3 - 493
H_2SO_4 - 0.1 M	-.60	1.3 - 201
pH 3.0	-.78	2.0 - 168
pH 3.0/0.1 M Na_2SO_4	-.78	2.0 - 168
pH 5.0	-.975	12.7 - 243
PO_4^{-3} buffers - pH 3.0	-.98	6.5 - 507
pH 4.7	-1.15	5.2 - 507
pH 7.0	-1.30	5.2 - 507
NaCl - 0.3 M	-.60	6.5 - 50.7
HAc - pH 5.0/0.01 M NaAc/ 0.1 M NaCl	-1.15	6.5 - 279
pH 5.0/0.01 M NaAc/ 0.1 M KNO_3	-1.15	6.5 - 279
pH 5.0/0.01 M NaAc/ 0.1 M Na_2SO_4	-1.15	6.5 - 279

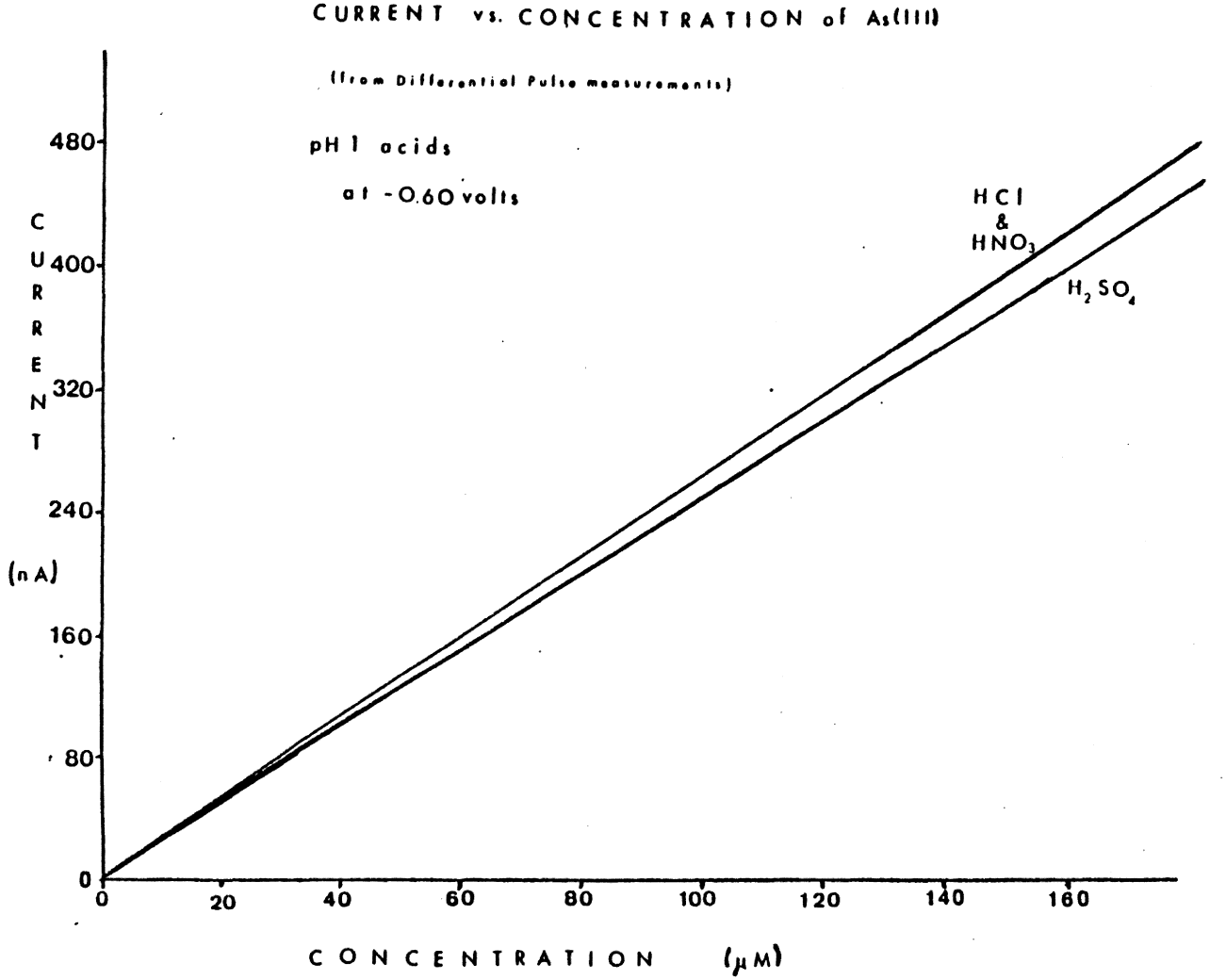
CURRENT vs. CONCENTRATION of As(III)
(from Differential Pulse measurements)
pH 1 acids
at -0.60 volts
HCl
&
HNO3
H2SO4
CURRENT (nA)
480
400
320
240
160
80
0
0
20
40
60
80
100
120
140
160
CONCENTRATION (μM)

Figure 35

consistent data to be obtained at the same pH. If the pH is increased, the peak potential should shift negatively according to the Nernst equation for the simplified reduction reaction

$$HAsO_2 + 3H^+ + 3e^- \rightarrow As + 2H_2O$$

This behavior was observed for HNO_3 for pH 1, 2, and 3. But as the pH increased further it became apparent that the polarographic maxima peak (Figure 22) shifted toward the peak used for analysis. By pH 3, the As(III) reduction peak could still be used to generate calibration plots but with some reservations as to their accuracy. At pH 4 the As(III) reduction peak was completely obscured, but at pH 5 the As(III) reduction peak (believed to be the same peak) reappeared on the other side of the polarographic maxima peak.

Prior to photoelectrochemical etching, both open-circuit etching rates and electrochemical etching rates in the dark were measured in several acidic media: H_2SO_4, HCl, and HNO_3, all at pH 1.0. For both the electrochemical and photoelectrochemical etching experiments the potential of the n-GaAs electrode was held at + 0.500 volts versus SCE, a potential which is sufficiently positive of the flatband potential for maximum photocurrent generation. By etching at constant potential, one can obtain a corrosion ratio of moles e^-

passed per mole As(III) generated. One can integrate the current to measure total charge passed, measure the concentration of As(III) generated, and use spiking to obtain a calibration plot for As(III). Table 5 contains some typical data. Results from the open-circuit and dark etching experiments proved that etching rates under these conditions were negligible. (See Table 6.) Note that after 30 minutes that only 1 μmole of As(III) appears, whereas during a single 5 minute photoelectrochemical etch, approximately 100 μmoles of As(III) appear. Thus, attention was given to photoelectrochemical etching.

Figure 36 illustrates a photocurrent-time plot. The stable photocurrents indicate that no passive layer is forming. Table 7 contains the results of photoelectrochemical etching for the uncoated n-GaAs photoelectrode in various electrolytes. In theory the number of electrons passed per As(III) generated should be six according to the reaction (30) (39) (78):

$$GaAs \rightarrow Ga(III) + As(III) + 6e^-.$$

Other workers have obtained this corrosion ratio. Results obtained by Kohl, Wolowodiuk, and Ostermayer

Table 5. Calculation of results from photoelectrochemical etch and DPP from pH 1.0 HNO_3/ 0.1 M KNO_3 at -0.60 volts clean GaAs

t(min)	i(nA)	i_{corr}(nA)	c(μM)	Δc'(μM)	μmoles As(III)	Q(Coul)	μmoles e-	$\frac{\text{moles e-}}{\text{mole As(III)}}$
0	16.4	0	0	0	0	0	0	0
5	300	283.6	194.6	194.6	5.838	2.1158	21.93	3.76
10	555	538.6	350.2	155.6	4.668	1.4936	15.48	3.32
15	753	736.6	452.9	102.7	3.081	1.4342	14.86	4.82
20	887	870.6	522.4	69.5	2.085	0.9459	9.80	4.70
25	1027	1010.6	595.0	72.6	2.178	1.4273	14.79	6.79
30	1238	1221.6	704.5	109.5	3.285	1.4182	14.70	4.47
								4.64±.79

After spiking with 2.00 μM As (III)

Δc(μM)	i(nA)	i_{corr}(nA)	i'(nA)
133.33	1360	1343.6	122
231.58	1545	1528.6	307
320.00	1720	1703.6	482

Intercept and slope determined by linear regression

$i_{corr} = i - i_{bkg}$

$i' = i_{corr} - i_{corr(30)}$

$\mu\text{moles e-} = \frac{Q \times 10^6 \ \mu\text{moles/mole}}{F}$

Table 6. Electrochemical etching of n-GaAs electrode in the dark

Electrolyte	Ave μmoles As(III)/etch	Ave μmoles e-/etch	Ave Q(Coul)/etch	Ave $\frac{\text{moles e-}}{\text{moles As(III)}}$
1 HCl pH 1.0	.0299			
2 H_2SO_4 pH 1.0	1.011	.0282	.00272	.0279±.0043
3 HNO_3 pH 1.0 /0.1 M KNO_3	1.482	.0461	.00445	.0311±.0059
4 pH 2.0/0.1 M KNO_3	.992	.0277	.00267	.0279±.0071
5 pH 3.0/0.1 M KNO_3	.891	.0221	.00213	.0248±.0065

(etching time = 30 minutes)

1 - open circuit

2 - 5 potentiostatted at +0.5 volts vs. SCE

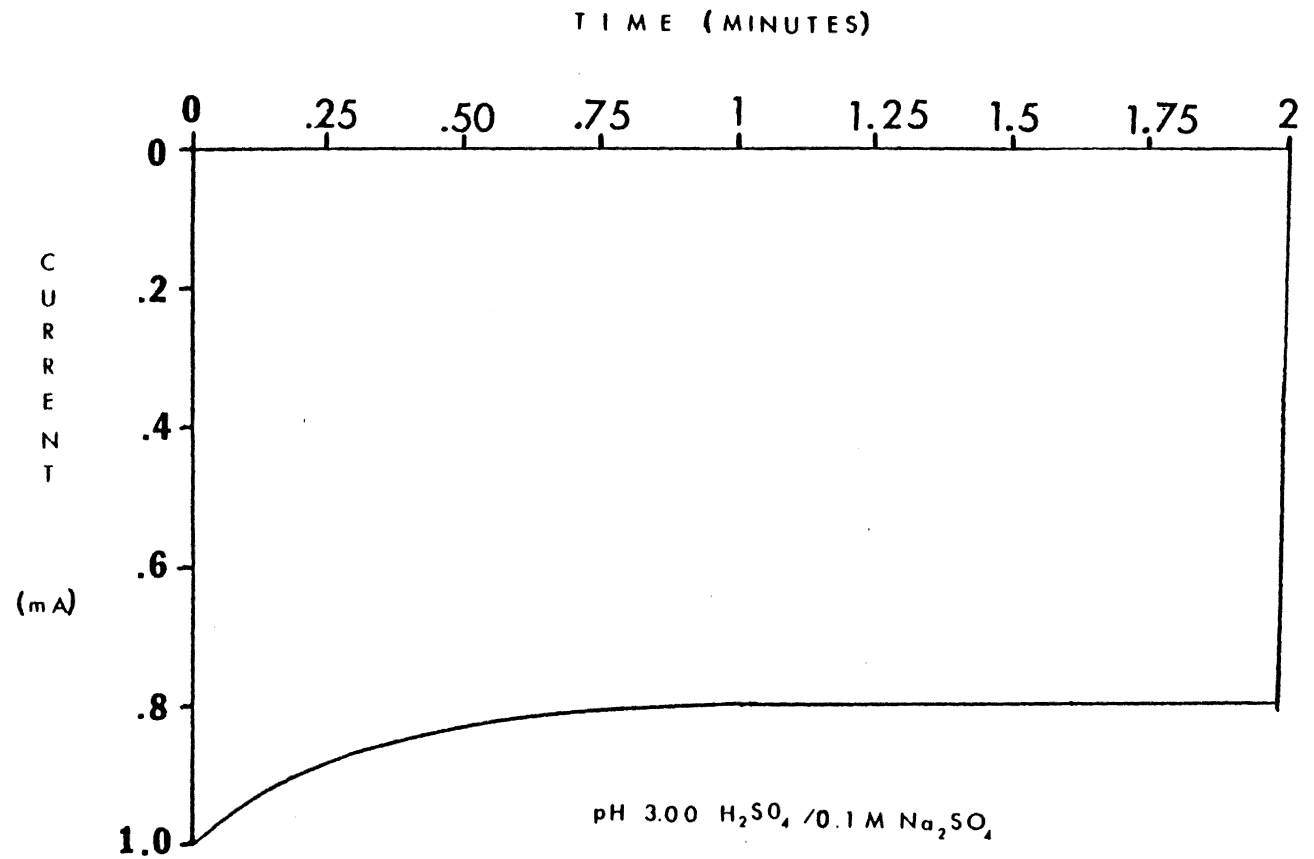

Photocurrent-time plot

Figure 36

(31) were actually higher than the theoretical value. They photo-oxidized the n-GaAs photoelectrode in several acidic solutions: H_2SO_4, HCl, HF and HBr, all of which were 2 M. Their data show 7.2 photons per GaAs in H_2SO_4 and HCl. The photon-based results may be in error due to recombination losses.

As can be seen in Table 7, the average number of moles of electrons per mole of As(III) is mostly between 2 to 3. These values are in disagreement with the theoretical value of 6.

Weight loss experiments, as described in chapter one, were attempted. As can be seen in Table 8, the results from weight loss yielded 2.6 electrons per GaAs whereas DPP results yielded 3.7 electrons per molecule. Similar results were obtained in H_2SO_4 and HCl. In these cases the DPP results were higher than those of the weight loss.

From the HNO_3 /0.1 M KNO_3 results (Table 7), it appeared that by increasing the conductivity (or the ionic strength) the average mole ratio of electrons to As(III) increased also. But as the pH increased, this ratio declined slightly. This phenomenon was noted by Gerischer (21) in his work involving CdS SLJSC. He explained that this effect was due primarily to the shift of the Fermi level towards a more positive

Table 7. Photoelectrochemical etching results for uncoated n-GaAs photoelectrode

Electrolyte	Ave $\frac{\text{moles e-}}{\text{mole As(III)}}$	Ave Q(Coul)/etch
H_2SO_4 pH 1.0	2.25±.16	1.110
	2.07±.06	1.201
	2.36±.09	0.900
HCl pH 1.0	2.38±.15	0.751
HNO_3 pH 1.0	2.57±.06	0.476
HNO_3 pH 1.0/0.1 M KNO_3	4.64±.79	1.470
pH 2.0/0.1 M KNO_3	4.39±.31	0.179
pH 3.0/0.1 M KNO_3	4.03±.53	0.103
	2.95±.31	0.128
H_2SO_4 pH 3.0/0.1 M Na_2SO_4	3.86±.42	0.106
	3.17±.39	0.120
HCl pH 3.0/0.1 M NaCl	3.01±.85	0.119
(etching time = 30 minutes)		

Table 8. Results of typical weight loss experiments in HNO_3 pH 1.0/0.1 M KNO_3

t_{etch}(min)	m_{ave}(g)	moles e- / *mole As(III)
0	9.5392	0
10	9.5380	3.433
20	9.5366	3.311
30	9.5358	3.803
40	9.5350	3.303
50	9.5342	4.595
		3.69±.41

Q_{total} = 8.7216 C

μmoles e^-_{total} = 90.39

Δm = 5.0 mg

μmoles GaAs = 34.5 $\quad \frac{90.39}{34.5} = 2.62$

	Q Total	Δm(mg)	moles e- / mole As(III)	moles e- / *mole As(III)
H_2SO_4 pH 1.0 /0.1 M Na_2SO_4	7.2171	5.1	2.12	2.97
HCl pH 1.0 /0.1 M NaCl	7.6126	4.7	2.43	3.13

*as determined by DPP

potential at higher pH. Thus, both effects, conductivity and pH, were reflected in the pH 3.0 H_2SO_4 and HCl with supporting electrolyte added. It is apparent that the level of conductivity has a greater effect on the electron-to-As(III) ratio than the pH. No studies were conducted by altering the amount of supporting electrolyte.

C. Analysis of Coated n-GaAs Photoelectrode

Three different coatings were applied to clean n-GaAs electrode surfaces in an attempt to suppress corrosion of the photoelectrode. These coatings were polymers of tetrachlorosilane, divinylbenzene (DVB), and phenol. The coatings were applied via vapor deposition or by voltammetric oxidation.

In the silanization procedure the clean gallium arsenide surface was exposed to the tetrachlorosilane under a constant vapor pressure. (See Figure 37.) The heated (150°C) sample was allowed to react and form covalent bonds to the silane via the ubiquitous surface oxide, after which cross-linking was accomplished by introduction of water and heat. Results of photoelectrochemical etching revealed that the corrosion rate of n-GaAs was not significantly improved in acidic media.

The next approach taken was photoelectrochemical oxidation of divinylbenzene or phenol in either acetonitrile or methanol electrolytes. This approach is based on the relatively recent idea of coating electrodes by electrochemical polymerization. Shaw et al. (79) coated electrodes by benzophenone reduction (to its radical anion) in a styrene mixture to produce a polystyrene film. Thus, research in this area

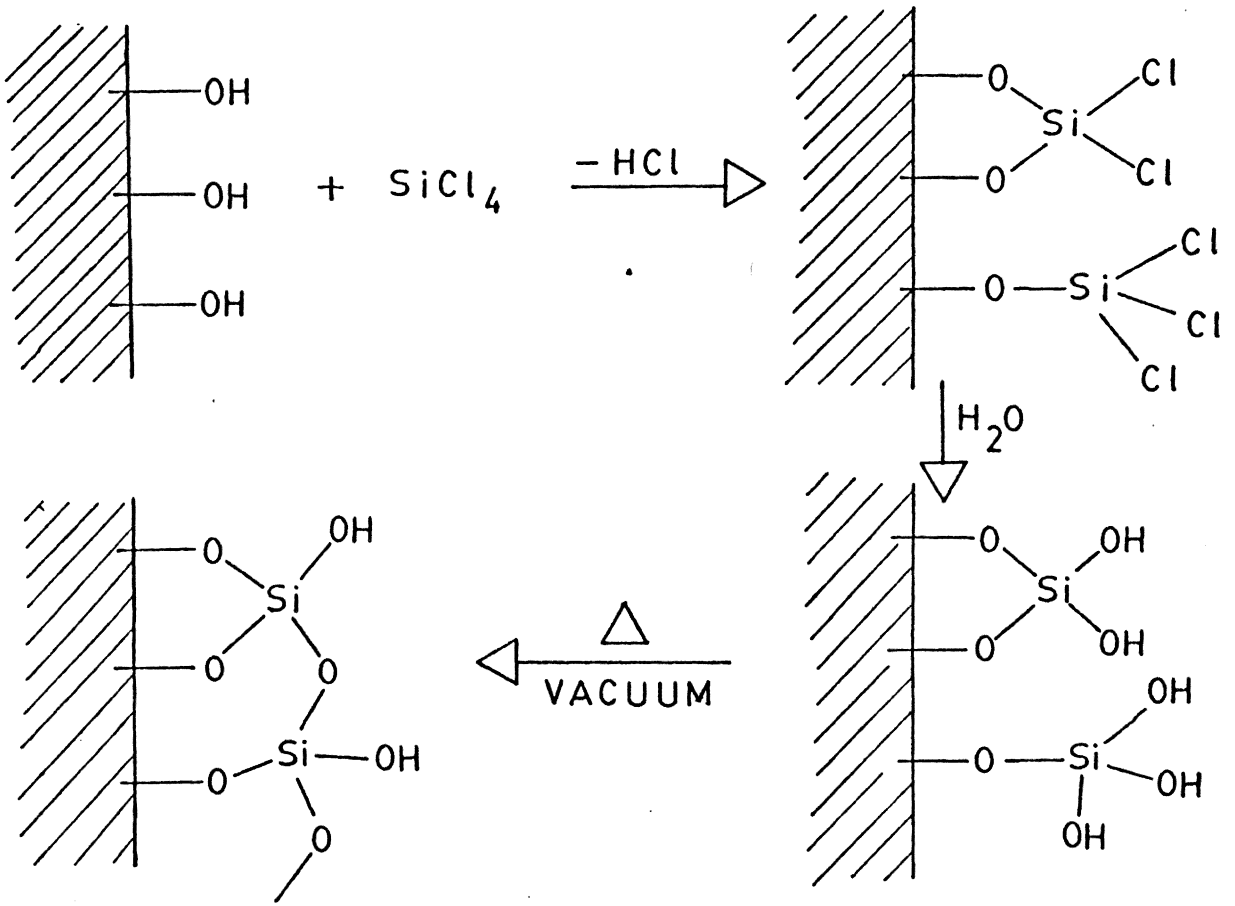

Silanization of GaAs Surface

Figure 37

prompted the idea that divinylbenzene (DVB) should be electrochemically active and capable of self-initiation.

Figure 38 illustrates DVB oxidation on a platinum electrode in 0.1 M KPF_6 in CH_3CN. The oxidation peak is observed at +1.40 volts vs. SCE. A very weak reduction peak is observed at +.33 volts vs. SCE. It was suggested by R. S. Vithanage (11) that this small reduction wave was due to dimeric or oligomeric species generated during the voltammetric polymerization process. On subsequent scans there was drastic and rapid attenuation of the oxidation peak. Similar behavior was observed for the GaAs electrode (See Figure 39) as the DVB photooxidation product passivated the electrode surface. Photocorrosion results will be analyzed at the end of this section.

Use of phenols as another corrosion inhibitor was first explored by Bruno, Pham, and Dubois. (64) In their study the anodic oxidation of disubstituted phenols in an alcohol and hydroxide media was investigated. The base ensured maximum phenolate ion concentration which is more easily oxidized than phenol. They concluded that the formation of the polyphenylene oxide film is continuous on and adheres to noble metals, such as Pt and Au, and suppresses

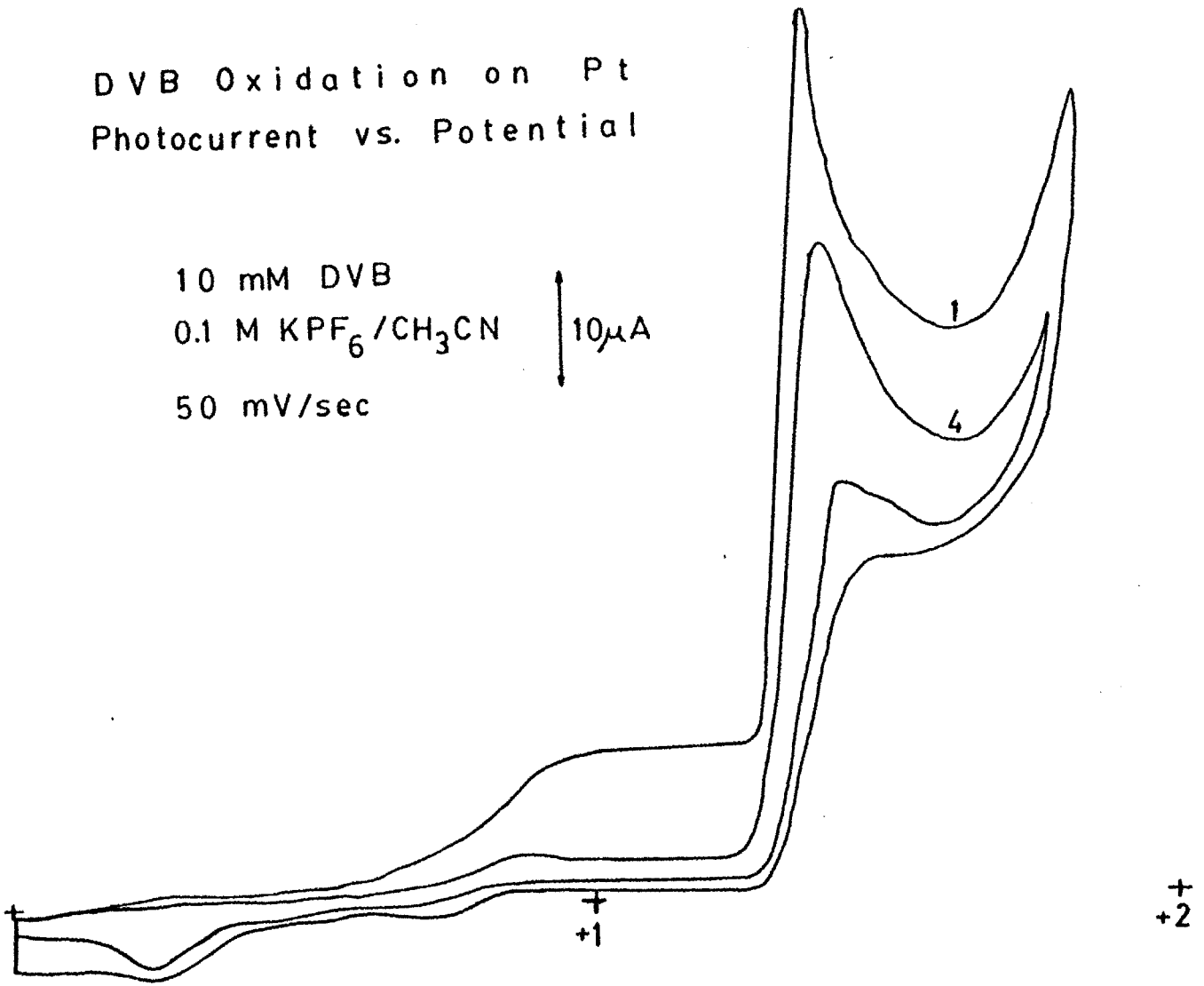
DVB Oxidation on Pt
Photocurrent vs. Potential
10 mM DVB
0.1 M KPF_6/CH_3CN
50 mV/sec
10μA
1
4
+1
+2

Figure 38

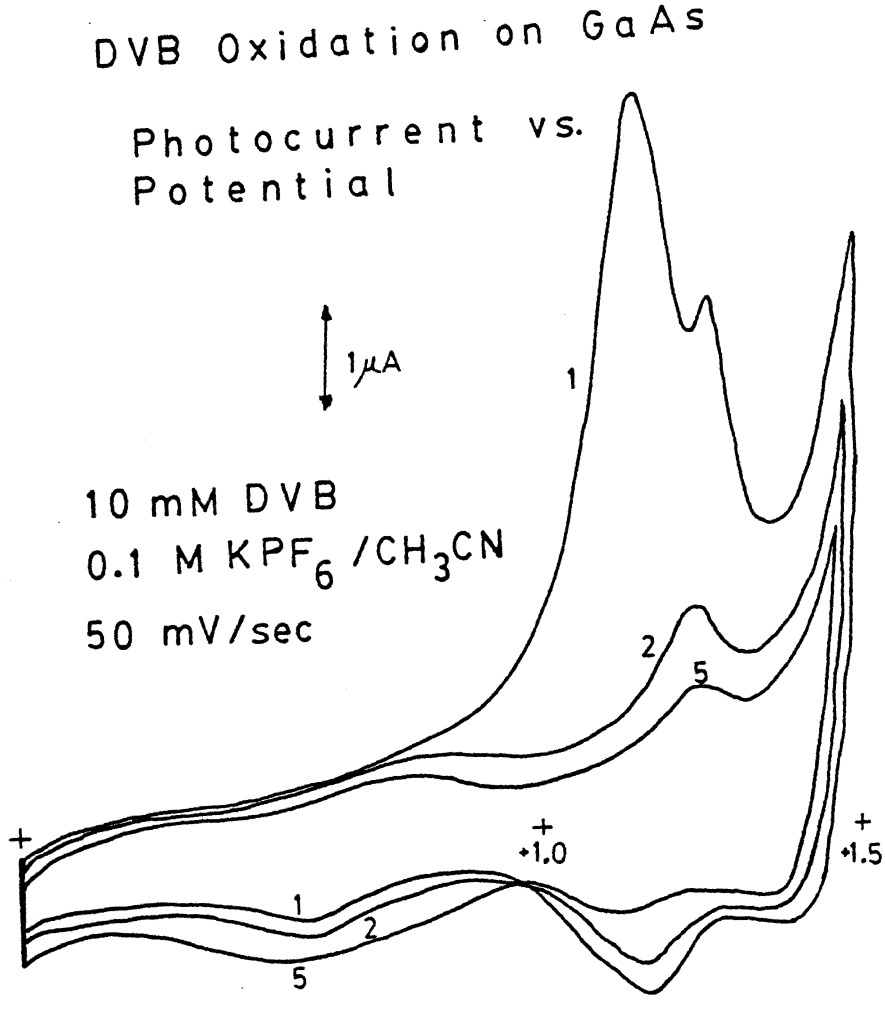
DVB Oxidation on GaAs
Photocurrent vs.
Potential
1μA
10 mM DVB
0.1 M KPF6 /CH3CN
50 mV/sec
1
2
5
+
+1.0
+1.5
1
2
5

Figure 39

corrosion on metals such as Fe, Ni, and Cu, by blocking the electrode surface for water oxidation.

With this in mind phenol was used to produce a polymer coating on Pt, Au, and n-GaAs electrodes. With phenol present in the acetonitrile-sodium hydroxide solvent system, the platinum working electrode attained a saturation current, as shown in Figure 40, for the oxidation of phenol. Upon reversing the scan, the current dropped to near zero (~1μA). Upon obtaining a second scan, the current gradually rose. After +1.2 volts vs. SCE, the current increased more rapidly. This effect may be attributed to the polyphenylene oxide which may be blocking the available sites for further polymerization at lower potentials. Similar behavior was observed on Au electrodes. Figure 25 illustrates the passivation of a gold electrode by formation of polyphenylene oxide in 0.1 M NaOH/MeOH. With each sweep the current decayed at both the oxidation peak (+.33 volts vs. SCE) and the reduction peak (-.06 volts vs. SCE). This is indicative of the formation of the polyphenylene oxide layer.

Finally, the n-GaAs photoelectrode was utilized for phenol oxidation. Figure 41 illustrates the cyclic voltammetric response for the electrochemical

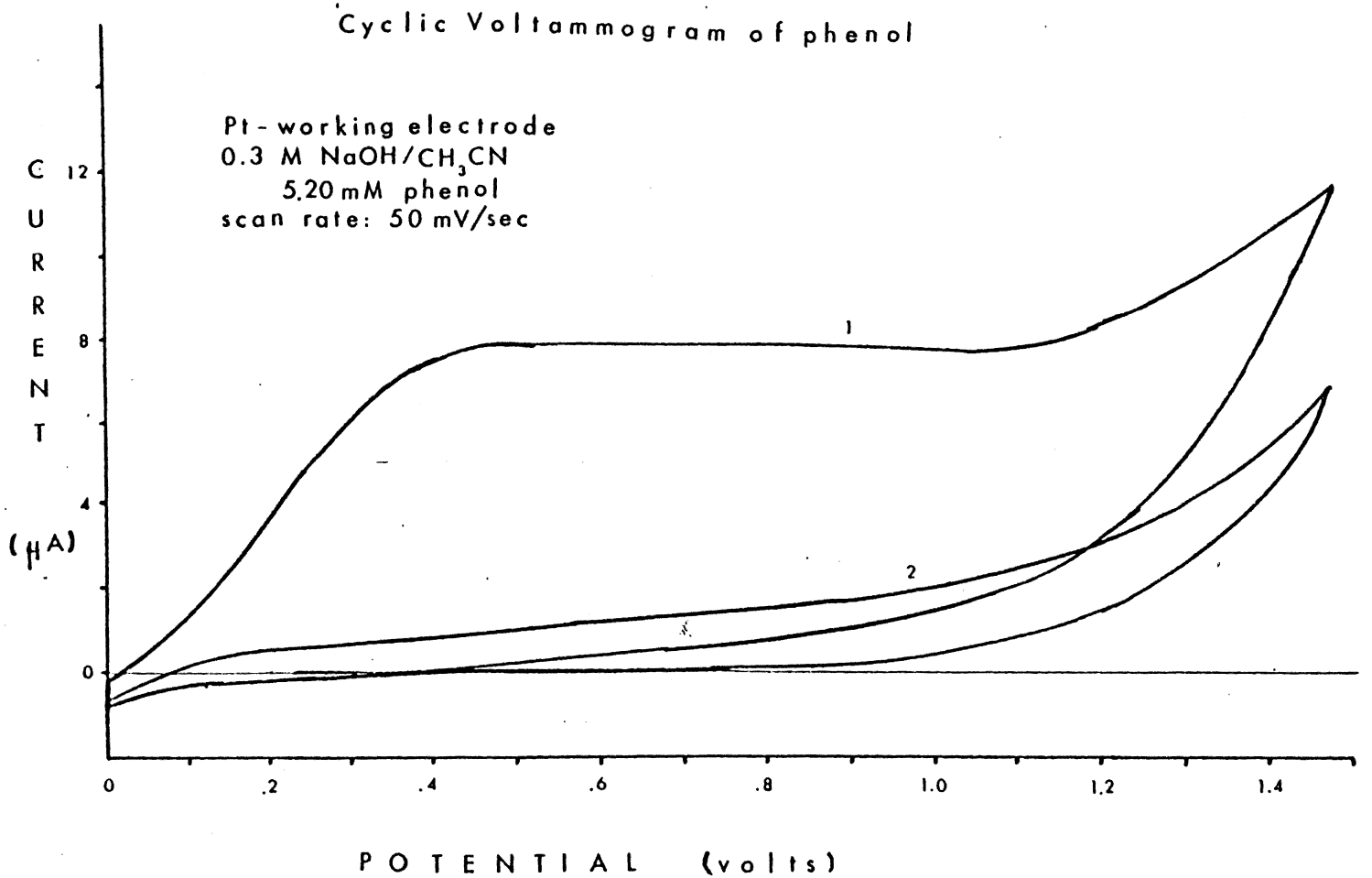
Cyclic Voltammogram of phenol
Pt - working electrode
0.3 M NaOH/CH3CN
5.20 mM phenol
scan rate: 50 mV/sec
CURRENT (μA)
12
8
4
0
1
2
0
.2
.4
.6
.8
1.0
1.2
1.4
POTENTIAL (volts)

Figure 40

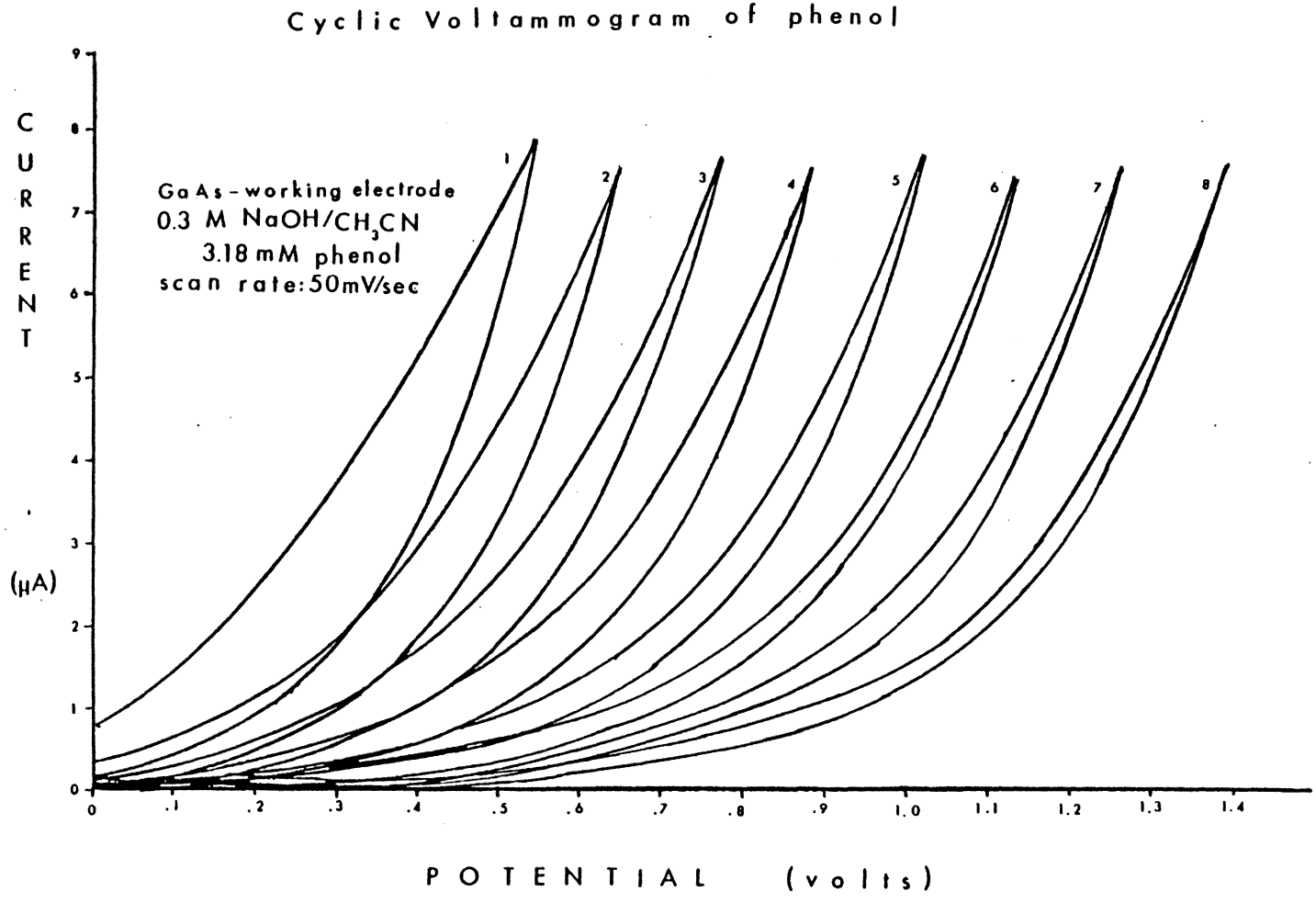
Cyclic Voltammogram of phenol
CURRENT
(μA)
GaAs-working electrode
0.3 M NaOH/CH3CN
3.18 mM phenol
scan rate:50mV/sec
1
2
3
4
5
6
7
8
0
1
2
3
4
5
6
7
8
9
.1
.2
.3
.4
.5
.6
.7
.8
.9
1.0
1.1
1.2
1.3
1.4
POTENTIAL (volts)

Figure 41

formation of a polyphenylene oxide film on the gallium arsenide electrode, which was illuminated with white light. With each scan behavior similar to Pt and Au was observed. The only difference was the lack of a well-defined plateau of current. Solvents were then changed to a $NaOH/CH_3OH$ combination to try to observe well-defined cyclic voltammetry of phenol on n-GaAs. The n-GaAs electrode was illuminated in various concentrations of the phenol mixtures. Figure 42 is a typical cyclic voltammogram obtained by using the n-GaAs photoelectrode. Towards negative potentials no reduction wave was observed, thus indicating that the photooxidation of phenol to polyphenylene oxide is an irreversible electrochemical process. It was also noted that after several cycles, a blue coating was present on the n-GaAs electrode surface. This confirmed the formation of the polymer layer and was in agreement with the observations of Bruno, Pham, and Dubois. (64)

As to how the polymer layer forms, several authors (11) (64) (80-82) have proposed the oxidation mechanism of phenol. (See Figure 43.) First, the phenol, in the alcoholic base, deprotonates to yield the phenolate ion. Electrochemical oxidation yields the neutral radical. Step III shows how the phenolate

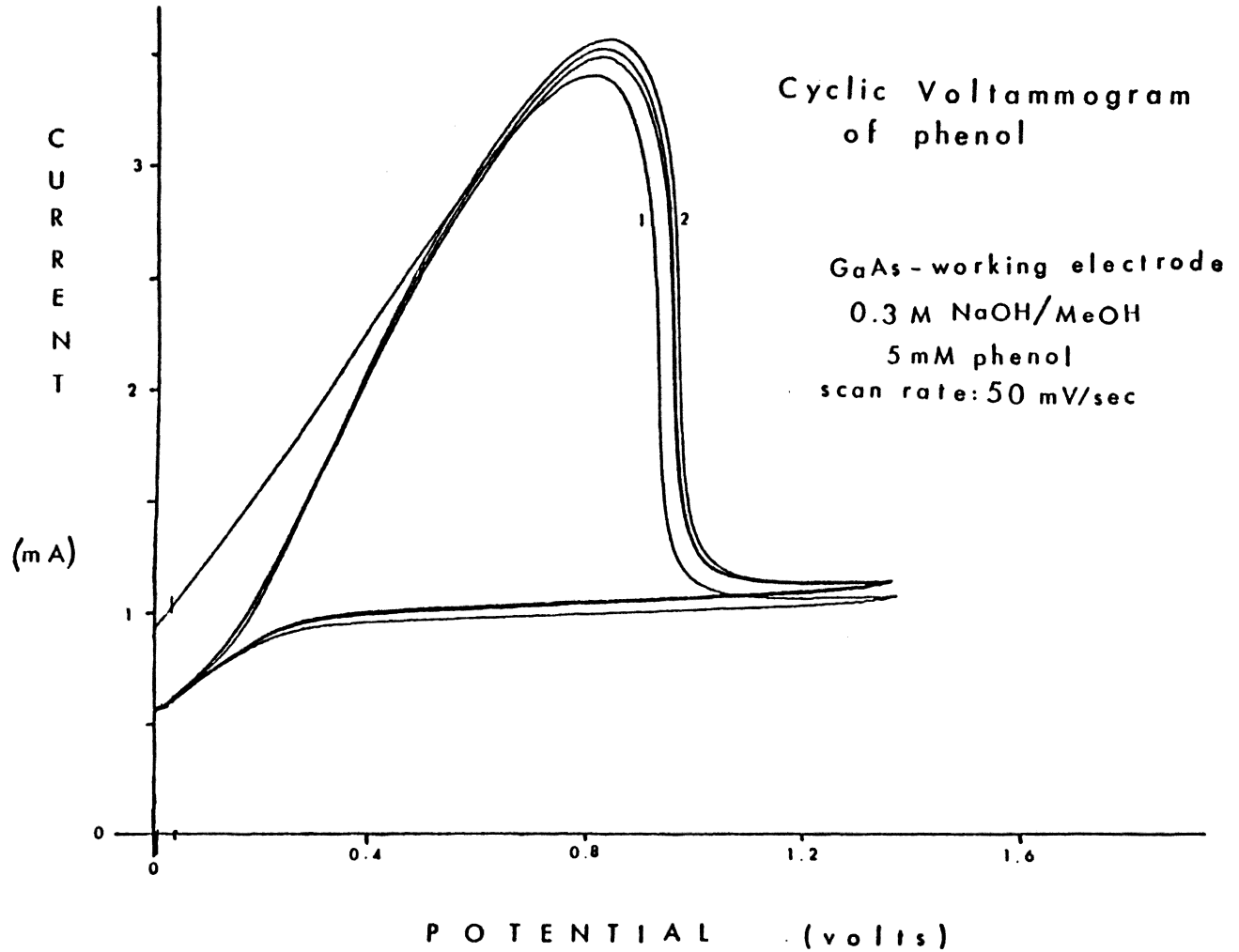
Cyclic Voltammogram
of phenol
GaAs - working electrode
0.3 M NaOH/MeOH
5 mM phenol
scan rate: 50 mV/sec
CURRENT
(mA)
POTENTIAL (volts)
0
1
2
3
0.4
0.8
1.2
1.6

Figure 42

Phenol Mechanism

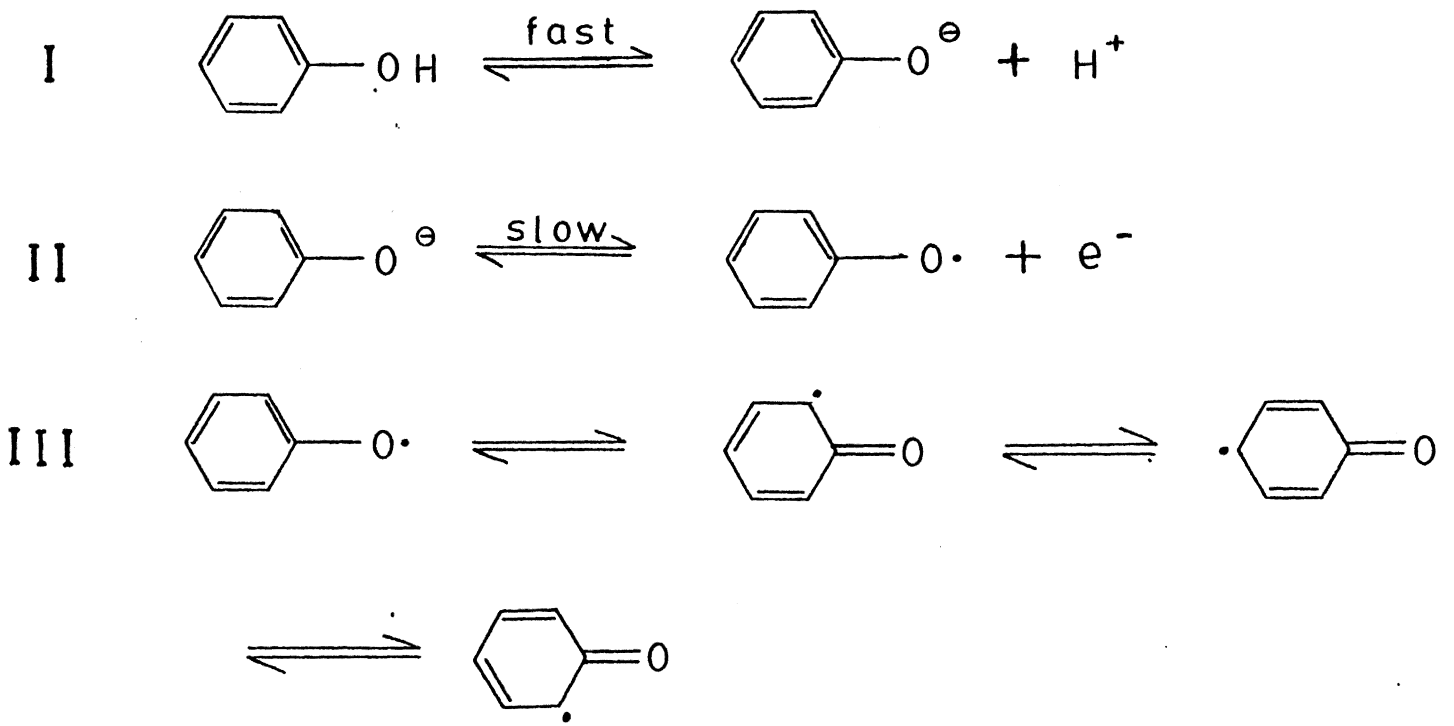

Figure 43

I. Generation of Phenolate in alcoholic base
II. Initiation of Phenolate radical
III. Rearrangement
IV. Propagation 1
V. Propagation 2
VI. Termination 1
VII. Termination 2

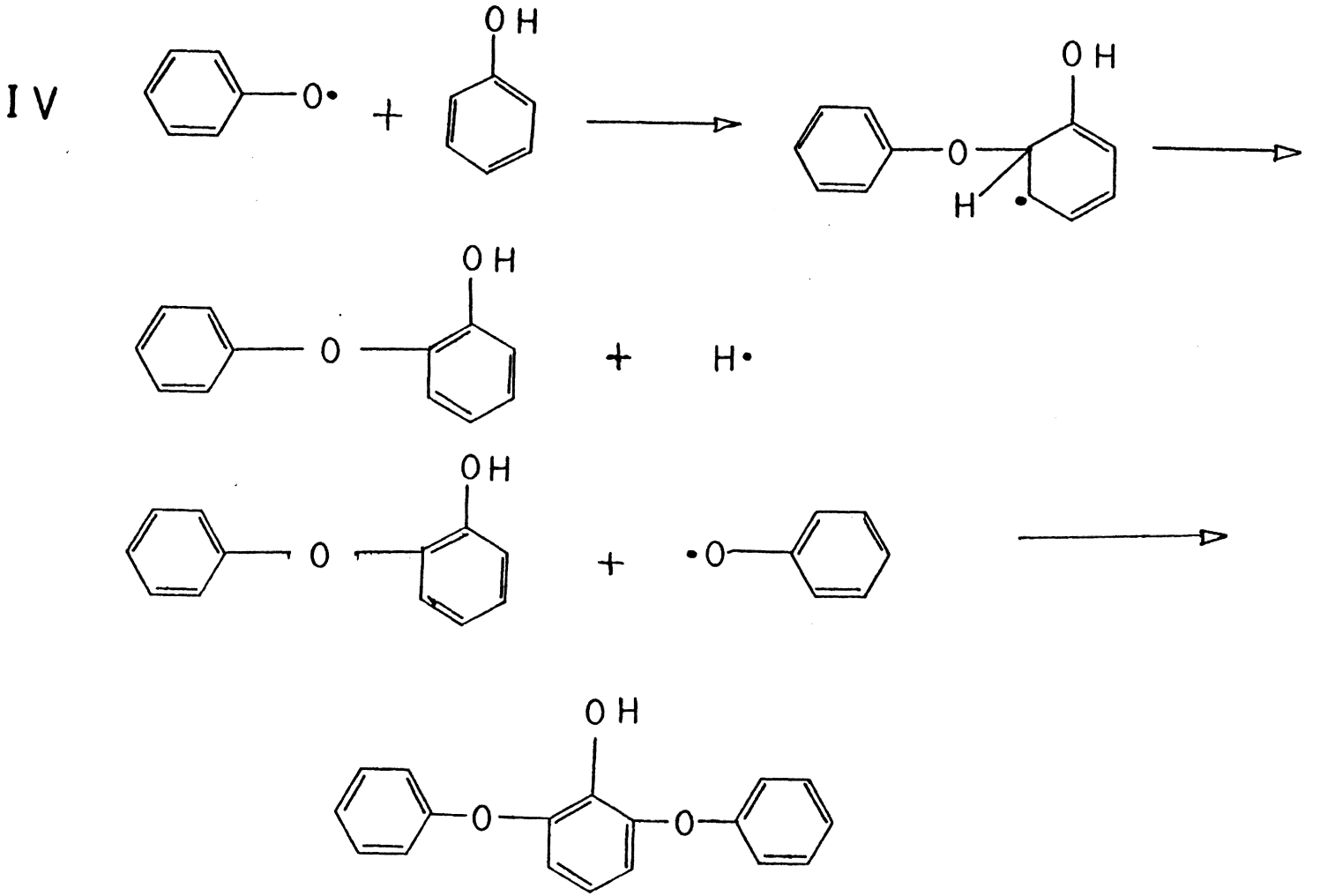

Figure 43 (continued)

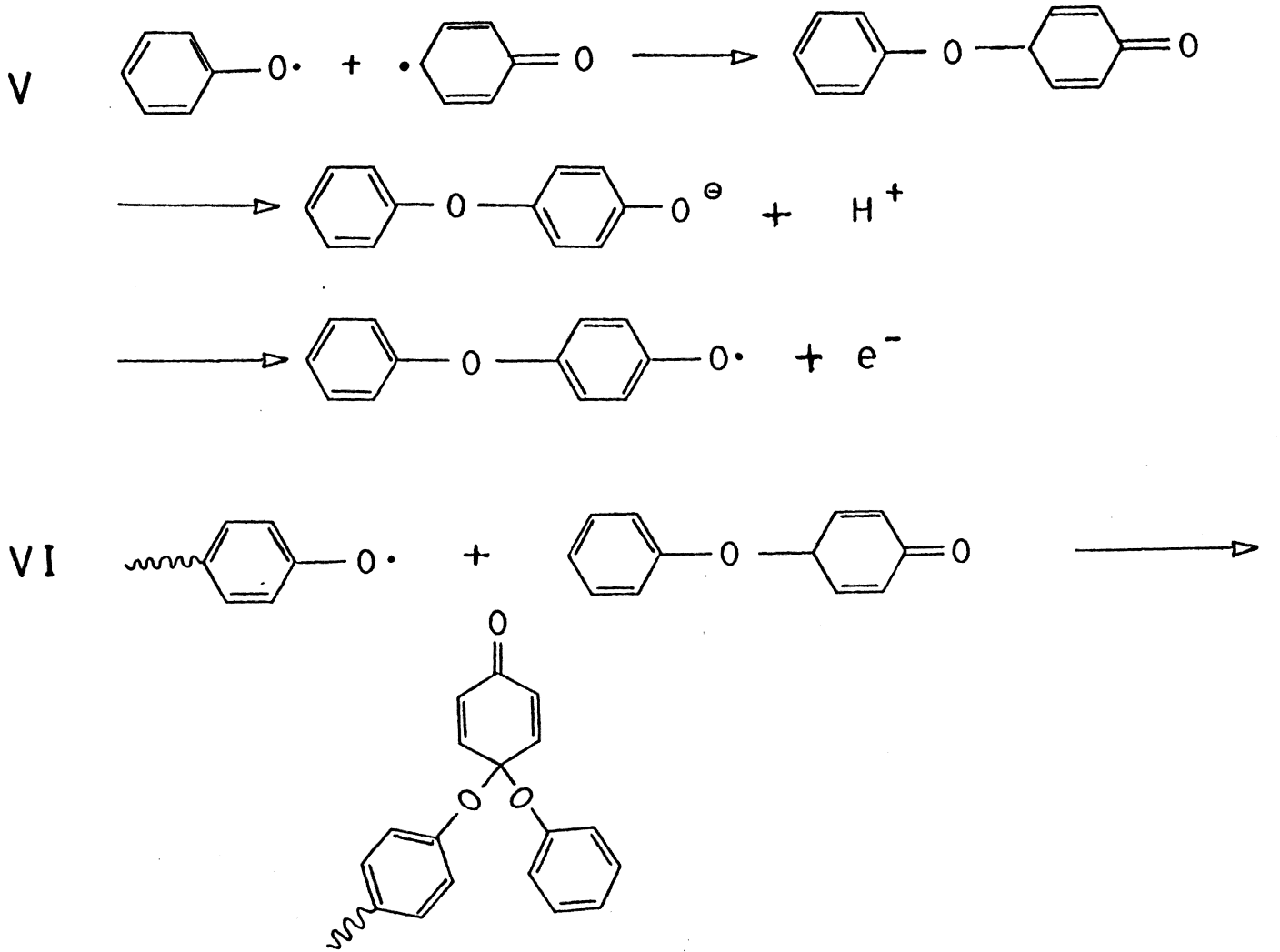

Figure 43 (continued)

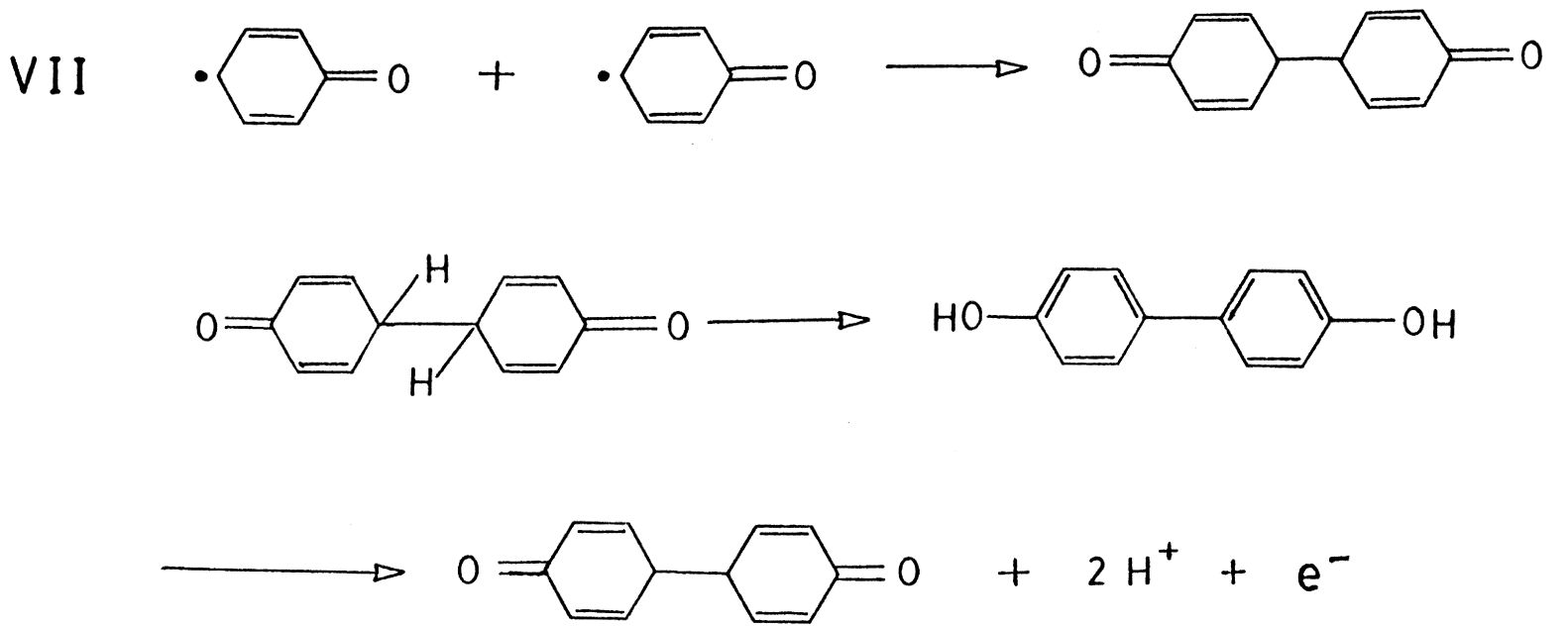

Figure 43 (continued)

radical can rearrange once generated. These resonance forms can then be utilized to describe the propagation or termination steps, if necessary. In the first propagation scheme (IV) a phenolate radical reacts with a phenol molecule to yield a biphenyl-like radical. This radical then undergoes loss of hydrogen and can continue propagation with another phenolate radical. Propogation scheme 2 (V) exhibits head-to-tail coupling of two phenolate radicals. This product can then deprotonate and finally be subjected to anodic oxidation to expand a chain. Two mechanisms have been proposed for termination. The first (VI) involves a polymer chain attaching a phenyl-quinone type compound to form a diphenyl-quinone polymer. The other termination mechanism (VII) involves tail-to-tail coupling of two phenolate radicals to generate a para diphenol. If the diphenoquinone product is desired, electrochemical oxidation is required at higher potentials. The net result is a highly cross-linked polymer of polyphenylene oxide.

Figure 44 exhibits the proposed formation of the nonconducting polymer film on the n-GaAs surface. Natural film formation may occur with flaws and weak spots also being present. The polymer may grow through oxidation or reduction, by creation of radical

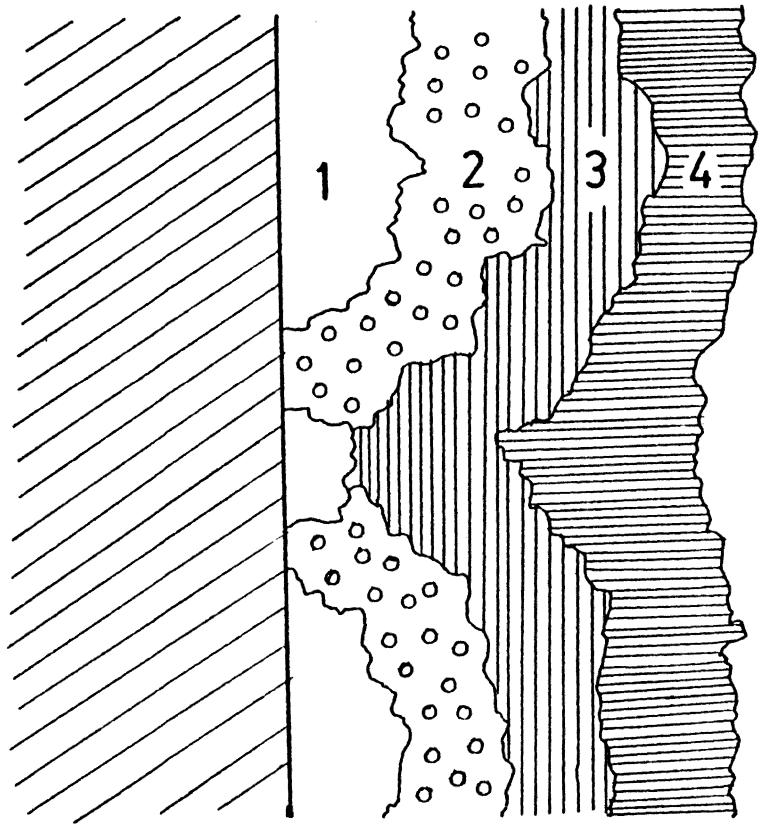

Proposed Formation of Nonconducting Polymer Films on n-GaAs Surface

Figure 44

anions, or by propagation of free radicals after initiation. If an open site on the electrode exists after a sweep, that pinhole then becomes a preferred site in the next subsequent sweep. Thus, a self-healing, self-limiting polymer layer is formed.

After coating of the electrode had been completed, the GaAs electrode was again subjected to photocurrent generation in acidic media. Tables 9, 10 and 11 display these results for the DVB-, and phenol-based coatings. By comparing the uncoated electrode PEC etching results to that of the coated electrode results, it is apparent that the coated electrodes exhibit a somewhat higher corrosion ratio (moles e^-/mole As(III)). The DVB-coated photoelectrode data exhibit only a slightly higher ratio although the coated electrode was etched for a lesser time. The DVB-coated electrode shows a remarkably small number of Coulombs per photo-etch, due to the rather low photocurrent observed. The reason for this is unknown.

Table 10 contains data obtained from the phenol coated n-GaAs photoelectrode, which was coated in 0.3 M $NaOH/CH_3CN$. The mole ratio is up approximately one electron per GaAs for HCl electrolyte data with comparable Q's. The same is true for both HNO_3 etch

Table 9. Photoelectrochemical results for DVB-coated n-GaAs photoelectrode

	Coated		Uncoated	
	moles e-		moles e-	
Electrolyte	Ave mole As(III)	Ave Q(Coul)/etch	Ave mole As(III)	Ave Q(Coul)/etch
H_2SO_4 pH 1.0	2.80±.54	0.00510	2.25±.16	1.110
HCl pH 1.0	2.97±.32	0.0216	2.38±.15	0.751
HNO_3 pH 1.0	3.12±.46	0.0173	2.57±.06	0.476

(etch time = 20 minutes)

Table 10. Photoelectrochemical results for phenol-coated n-GaAs photoelectrode from acetonitrile

Electrolyte	Coated moles e- Ave mole As(III)	Coated Ave Q(Coul)/etch	Uncoated moles e- Ave mole As(III)	Uncoated Ave Q(Coul)/etch
HCl pH 1.0	3.37±.51*	0.681	2.38±.15	0.751
HNO_3 pH 1.0	3.78±.67*	1.55	4.64±.79	1.470
	4.11±1.22	0.776		
pH 3.0/0.1 M KNO_3	4.46±1.78	0.0281	4.03±.53	0.103
			2.95±.31	0.128

*Indicates 60 minutes etch time

All other etch times = 30 minutes

solutions. The etch time for two of the results, pH 1.0 HNO_3 and pH 3.0 HNO_3/0.1 M KNO_3, was extended to check the stability of the coating at longer lifetimes.

Finally, Table 11 displays the results from the phenol coating as deposited from 0.1 M NaOH/CH_3OH. These results attained the theoretical six electrons per As(III). Although some were obtained from a shorter photoelectrochemical etch time (10 minutes), these results were only slightly higher than the 30 minute etches.

As for the stability of these layers, it can be concluded that for DVB, the polymer coating was not sufficiently stable enough to completely suppress corrosion of the n-GaAs semiconductor electrode yet it did offer some corrosion protection in weakly acidic media. As for the polyphenylene oxide coating, results from film deposition from the methanol media offered far better protection than those from the acetonitrile media (although weak bases are stronger in CH_3CN than in CH_3OH). This may be partially due to the greater ionization of phenol in methanol as opposed to acetonitrile, thus leading to a more tightly cross-linked polymer coating. These results reflect short term corrosion protection; very long

Table 11. Photoelectrochemical results for phenol-coated n-GaAs photoelectrode from methanol

Electrolyte	Coated: moles e- / Ave mole As(III)	Coated: Ave Q(Coul)/etch	Uncoated: moles e- / Ave mole As(III)	Uncoated: Ave Q(Coul)/etch
H_2SO_4 pH 1.0	6.34± .79	1.032	2.25±.16	1.110
	6.75±1.41*	0.922	2.07±.06	1.201
			2.36±.09	0.900
pH 3.0 /0.1 M Na_2SO_4	6.56±1.91	0.137	3.86±.42	0.106
			3.17±.39	0.120
HCl pH 1.0	7.95± .62	0.823	2.38±.15	0.751
	8.23± .46*	0.779		
pH 3.0 /0.1 M NaCl	8.41± .30	0.141	3.01±.85	0.119
	8.59±1.00*	0.138		

*Indicates 10 minutes etch time

term stability is not known.

D. Rotating Ring-Disc Voltammetry

Rotating ring-disc voltammetry is useful for determining the kinetics of homogeneous reactions in solution. (59) (83) (84) Reactants can be oxidized or reduced at the disc and further oxidized or reduced, if desired, at the ring. In this manner, the product generation rate can be easily controlled by the disc. The transport of the electroactive species to the disc occurs via convective flow. The same convective flow carries disc reaction products across the electrode. With the aid of the circuit in Figure 45 the potential of one of the electrodes was fixed while the other was scanned. The currents of both electrodes were plotted on two x-y recorders as a function of the sweep potential.

By utilizing a reversible redox couple such as Fe^{+2}/Fe^{+3}, one can observe the rate of electron transfer at clean and coated electrodes. The use of redox couples in the RRDE system allows analysis of surface reactions on the photoelectrode. With redox couples present, one can consume holes at the surface, slow down the rate of corrosion (depending on the operating conditions), or slow the growth of an oxide film on the electrode surface. (72) (85-87) By controlling the pH of the electrolyte, the rate of

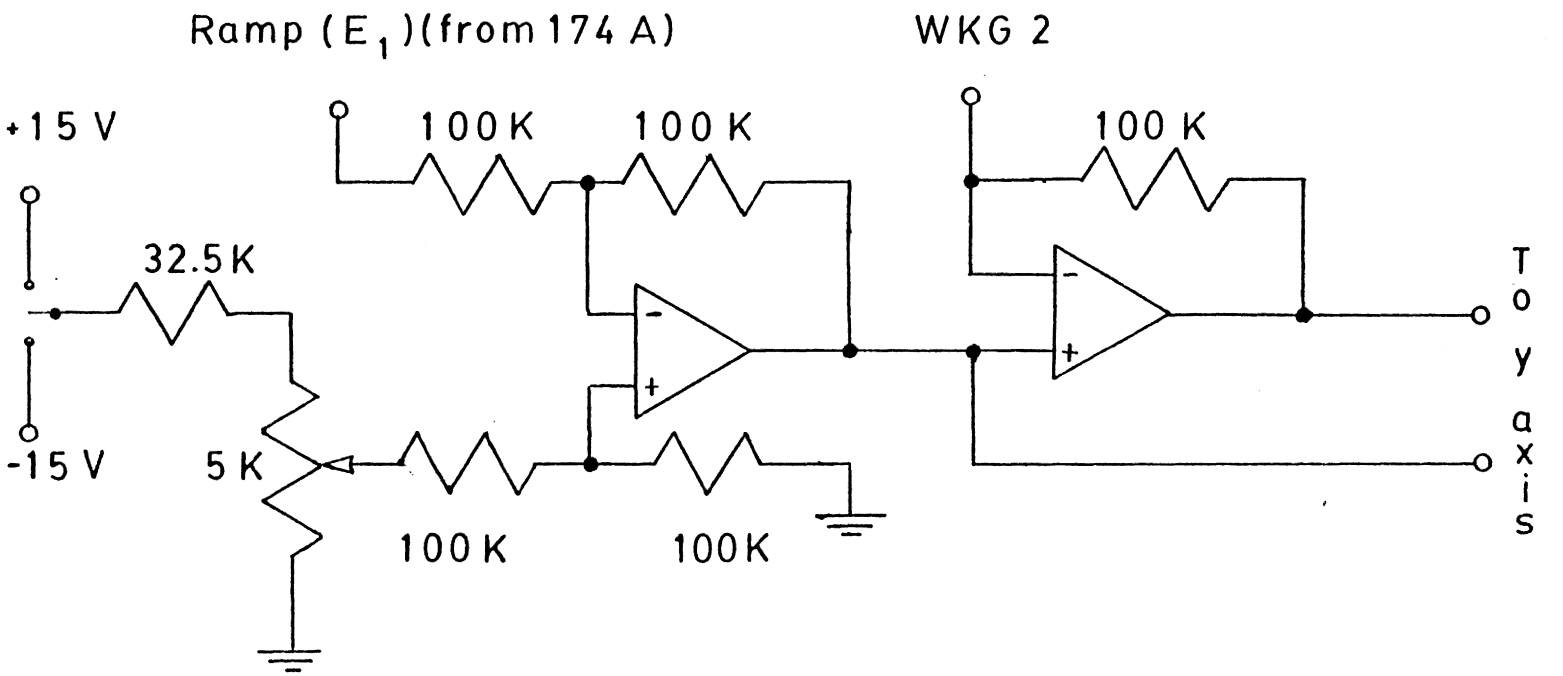

Rotating Ring-Disc Accessory

Figure 45

photocorrosion can also be affected, higher rates occurring at extreme pH's and lower rates occurring at medium pH's. (85)

From this the collection efficiency, defined as the ratio of ring and disc currents, can be determined. Theoretically, the collection efficiency is dependent only on the dimensions of the ring, disc, and separator--not the rotational speed. (84) The collection efficiency can be represented by eq. 1. (43)

$$N = 1 - F(\alpha/\beta) + \beta^{2/3}\,[1 - F(\alpha)] - (1+\alpha+\beta)^{2/3}\,\{1-F[(\alpha/\beta)(1+\alpha+\beta)]\} \quad \text{(eq. 1)}$$

$$\text{where } \alpha = (r_2/r_1)^3 - 1 \quad \text{(eq. 2)}$$

$$\beta = ((r_3/r_1)^3 - (r_2/r_1)^3)^{2/3} \quad \text{(eq. 3)}$$

where r_1 is the radius of the disc, r_2 is the radius of the separator, and r_3 is the radius of the ring. All three radii have been determined and N calculated. With r_1= 0.300 cm, r_2 = 0.375 cm, and r_3 = 0.425 cm, the theoretical collection efficiency was N = 0.2398.

A Pt ring electrode was used to illustrate the stationary and rotating ring electrodes under similar conditions. (See Figure 46 and 47.) It should be noted that H_2 oxidation (anodic) and H_2 formation (cathodic) waves (88) occurring near zero volts are

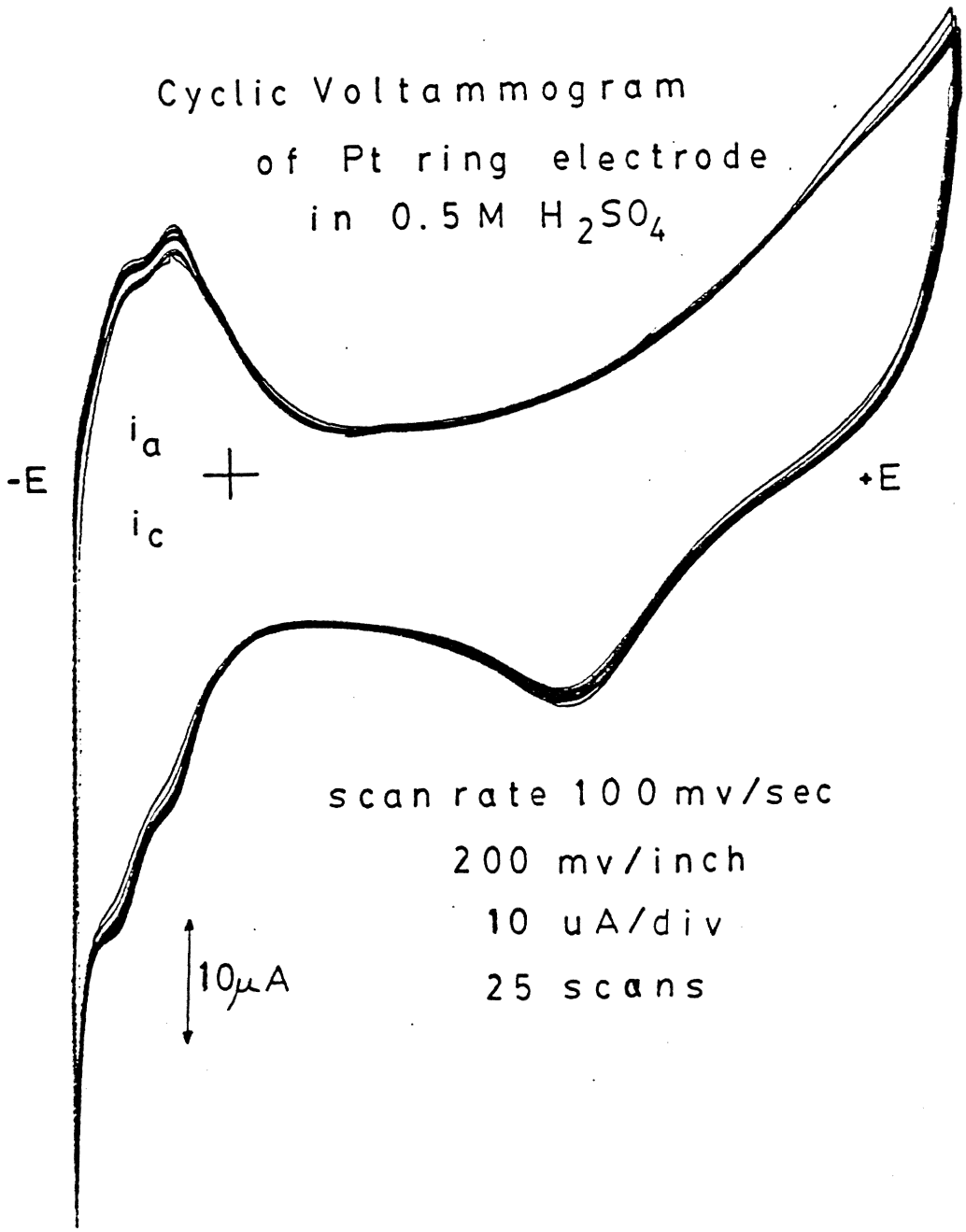
Cyclic Voltammogram
of Pt ring electrode
in 0.5 M H_2SO_4
i_a
i_c
-E
+E
scan rate 100 mv/sec
200 mv/inch
10 uA/div
25 scans
10μA

Figure 46

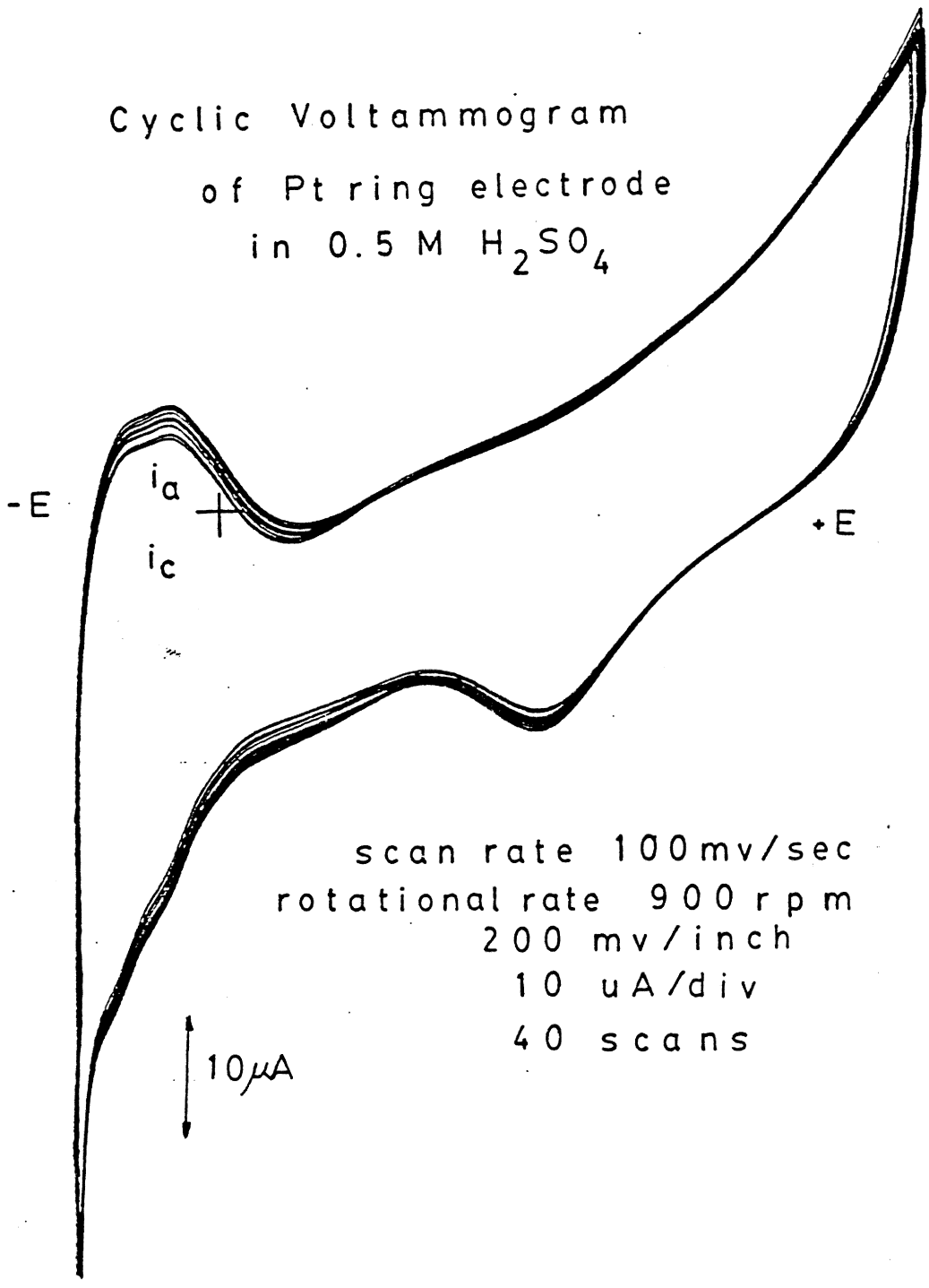
Cyclic Voltammogram
of Pt ring electrode
in 0.5 M H_2SO_4
-E
i_a
i_c
+E
scan rate 100mv/sec
rotational rate 900 rpm
200 mv/inch
10 uA/div
40 scans
10μA

Figure 47

not as noticeable on the rotating ring electrode. The surface oxide reduction, near +.46 volts vs. SCE, had not been affected by the rotation, even at speeds of 2500 rpm. These scans indicate a clean platinum ring electrode.

Figure 48 illustrates the ring current produced from an $Fe^{II}(EDTA)/Fe^{III}(EDTA)$ redox couple in 100 mM EDTA, 40 mM $Fe(ClO_4)_2$ at pH 7.0. Curve (a) shows the mass transfer of the $Fe^{II}(EDTA)$ at a rotating Pt ring electrode. As it can be seen, by rotating the ring the plateaus obtained are convection limited. Also, the sweep rate is kept at slow speeds (~10 mV/sec) to reduce charging currents. Similar curves (Figure 49) were obtained at different rotational speeds to determine if I_{lim} was proportional to $\omega^{1/2}$. The dependence of I_{lim} on ω is given by the Levich equation:

$$I_{lim} = 0.620\ n\ F\ A\ C^*\ D^{2/3}\ \omega^{1/2}/v^{1/6}$$

where I_{lim} is the convection limited current, n is the number of electrons transferred per molecule, F is Faraday's constant, A is the electrode area, D is the diffusion coefficient of the observed species C*, and v is the scan rate. By plotting I_{lim} vs. $\omega^{1/2}$ (Figure 50 and Table 12), one can check to see if Levich behavior is obtained.

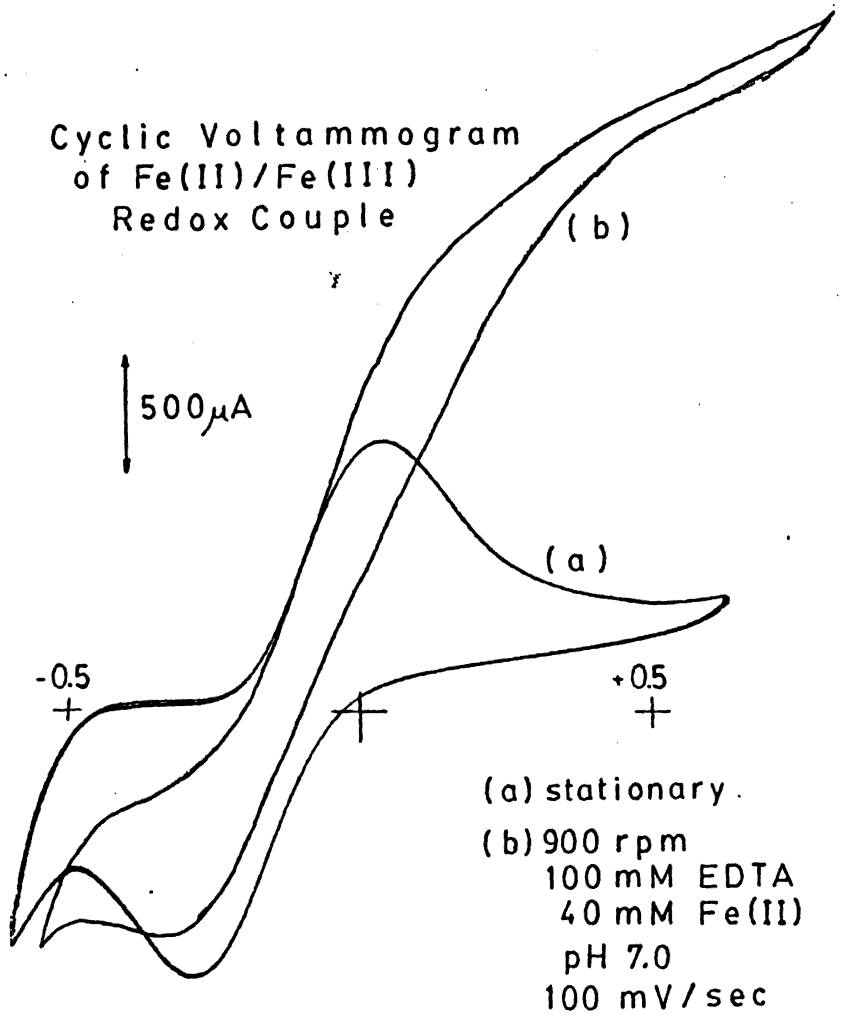
Cyclic Voltammogram
of Fe(II)/Fe(III)
Redox Couple
(b)
500μA
(a)
-0.5
+0.5
(a) stationary.
(b) 900 rpm
100 mM EDTA
40 mM Fe(II)
pH 7.0
100 mV/sec

Figure 48

Cyclic Voltammogram of Fe(II) at a Rotating Pt Ring Electrode for Levich Data

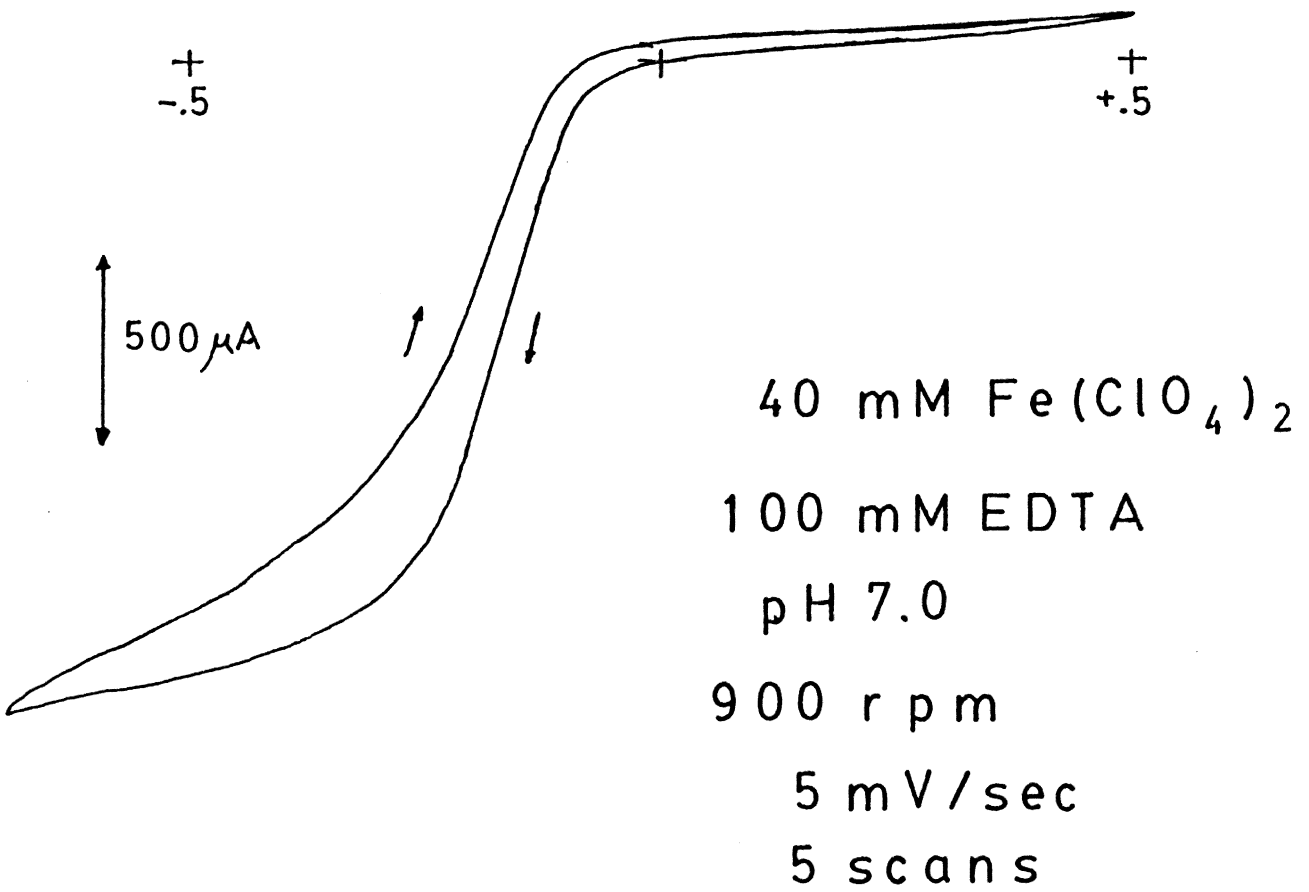

Figure 49

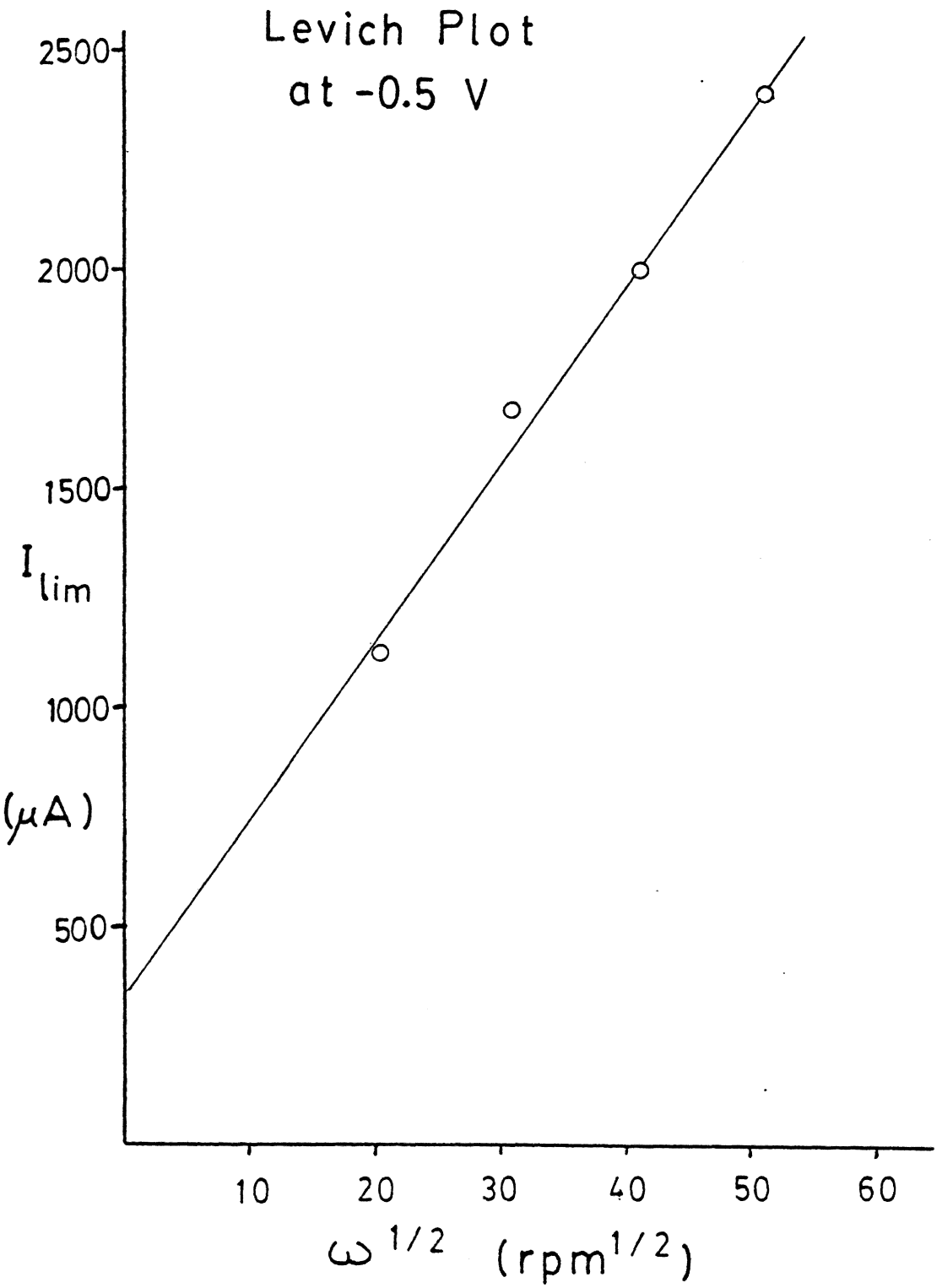
Levich Plot
at -0.5 V
2500
2000
1500
1000
500
I_{lim}
(μA)
10
20
30
40
50
60
$\omega^{1/2}$ ($rpm^{1/2}$)

Figure 50

Table 12

$\omega^{1/2}(rpm^{1/2})$	I_{lim} (μA) at -0.5 V	I_{lim} (μA) at -0.6 V
20	1128	1144
30	1572	1550
40	1910	1965
50	2300	2380
60	2420	2510

By comparing the measured collection efficiency to the theoretical collection efficiency, one can determine hole corrosion rates. Frese et al. (22) (24) (89) (90) used this method by employing a redox couple as a stabilizing agent against corrosion to compete for holes at the n-GaAs disc electrode. By measuring the fraction of holes oxidizing Fe^{II}(EDTA) versus the fraction of holes corroding the n-GaAs photoelectrode, they determined the stabilization ratio. They concluded that at intermediate pH's, the highest stabilization ratios are obtained.

The n-GaAs disc was used to check if electron transfer occurred in the dark. No significant current was observed beyond the normal dark current of the disc when Fe^{III}(EDTA) generated at the disc reached the ring and was reduced back to Fe^{II}(EDTA). The ratio of the anodic and cathodic currents, the collection efficiency, was approximately 7.3%. As it can be seen in Figure 51, as the disc photocurrent increased, the ring current reciprocated by increasing cathodically. This suggests passivation by an oxide layer.

Prior to coating the n-GaAs electrodes, coatings were formed on metal electrodes to test their effect on mass transfer to the electrode. Figure 52

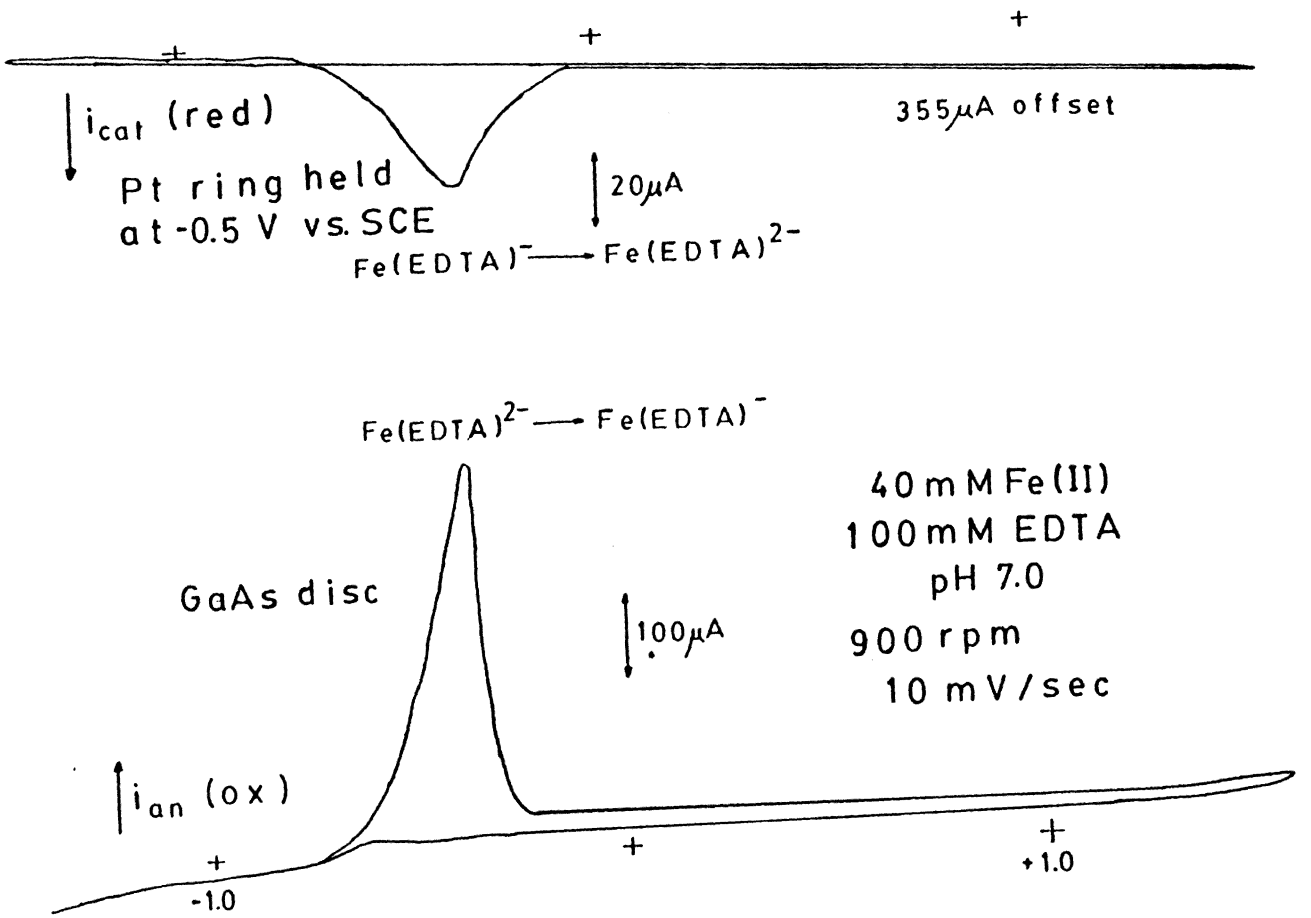

Photocurrent Generation

Figure 51

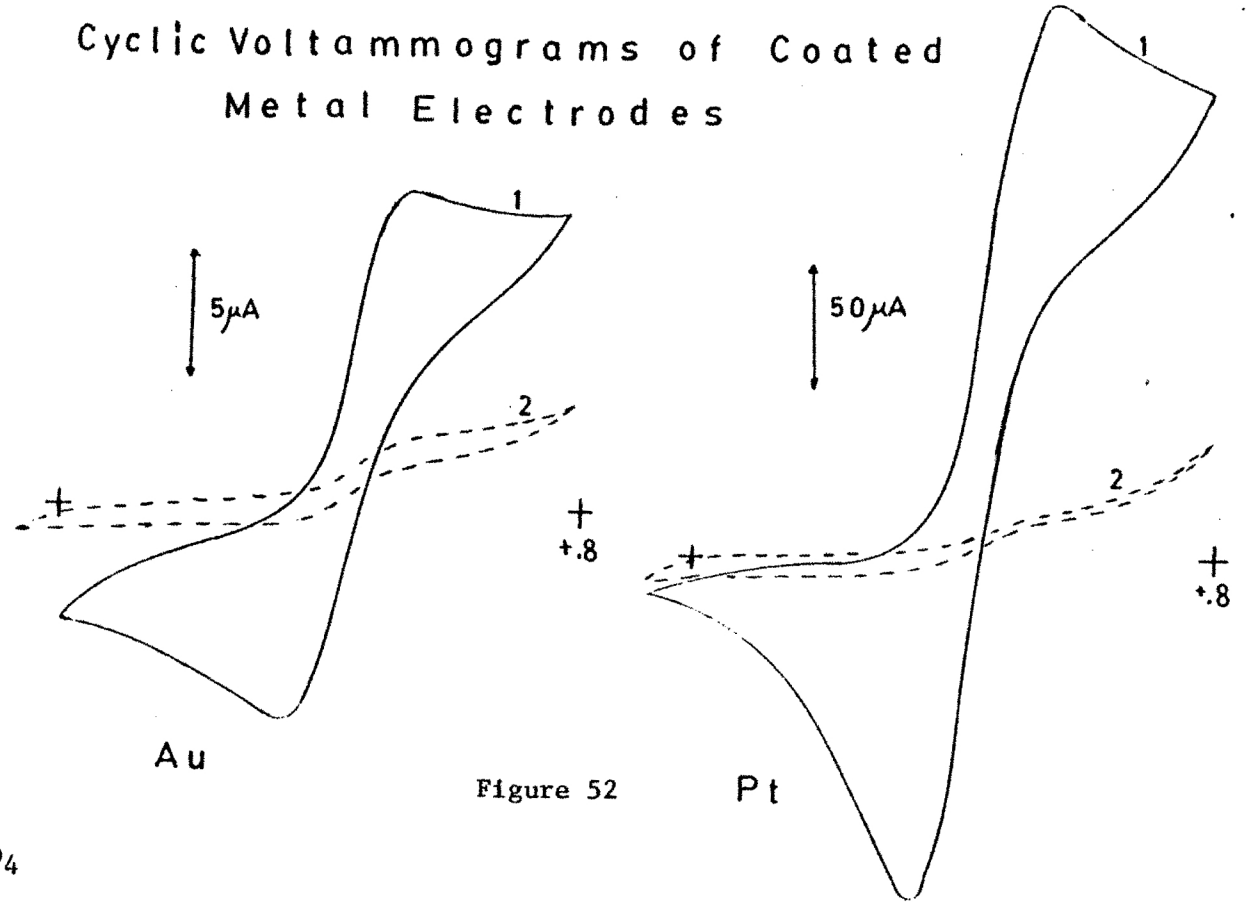

Figure 52

4 scans
0.5 M H_2SO_4
50 mV/sec
(1) clean
(2) phenol coated from 42 mM phenol/0.1 M NaOH/CH_3OH
Au - 5 mM Fe^{+2} Pt - 25 mM Fe^{+2}

represents the effect of a phenol coating on Au and Pt electrodes. Both curves are cyclic voltammograms of clean disc electrodes in 0.5 M H_2SO_4. After a successful coating of polyphenylene oxide (generated in 0.1 M $NaOH/CH_3OH$), the electrodes were placed into their respective Fe^{+2} solutions and reanalyzed. The polyphenylene oxide layer inhibited the diffusion of Fe^{+2} to the disc electrode surfaces. Thus, the polyphenylene oxide layer acted as a blocking layer between the electrodes and their electrolytes. By reducing Fe^{+2} mass transport to the electrode surface, less electrochemistry of the species under investigation could be observed.

Electrochemistry of phenol at both stationary and rotating n-GaAs disc electrodes was performed. Figure 42 represents the behavior of phenol oxidation at a stationary n-GaAs electrode while Figure 53 exhibits the phenol oxidation at a rotating n-GaAs disc photoelectrode when illuminated. The characteristic blue color on the disc surfaces was observed for both stationary and rotating n-GaAs disc photoelectrodes.

Several redox couples were used in the analyses. They include I^-, $Fe^{+2}/^{+3}$, Fe^{II}(EDTA), and ferroin. Initial RRDE experiments concentrated on using iodide to produce I_3^-, triiodide. Figure 54 illustrates the

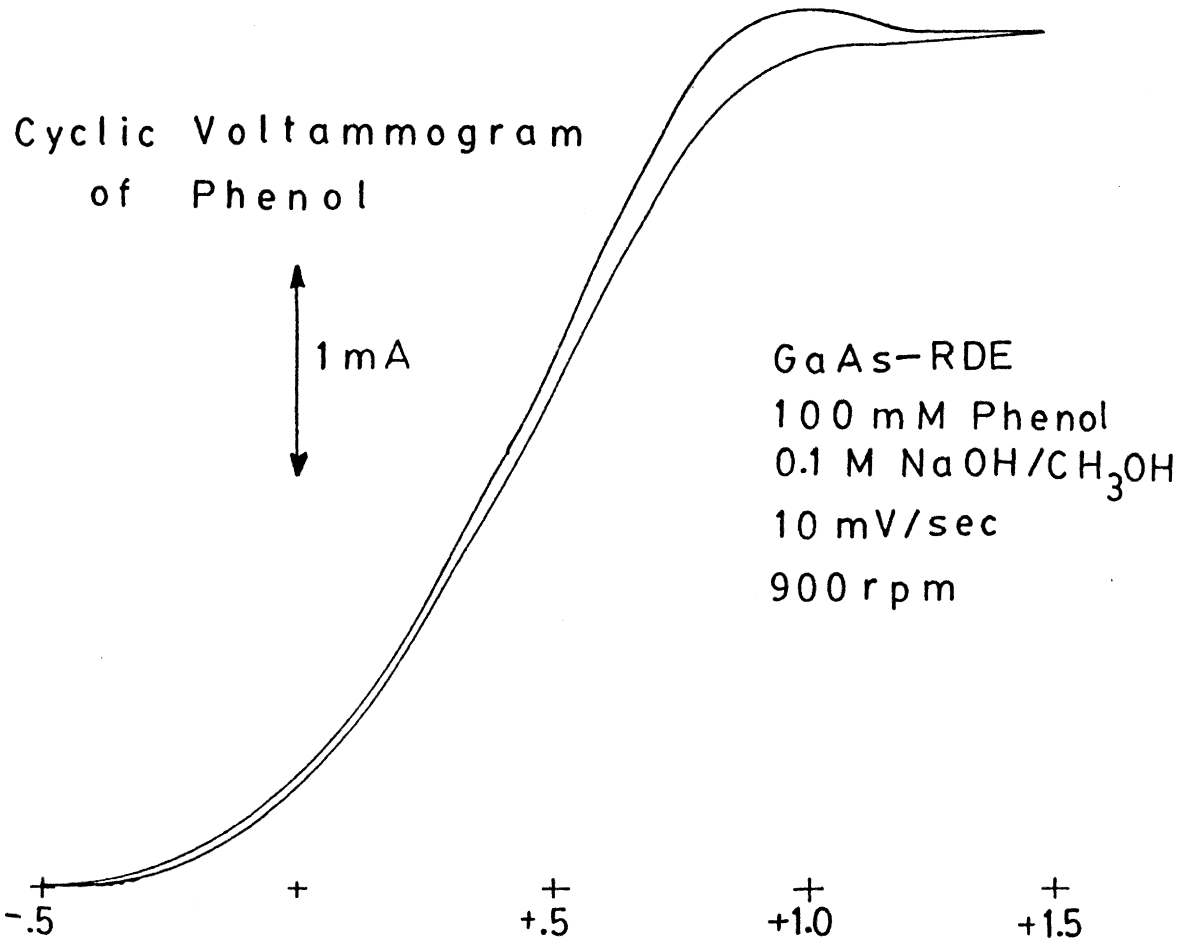
Cyclic Voltammogram
of Phenol
1 mA
GaAs-RDE
100 mM Phenol
0.1 M NaOH/CH3OH
10 mV/sec
900 rpm
-.5
+.5
+1.0
+1.5

Figure 53

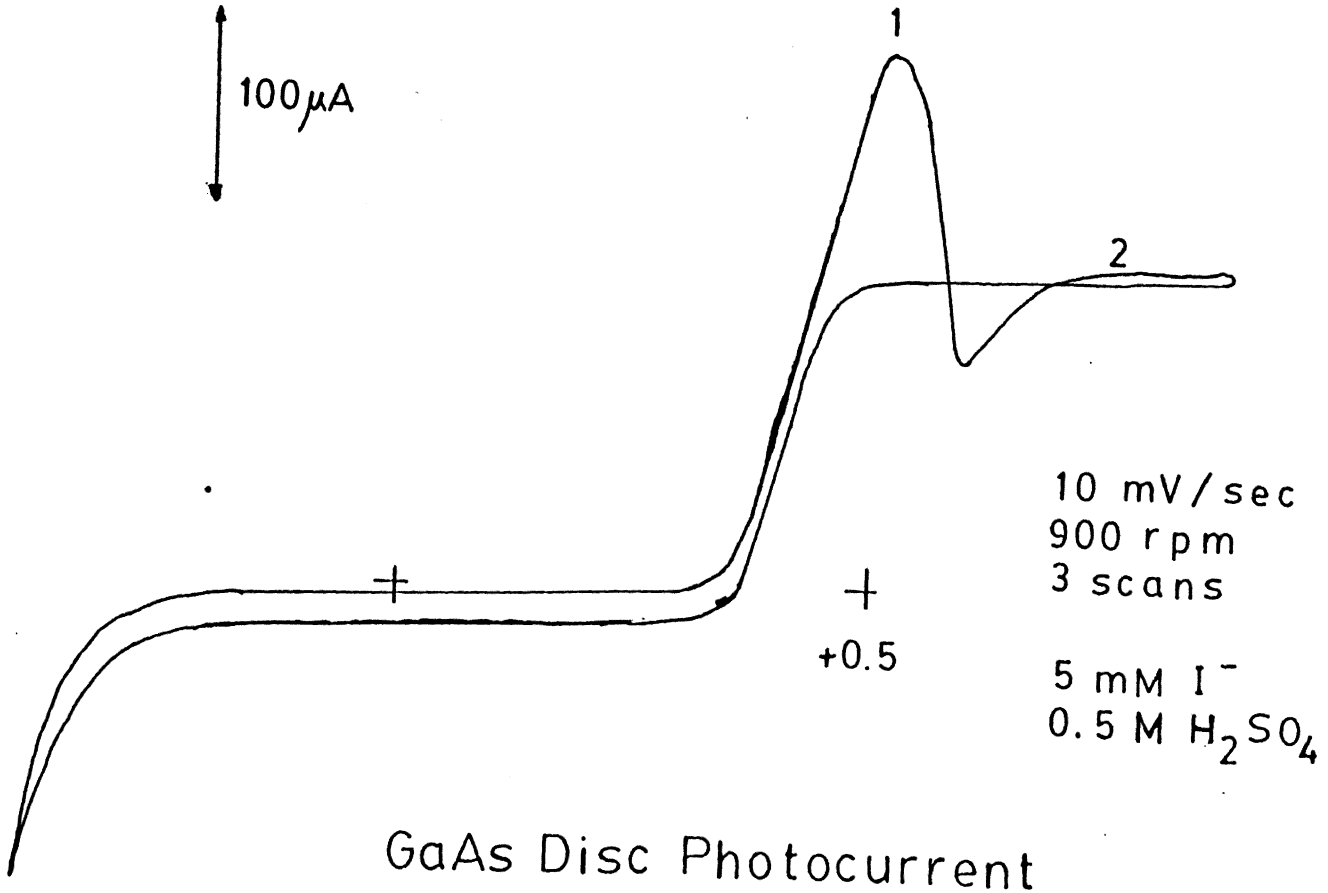
100μA
1
2
10 mV/sec
900 rpm
3 scans
+0.5
5 mM I⁻
0.5 M H₂SO₄
GaAs Disc Photocurrent
Generation

Figure 54

anodic photocurrent in iodide electrolyte. The ring current, which was set to detect I_3^-, (not shown here) showed no change as the disc potential changed. No I_3^- was being released into the electrolyte. Possibly, an insoluble coating was being formed on the disc. Notice the strange shape of the disc photocurrent.

Ferroin, also known as o-phenanthroline ferrous sulfate, was used as a hole scavenger in 0.5 M H_2SO_4. Ring-disc voltammetry revealed (See Figure 55) that as disc photocurrent was generated a broad and slowly rising current developed at the ring. No peak was observed for ferroin oxidation at the disc nor any reduction peak of any kind at the ring. This might be due to degradation of the ferroin by air oxidation or by a contaminant mixed in the ferroin which might suppress the oxidation or reduction waves. Thus, research on ferroin was discontinued.

The Fe^{+2}/Fe^{+3} redox couple was attempted in 0.5 M H_2SO_4. When photoelectrochemistry was tried, no Fe^{+3} was detected at the ring electrode. Even though the Pt ring potential was held at +1.0, 0.0, and -1.0 volts vs. SCE, the ring current did not vary as a function of the disc photocurrent. Therefore, the holes not oxidizing the Fe^{+2} must have been oxidizing

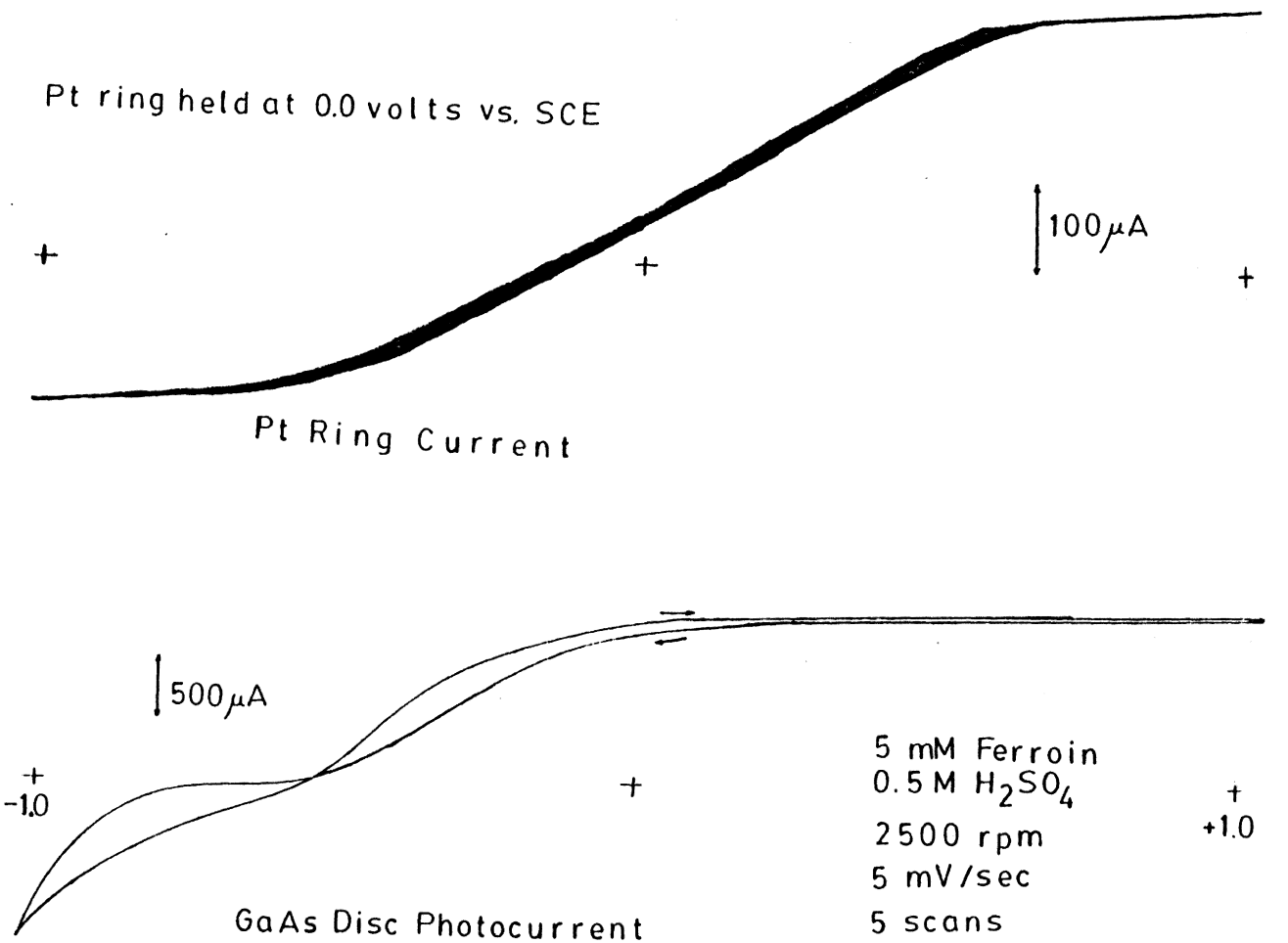

Figure 55

RRDE Photocurrent generation - ferroin

the GaAs.

The $Fe^{II}(EDTA)/Fe^{III}(EDTA)$ redox couple was attempted in 100 mM EDTA at pH 7.0. By placing 5 mM $Fe^{III}(EDTA)$ in solution to initially establish a one-to-one concentration ratio in the first experiment, the formal potential was established for the couple. The ring electrode was set at that potential to keep the "dark" current low. Reports by Menezes et al. (85), Decker et al. (86), and Frese et al. (22) (24) (89) (90) indicated that the oxidation of $Fe^{II}(EDTA)$ was observed on a GaAs electrode in a neutral pH range.

Figure 56 displays RRDE data obtained in a 100 mM EDTA pH 7.0 media with 5 mM $Fe^{III}(EDTA)$ and 20 mM $Fe^{II}(EDTA)$ present. The disc potential was initially scanned in the dark (dashed lines) to see if either $Fe^{II}(EDTA)$ was oxidized at the disc or if the product $Fe^{III}(EDTA)$ was reduced at the ring. No excess Fe^{+3} was detected in the dark. When the disc was illuminated (solid lines), the anodic disc current began to increase substantially near -0.70 volts vs. SCE. At the same time the ring current increased cathodically. Near -0.40 volts the currents peaked and receded immediately afterwards. Subsequently, the disc maintained a low saturation current level.

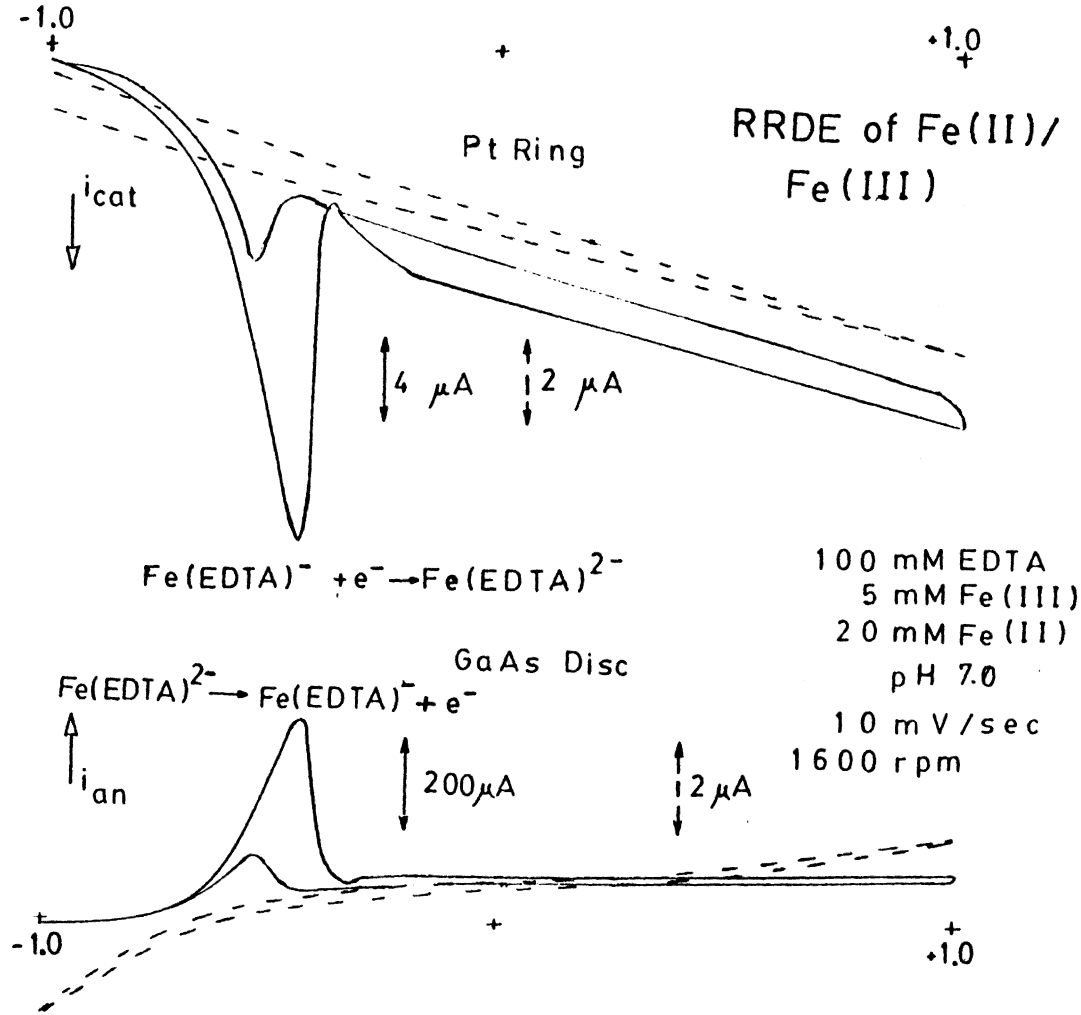
-1.0
+1.0
Pt Ring
RRDE of Fe(II)/
Fe(III)
i_{cat}
4 μA
2 μA
$Fe(EDTA)^- + e^- \rightarrow Fe(EDTA)^{2-}$
100 mM EDTA
5 mM Fe(III)
20 mM Fe(II)
pH 7.0
10 mV/sec
1600 rpm
GaAs Disc
$Fe(EDTA)^{2-} \rightarrow Fe(EDTA)^- + e^-$
i_{an}
200μA
2 μA
-1.0
+1.0

Figure 56

On the return scan, again a small current rise was observed at both ring and disc. These correspond to the same reactions as the larger peaks.

This "passivation" effect was observed by Decker et al. (86) for Ce^{+4}/Ce^{+3} on an RRDE (GaAs disc) system. Results by Menezes and Miller (40) at pH 5.0 in 0.5 M HOAc/0.5 M NaOAc demonstrated similar results. They proposed that three reactions were occurring at the RRDE/electrolyte interface: (1) reduction of Fe^{III}(EDTA) at the ring, (2) oxidation of Fe^{II}(EDTA) at the disc, and (3) passivation of the disc surface. Finally, Frese et al. (22) (24) (89) (90) commented that the holes arriving at the n-GaAs disc surface from the bulk of the crystal oxidized the Fe^{II}(EDTA) at the disc. It was also stated that the holes are competed for by Fe^{II}(EDTA) and H_2O. When the H_2O is oxidized in neutral pH, insoluble Ga_xO_y products are formed on the disc surface thereby creating a passivation layer.

To summarize, the redox chemistry observed involved both RRDE work and photoelectrochemistry. In the case of ferroin, oxidation of the Fe(II) species was not observed. As for iodine, the oxidation of I^- appeared to be occurring at the GaAs disc with quenching of the signal immediately afterwards. No

reduction current was observed at the ring indicating that soluble oxidation products of I^- were formed. Also, for the Fe^{+2}/Fe^{+3} couple in 0.5 M H_2SO_4, no hole capture by Fe^{+2} was observed. This may be due to a higher corrosion rate of the GaAs disc at lower pH. Finally, in pH 7.0 solution the $Fe(EDTA)^{2-/-}$ redox couple was observed to capture holes from the GaAs disc photoelectrode. Hole injection was confirmed by the way in which the ring current tracked the disc photocurrent. In strong acid the dissolution reaction of the GaAs to yield soluble products may have been faster than the ability of the redox couples to reach the GaAs disc surface.

The final topic of discussion is the collection efficiency, N. Results were obtained by comparing the ring current to the disc current at various Fe(II) concentrations. In order to maximize the current signal of the ring electrode, the formal potential was adjusted to give increased sensitivity. Tables 13 and 14 contain data for the collection efficiencies of clean and polyphenylene oxide coated n-GaAs disc photoelectrodes using the $Fe^{II}(EDTA)/Fe^{III}(EDTA)$ couple. For both electrodes, as the Fe(II) concentration increased, the collection efficiency increased. (See Figure 57.) This confirmed results as

Table 13. Collection efficiencies of clean n-GaAs disc photoelectrode using Fe(II)/Fe(III) redox couple

Scan	[Fe(III)]μM	$E^{\circ\prime}$ (volts)	i_{disc}(μA)	i_{ring}(μA)	$N=i_r/i_d$	N_{obs}/N_{theor}
1f	5	-.133	550	11.3	.0205	.0855
1b			375	7.6	.0203	.0847
2f			550	10.8	.0196	.0817
2b			375	7.4	.0197	.0822
1f	10	-.152	560	16.8	.0300	.1251
1b			283	9.0	.0318	.1326
2f			520	15.9	.0306	.1276
2b			218	8.0	.0367	.1530
1f	20	-.169	420	17.4	.0414	.1726
1b			140	5.8	.0414	.1726
2f			440	17.5	.0398	.1660
2b			107	4.2	.0393	.1639
1f	40	-.183	1900	63.0	.0332	.1384
1b			1675	65.0	.0388	.1618
2f			1900	56.0	.0295	.1230
2b			1650	61.0	.0370	.1543

[Fe(III)] = 5 mM

ω = 1600 rpm

v = 10 mV/sec

f...forward

b...back

Table 14. Collection efficiencies of polyphenylene oxide coated n-GaAs disc photoelectrode using Fe(II)/Fe(III) redox couple

Scan	[Fe(II)]μM	E^{o1} volts	i_{disc}(μA)	i_{ring} (μA)	$N = i_r/i_d$	$\frac{N_{obs}}{N_{theor}}$
1f	5	-.137	790	11.6	.0147	.0613
1b			562	7.7	.0137	.0571
2f			745	10.0	.0134	.0559
2b			522	6.4	.0123	.0513
1f	10	-.153	612	9.8	.0160	.0667
1b			380	5.9	.0155	.0646
2f			560	8.5	.0152	.0634
2b			378	5.4	.0143	.0596
1f	20	-.172	437	10.9	.0249	.1038
1b			140	4.1	.0293	.1222
2f			420	10.7	.0255	.1063
2b			136	3.7	.0272	.1134
1f	40	-.185	505	11.9	.0236	.0984
2f			465	11.7	.0252	.1051
3f			310	8.3	.0268	.1118

No back observed

n-GaAs disc coated in 100 mM phenol in 0.1 M NaOH/CH_3OH

[Fe(III)] = 5 mM

ω = 1600 rpm

v = 10 mV/sec

f...forward

b...back

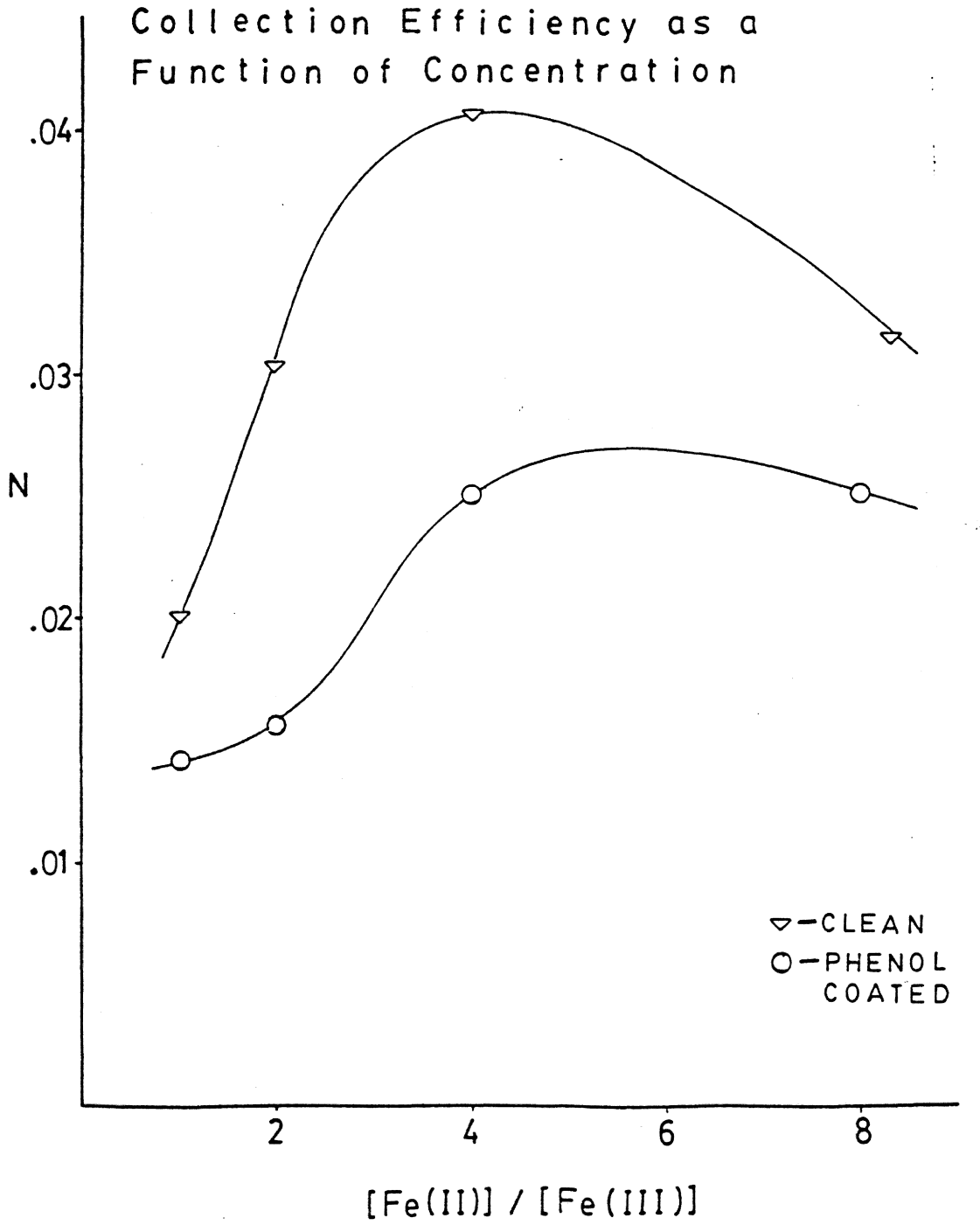
Collection Efficiency as a
Function of Concentration
.04
.03
.02
.01
N
2
4
6
8
[Fe(II)] / [Fe(III)]
▽—CLEAN
O—PHENOL
COATED

Figure 57

obtained by Frese et al. (50) that the collection efficiencies he obtained increased up to 100 mM Fe^{II}(EDTA) whereupon i_{ring} equaled i_{disc} (N = 100%). As the formal potential shifted negatively with increasing Fe(II) concentration, the collection efficiency increased. (See Figure 58.) By comparing the data of the clean n-GaAs disc photoelectrode to the polyphenylene oxide coated n-GaAs disc photoelectrode, it is clear that the polyphenylene oxide coating is not improving the collection efficiency. Secondly, as the Fe^{II}(EDTA) concentration increased, currents at the coated disc electrode decreased. This is also supported by the data obtained by Fe^{+2} in 0.5 M H_2SO_4.

Finally, as a general observation, the collection efficiencies increased with Fe(II) concentrations on both clean and coated electrodes.

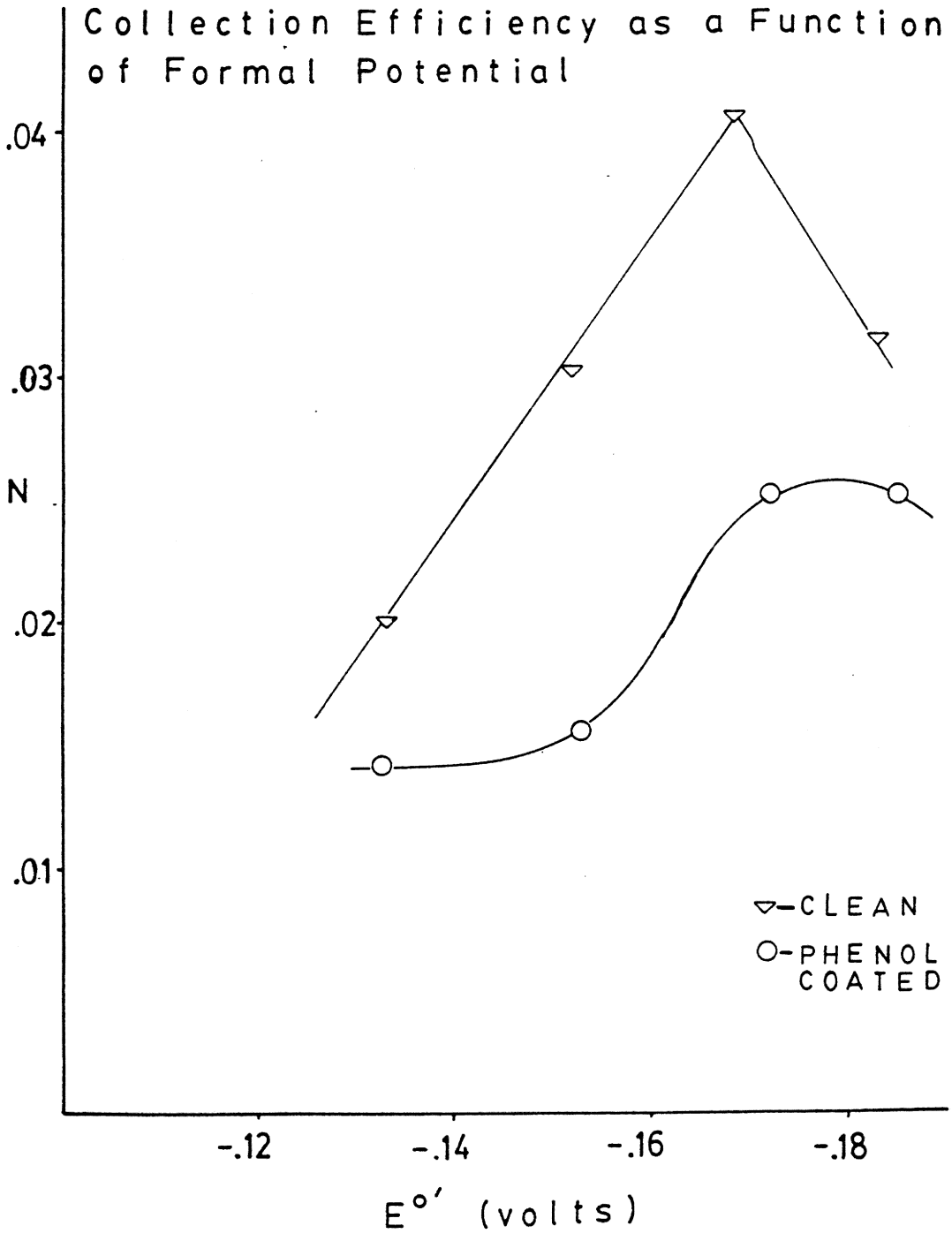
Collection Efficiency as a Function of Formal Potential
.04
.03
N
.02
.01
-.12
-.14
-.16
-.18
E°' (volts)
▽-CLEAN
O-PHENOL COATED

Figure 58

IV. CONCLUSIONS

Electrochemical techniques are very useful in determining the corrosion rate of n-GaAs semiconductor liquid-junction solar cells. Differential pulse polarography allows one to analyze corrosion products individually as long as their redox potentials do not overlap. The generation of photocurrent on the n-GaAs photoelectrode in acidic media indicates that dissolution of the electrode surface occurs by holes, giving primary corrosion products as Ga(III) and As(III). When the pH is neutral, a passivation layer, consisting primarily of Ga_2O_3 and As_2O_3 grows on the surface. Using the $Fe(EDTA)^{2-/-}$ redox couple, one can observe the capture of holes from the GaAs disc photoelectrode via RRDE experiments. The observation of corrosion in acidic media for clean n-GaAs electrodes is confirmed by DPP data. Non-electroactive coatings of silane and divinylbenzene provided some protection but not enough to significantly improve the electron to As(III) ratio to six. The polyphenylene oxide layers on n-GaAs photoelectrodes offered better corrosion protection in weakly acidic media. The polyphenylene oxide coatings deposited from the methanol media offered better protection than the same deposited from the acetonitrile media. This may be due

to better cross-linking of the polymer coating in the methanol media.

Finally, by using redox couples to observe hole capture at the electrode/electrolyte interface, it was noted that the clean electrodes yielded better results in neutral pH than polymer coated electrodes. Clearly, the polyphenylene oxide coated n-GaAs photoelectrodes did not improve the collection efficiency. Also, as the Fe^{II}(EDTA) concentration increased, currents at the coated disc electrode decreased. But generally, the collection efficiencies increased with Fe(II) concentrations on both clean and coated electrodes.

REFERENCES

(1) New York Times, February 13, 1934, VIII, 5:2.

(2) Cotton, F. Albert, "Chemical Applications of Group Theory", John Wiley & Sons, Inc., NY, 1971, pp. 123-128.

(3) Myamlin, Viktor A., and Pleskov, Yurii V., "Electrochemistry of Semiconductors", Plenum Press, NY, 1967, pp. 1-7.

(4) Burford, William Berryman, III, and Verner, H. Grey, "Semiconductor Junctions and Devices", McGraw-Hill, Inc., NY, 1965, pp. 5-17.

(5) Phillips, J. C., "Bonds and Bands in Semiconductors", Academic Press, Inc., NY, 1973, pp. 2-11.

(6) Finklea, Harry Osborn, Journal of Chemical Education, 1983, 60, 325-327.

(7) Morrison, Michael A., Estle, Thomas L., and Lane, Neal F., "Quantum States of Atoms, Molecules, and Solids", Prentice-Hall, Inc., Englewood Cliffs, NJ, 1976, pp. 444-446.

(8) Gopal, E. S. R., "Statistical Mechanics and Properties of Matter", Ellis Horwood Limited, Chichester, England, 1974, pp. 160-174.

(9) Wright, Hubert Charles, "Elementary Semiconductor Physics", Van Hostrand Reinhold Co. Ltd., NY, 1979, pp. 6-25.

(10) Finklea, Harry Osborn, "A Primer on Semiconductor Liquid-Junction Solar Cells", unpublished.

(11) Vithanage, Rathnapala S., "Surface Modification of Titanium Dioxide and Synthesis of Non-electroactive Coatings of Electrochemical Polymerization", Thesis, VPI & SU, 1983.

(12) Dunlap, William Crawford, Jr., "An Introduction to Semiconductors", John Wiley & Sons, Inc., NY, 1960, pp. 78-83.

(13) Bard, Allen J., and Faulkner, Larry R., "Electrochemical Methods: Fundamentals and Applications", John Wiley & Sons, Inc., NY, 1980, pp. 629-645.

(14) Bockris, J. O'M., Conway, Brian E., and Yeager, Ernest, "Comprehensive Treatise of Electrochemistry", Plenum Press, NY, 1980, pp. 1-4.

(15) Bockris, J. O'M., Boncidat, N., and Gutmann, F., "An Introduction to Electrochemical Science", Wykeham Publications Ltd., London, 1974, pp. 85-89.

(16) Friend, J. A., and Gutmann, F., "Proceedings of the First Australian Conference on Electrochemistry", Permagon Press Ltd., Oxford, 1965, pp. 188-191.

(17) Gerischer, Heinz, Electroanalytical Chemistry and Interfacial Electrochemistry, 1975, 58 , 263-274.

(18) Crystic Research Center, "Chemical Resistance", Scott Bader Company Limited, Wellingborough, England, 1971, pp. 9-16.

(19) Power, G. P., and Ritchie, I. M., Electrochimica Acta, 1981, 26, 1973-1078.

(20) Pedersen, C. I., "Gallium Arsenide", no. 7, The Institute of Physics and the Physical Society, London, 1969, pp. 77-79.

(21) Gerischer, Heinz, Journal of Electroanalytical Chemistry, 1977, 82, 133-143.

(22) Frese, K. W., Jr., Madou, J. J., and Morrison, S. R., Journal of Physical Chemistry, 1980, 84, 3172-3178.

(23) Gerischer, Heinz, and Mindt, W., Electrochimica Acta, 1968, 13, 1329-1341.

(24) Frese, K. W., Jr., Madou, J. J., and Morrison, S. R., Journal of the Electrochemical Society, 1981, 128, 1527-1531.

(25) Vijh, Ashok K., "Oxides and Oxide Films, Volume 6", Marcel Dekker, Inc., NY, 1981, pp. 85-143.

(26) Kelly, J. J., and Notten, P. H. L., Journal of the Electrochemical Society, 1983, 130, 2452-2459.

(27) Harvey, W. W., and Kruger, J., Electrochimica Acta, 1971, 16, 2017-2037.

(28) Harvey, W. W., Journal of the Electrochemical Society, 1967, 114, 472-478.

(29) Hollan, L., Tranchart, J. C., and Memming, R., Journal of the Electrochemical Society, 1979, 126, 855-859.

(30) Ellis, Arthur B., Bolts, Jeffrey M., Kaiser, Steven W., and Wrighton, Mark S., Journal of the American Chemical Society, 1977, 99, 2848-2854.

(31) Kohl, P. A., Wolowodiuk, C., and Ostermayer, F. W., Jr., Journal of the Electrochemical Society, 1980, 127, 454-461.

(32) Bard, Allen J., and Wrighton, Mark S., "Semiconductor Liquid-Junction Solar Cells", Volume 77-3, The Electrochemical Society, Inc., Princeton, 1977, pp. 195-209.

(33) Lu, N. C. C., Reuter, W., Lu, C. Y., Lee, M. K., Shih, C. C., Wang, C. S., and Sheng, T. T., Journal of the Electrochemical Society, 1984, 131, 897-902.

(34) Aspnes, D. E., Schwartz, G. P., Gualtieri, G. J., Studna, A. A., and Schwartz, B., Journal of the Electrochemical Society, 1981, 128, 590-597.

(35) White, Henry S., Abruna, Hector D., and Bard, Allen J., Journal of the Electrochemical Society, 1982, 129, 265-271.

(36) Ginley, D.S., Baughman, R. J., and Butler, M. A., Journal of the Electrochemical Society, 1983, 130, 1999-2002.

(37) Breeze, P. A., Hartnagel, H. L., and Sherwood, P. M. A., Journal of the Electrochemical Society, 1980, 127, 454-461.

(38) Fornarini, L., Stirpe, F., and Scrosati, B., Journal of the Electrochemical Society, 1983, 130, 2184-2187.

(39) Elliott, C. R., and Regnault, J. C., Journal of the Electrochemical Society, 1980, 127, 1557-1562.

(40) Heller, A., and Miller, B., Interfacial Photoprocesses: Energy Conversion and Synthesis, 1980, 184, 215-231.

(41) Simon, R. A., Ricco, and A. J., Wrighton, M. S., Journal of the American Chemical Society, 1982, 104, 2031-2034.

(42) Skotheim, T., Petersson, L.-G., Inganas, O., and Lundstrom, I., Journal of the Electrochemical Society, 1982, 129, 1737-1741.

(43) Fan, F.-R. F., Wheeler, B. L., Bard, A. J, and Noufi, R. N., Journal of the Electrochemical Society, 1981, 128, 2042-2045.

(44) Bocarsly, A. B., Walton, E. C., Bradley, M. G., and Wrighton, M. S., Journal of Electroanalytical chemistry, 1979, 100, 283-306.

(45) Skotheim, T., Lundstrom, I., and Prejz, J., Journal of the Electrochemical Society, 1981, 128, 1625-1626.

(46) Lewis, N. S., Bocarsly, A. B., and Wrighton, M. S., Journal of Physical Chemistry, 1980, 84, 2033-2043.

(47) Noufi, R., Frank, A. J., and Nozik, A. J., Journal of the American Chemical Society, 1981, 103, 1849-1851.

(48) Bocarsly, A. B., Walton, E. G., and Wrighton, M. S., Journal of the American Chemical Society, 1980, 102, 3390-3398.

(49) Bolts, J. M., Bocarsly, A. B., Palazzotto, M. C., Walton, E. G., Lewis, N. S., and Wrighton, M. S., Journal of the American Chemical Society, 1979, 101, 1378-1385.

(50) Parkinson, B. A., and Canfield, D., Journal of the American Chemical Society, 1981, 103, 1279-1281.

(51) Finklea, Harry Osborn, and Vithanage, Rathnapala S., Journal of Physical Chemistry, 1982, 86,3621-3626.

(52) Willard, Hobart H., Merritt, Lynne L., Jr., and Dean, John A., "Instrumental Methods of Analysis", 5th ed., D. Van Nostrand Company, NY, 1974, pp. 638-651.

(53) Bond, A. M., "Modern Polarographic Methods in Analytical Chemistry", Marcel Dekker, Inc., NY, 1980, pp. 236-260.

(54) Barker, G. C., and Gardner, A. W., Zeitschrift fur Analytische Chemie, 1960, 173, 79-83.

(55) Nurnberg, H. W., "Electroanalytical Chemistry", John Wiley & Sons, Ltd., Bristol, Great Britain, 1974, pp. 41-44.

(56) Flato, Jud B., Analytical Chemistry, 1972, 44, 75A-87A.

(57) Princeton Applied Research Corporation, "Model 174A Polarographic Analyzer", Princeton, NJ, 1971.

(58) Osteryoung, Janet, Journal of Chemical Education, 1983, 60, 296-298.

(59) Plambeck, James A., "Electroanalytical Chemistry: Basic Principles and Applications", John Wiley & Sons, Inc., NY, 1983, pp. 328-329.

(60) Breyer, B., and Bauer, H. H., "Alternating Current Polarography and Tensammetry", Wiley-Interscience, NY, 1963, pp. 263-275.

(61) Vassos, Basil H., and Ewing, Galen W., "Electroanalytical Chemistry", John Wiley & Sons, Inc., NY, 1983, pp. 90-101.

(62) Pine Instrument Company, "Electrochemical Research Equipment", Grove City, PA, 1978.

(63) Albery, W. J., Transactions of the Faraday Society, 1966, 62,1915-1919.

(64) Bruno, F., Pham, M.-C., and Dubois, J.-E., Electrochimica Acta, 1977, 22, 451-457.

(65) Pham, M.-C., Lacaze, P.-C., and Dubois, J.-E., Journal of Electroanalytical Chemistry, 1978, 86, 147-157.

(66) Pham, M.-C., Dubois, J.-E., and Lacaze, P.-C., Journal of Electroanalytical Chemistry, 1979, 99, 331-340.

(67) Pham, M.-C., Tourillon, G., Lacaze, P.-C., and Dubois, J.-E., Journal of Electroanalytical Chemistry, 1981, 111, 385-390.

(68) Dubois, J.-E., Lacaze, P.-C., and Pham, M.-C., Journal of Electroanalytical Chemistry, 1981, 117, 233-241.

(69) Bard, Allen J., Journal of Chemical Education, 1983, 60, 302-304.

(70) Bolts, J. M., and Wrighton, M.S., Journal of the American Chemical Society, 1979, 101, 6179-6184.

(71) Haller, Ivan, Journal of the American Chemical Society, 1978, 100, 8050-8055.

(72) Bocarsly, A. B., Galvin, S. A., and Sinha, S., Journal of the Electrochemical Society, 1983, 130, 1319-1325.

(73) Dominey, T. N., Lewis, N. S., Bruce, J. A., Bookbinder, D. C., and Wrighton, M. S., Journal of the American Chemical Society, 1982, 104, 467-482.

(74) Finklea, Harry Osborn, Journal of the Electrochemical Society, 1982, 129, 2003-2008.

(75) Mizokawa, Y., Iwasaki, H., Nishitani, R., and Nakamura, S., Journal of Electron Spectroscopy and Related Phenomena, 1978, 14, 129-141.

(76) Laflere, W. H., van Meirhaeghe, R. L., and Cardon, F., Surface Science, 1979, 59, 401-412.

(77) Myers, D. J., and Osteryoung, J., Analytical Chemistry, 1973, 45, 267-271.

(78) Rock, Peter A., "Special Topics in Electrochemistry", Elsevier Scientific Publishing Company, NY, 1977, pp. 35-59.

(79) Shaw, B. R., Haight, G. P., and Faulkner, L. R., Journal of Electroanalytical Chemistry, 1982, 140, 147-153.

(80) Nilsson, A., Palmquist, U., Pettersson, T., and Ronlan, A., Journal of the Chemical Society, 1978, 696-707.

(81) Pletcher, Derek, "Electrochemistry", Volume 8, Academic Press, Inc., NY, 1976, pp. 127-131.

(82) Ross, S. D., Finkelstein, M., and Rudd, E. F., "Anodic Oxidation", Academic Press, NY, 1975, pp. 271-275.

(83) Albery, W. J., and Hitchman, M. L., "Ring-Disc Electrodes", Clarendon Press, Oxford, Great Britain, 1971, pp. 2-25.

(84) Pleskov, Yu V., and Filinovskii, V. Yu, "The Rotating Disc Electrode", Nauka Press, Moscow, 1972, pp. 287-311.

(85) Menezes, S., and Miller, B., Journal of the Electrochemical Society, 1983, 130, 517-523.

(86) Decker, F., Pettinger, B., and Gerischer, H., Journal of the Electrochemical Society, 1983, 130, 1335-1339.

(87) Memming, R., Journal of the Electrochemical Society, 1978, 125, 117-123.

(88) Sawyer, Donald T., and Roberts, Julian L., Jr., "Experimental Electrochemistry for Chemists", John Wiley & Sons, Inc., NY, 1974, pp. 74-76.

(89) Frese, K. W., Jr., Madou, M. J., and Morrison, S. R., Journal of the Electrochemical Society, 1981, 128, 1939-1943.

(90) Madou, M. J., Frese, K. W., Jr., and Morrison, S. R., Journal of the Electrochemical Society, 1980, 127, 987-989.

The vita has been removed from the scanned document